

VOLUMETRIC NON-CONTRAST PULMONARY PERFUSION
USING ARTERIAL SPIN LABELED MAGNETIC RESONANCE IMAGING

by

Joshua S. Greer



APPROVED BY SUPERVISORY COMMITTEE:

Ananth J. Madhuranthakam, Chair

Heather Hayenga

Robert Rennaker

A. Dean Sherry

Copyright 2018

Joshua S. Greer

All Rights Reserved

To my parents, Dr. Steven Craig Greer and Mrs. Norma Greer.

VOLUMETRIC NON-CONTRAST PULMONARY PERFUSION
USING ARTERIAL SPIN LABELED MAGNETIC RESONANCE IMAGING

by

JOSHUA S. GREER, BS

DISSERTATION

Presented to the Faculty of
The University of Texas at Dallas
in Partial Fulfillment
of the Requirements
for the Degree of

DOCTOR OF PHILOSOPHY IN
BIOMEDICAL ENGINEERING

THE UNIVERSITY OF TEXAS AT DALLAS

December 2018

ACKNOWLEDGMENTS

This work would not have been possible without the support and encouragement of many people.

I am extremely grateful to my advisor, Dr. Ananth Madhuranthakam, for providing me the opportunity to join his lab. Ananth has been an exceptional mentor. His door was always open when I had questions about my research or needed critique on my writing, and I matured both professionally and personally while working with him. I appreciate his patience and insightful advice during our many discussions.

I would also like to thank my dissertation committee members, Drs. Heather Hayenga, Robert Rennaker, and Dean Sherry. I appreciate your time and guidance over the years to help shape my projects.

I would like to recognize Drs. Robert E. Lenkinski and Ivan Pedrosa. Their advice has kept me focused on answering clinically important questions and has greatly improved my work as a scientist. I also want to thank Dr. Ivan Dimitrov, whose knowledge and support of my MR sequence development was incredibly valuable. I also appreciate Ivan's help in shaping my scientific presentations over the years. I want to thank Trevor Wigal and Dr. Kelli Key for their help in recruiting volunteers and supporting my research, and Dr. Keith Hulsey for his assistance with my perfusion phantom work.

I am also thankful for the opportunity to work with the Children's Health Cardiology research team: Amanda Potersnak and Drs. Tarique Hussain, Gerald Greil, Animesh Tandon, Barbara Burkhardt, Riad Zahr, and Jerry Michael. Your help and patience were greatly appreciated as I began my research in pediatric cardiac imaging. I look forward to working with you all in the next stage of my career.

I would especially like to thank the current and past members of the UT Southwestern MR research team: Dr. Yue Zhang, Dr. Crystal Harrison, Dr. Xinzeng Wang, Dr. Shu Zhang, Dr. Huajun She, Dr. Quyen Do, Dr. Ece Ercan, Dr. Durgesh Dwivedi, and Yiming Wang. You all provided much needed encouragement and friendship throughout my graduate career, and I will miss the insightful research discussions that we had. I also want to thank Quyen and Ece for constructive criticism of my dissertation.

Finally, I want to thank my family: my parents, Craig and Norma, and my brother and sister, Aaron and Rachel, for their unconditional love and encouragement, and my fiancée Monisha Thomas, who has been extremely loving, patient, and supportive throughout my graduate work, and has made countless sacrifices to help me complete this dissertation.

August 2018

VOLUMETRIC NON-CONTRAST PULMONARY PERFUSION
USING ARTERIAL SPIN LABELED MAGNETIC RESONANCE IMAGING

Joshua S. Greer, PhD
The University of Texas at Dallas, 2018

Supervising Professor: Ananth. J. Madhuranthakam

Arterial spin labeled (ASL) magnetic resonance imaging (MRI) is a rapidly growing area of research with significant clinical potential, primarily because it can provide non-invasive quantitative perfusion maps. A significant portion of ASL application have been in the brain and kidneys, though quantitative pulmonary perfusion would be beneficial in the management of chronic lung conditions. The work presented in this dissertation aims to develop non-contrast pulmonary perfusion imaging using ASL for volumetric coverage of the entire lungs. The established FAIR ASL technique is applied at 3T for improved SNR and the reproducibility of quantified perfusion is demonstrated. Further developments are made to reduce the sensitivity of FAIR perfusion imaging to respiratory motion and to reduce unwanted vascular signal. This enabled robust measurement of perfusion across the entire lung using multi-slice FAIR. Pseudo-Continuous ASL is investigated for use in the lungs to further improve SNR. Different labeling strategies are explored and the effects of cardiac phase on ASL-measured perfusion are examined. Next, the presented lung perfusion imaging techniques are applied in a clinical setting to better understand the cardiopulmonary flow patterns in pediatric patients with Fontan circulation. To

extend these techniques for 3D perfusion mapping, a Cartesian Acquisition with Spiral PRofile Ordering (CASPR) is developed to make ASL measurements more robust to sources of noise and motion artifacts. CASPR is demonstrated for brain and kidney perfusion imaging where ASL has been well established. This view ordering improved SNR and enabled 3D coverage of the brain and kidneys in similar scan times to a 2D slice. Finally, for ASL to be adopted for clinical perfusion imaging, it must be established as an accurate and reproducible perfusion measurement technique. A quality-control perfusion phantom is developed and tested to validate ASL-measured perfusion. In summary, the presented work makes ASL more valuable for clinical non-contrast measurement of pulmonary perfusion.

TABLE OF CONTENTS

ACKNOWLEDGMENTS	v
ABSTRACT.....	vii
LIST OF FIGURES	xiii
LIST OF ABBREVIATIONS.....	19
CHAPTER 1 INTRODUCTION	21
1.1 Motivation.....	21
1.2 Background: Perfusion Imaging	22
1.3 MR Perfusion Imaging.....	23
1.3.1 Exogenous Contrast.....	23
1.3.2 Hyperpolarized Gas.....	24
1.3.3 Fourier Decomposition.....	24
1.4 MR Perfusion Imaging: Arterial Spin Labeling.....	25
1.4.1 Contrast mechanism	25
1.4.2 Blood labeling approaches	27
1.4.3 Perfusion Quantification	30
1.5 Objectives	32
CHAPTER 2 NON-CONTRAST QUANTITATIVE PULMONARY PERFUSION USING FLOW ALTERNATING INVERSION RECOVERY AT 3T	34
2.1 Introduction.....	34
2.2 Methods.....	35
2.1.1 MR Imaging	35
2.1.2 FAIR Perfusion Quantification	38
2.1.3 SPECT Perfusion.....	38

2.1.4	Image Analysis	39
2.2	Results	39
2.2.1	FAIR Perfusion	39
2.2.2	FAIR Perfusion vs. SPECT Perfusion.....	41
2.2.3	Reliability of FAIR Perfusion	44
2.3	Discussion	44
CHAPTER 3 ROBUST NON-CONTRAST PERFUSION IMAGING OF WHOLE-LUNGS USING MULTI-SLICE FAIR AT 3T		50
3.1	Introduction.....	50
3.2	Background Suppression	51
3.2.1	Theory	51
3.2.2	Background suppression optimization	54
3.3	Inflow Saturation	55
3.4	Whole-lung coverage using multi-slice FAIR	58
3.5	Discussion.....	62
CHAPTER 4 ON THE APPLICATION OF PSEUDO-CONTINUOUS ASL FOR PULMONARY PERFUSION IMAGING.....		64
4.1	Introduction.....	64
4.2	Methods.....	65
4.3	Labeling approach 1: Inferior Vena Cava.....	66
4.3.1	Influence of cardiac phase.....	67
4.3.2	Cardiac-triggered acquisition	69
4.4	Labeling approach 2: Right pulmonary artery	72
4.5	Discussion.....	72

CHAPTER 5 ASSESSMENT OF CAVAL BLOOD FLOW DISTRIBUTION IN FONTAN CIRCULATION USING ARTERIAL SPIN LABELED MEASUREMENT OF PULMONARY PERFUSION	77
5.1 Introduction.....	77
5.2 Methods.....	79
5.2.1 ASL-MRI	79
5.2.2 4D-Flow MRI.....	81
5.3 Results.....	82
5.4 Discussion.....	86
CHAPTER 6 ROBUST 3D PCASL PERFUSION IMAGING USING A CARTESIAN ACQUISITION WITH SPIRAL PROFILE ORDERING (CASPR)	89
6.1 Introduction.....	89
6.2 Methods.....	90
6.2.1 3D Cartesian Acquisition with Spiral PProfile Ordering (CASPR)	90
6.2.2 MR Imaging	90
6.2.3 Quantification.....	91
6.2.4 Image Reconstruction.....	92
6.2.5 Statistical Analysis	92
6.3 Application in the Brain.....	92
6.3.1 Arterial Spin Labeling.....	92
6.3.2 Background Suppression and Inflow Saturation.....	93
6.3.3 Acquisitions.....	93
6.3.4 Results	94
6.4 Application in the Kidneys	96
6.4.1 Arterial Spin Labeling.....	96

6.4.2	Background Suppression and Inflow Saturation.....	97
6.4.3	Acquisitions.....	98
6.4.4	Results.....	98
6.5	Discussion.....	101
CHAPTER 7 A PERFUSION PHANTOM FOR QUALITY CONTROLLED MEASUREMENT OF ARTERIAL SPIN LABELED PERFUSION		104
7.1	Introduction.....	104
7.2	Perfusion phantom	105
7.2.1	Design.....	105
7.2.2	Results.....	106
7.3	3D printed perfusion phantom	110
7.3.1	Design.....	110
7.3.2	Results.....	111
7.4	Discussion.....	115
CHAPTER 8 DISCUSSION AND FUTURE DIRECTIONS		117
REFERENCES		121
BIOGRAPHICAL SKETCH		132
CURRICULUM VITAE		

LIST OF FIGURES

- Figure 1.1: ASL control image in the lungs with inflowing blood at equilibrium, and the corresponding label image with inflowing blood inverted. Subtracting the control and label images results in a perfusion-weighted image.26
- Figure 1.2: Longitudinal magnetization of the control (blue) blood, and labeled (red) blood throughout an ASL sequence. Inverted spins recover back to equilibrium at the rate of T_1 , reducing the resulting ASL signal as the post-label delay is extended.27
- Figure 1.3: Pulsed-ASL (PASL) and Continuous-ASL (CASL) sequences in the lungs at three time points throughout the experiment: equilibrium, labeling, and acquisition. PASL labeling is applied with a single pulsed inversion covering the inflowing blood, while CASL labeling is applied continuously over the inflowing vessel (pulmonary artery) for a chosen label duration, LD. After a post-label delay (PLD) to allow labeled blood to perfuse the lungs, the image is acquired.29
- Figure 1.4: RF and gradient diagram for Continuous ASL (CASL) and pseudo-Continuous ASL (pCASL), with reduced RF duty cycle to allow continuous labeling on standard RF amplifiers.30
- Figure 2.1: Schematic of the ECG-triggered FAIR sequence. (A) On cardiac trigger, the pre-saturation followed by slice/slab selective inversion pulses are applied. After an inversion delay (e.g. 1 R-R interval), data are acquired using a SShtSE acquisition during the diastolic phase of the subsequent cardiac cycle. (B) Schematic of the coronal image showing the sagittal imaging slice (red), slice-selective inversion [65] and slab-selective inversion (blue).36
- Figure 2.2: FAIR perfusion-weighted images (a-c, top row) and reconstructed quantitative perfusion maps (d-f, bottom row) in the sagittal (a,d), coronal (b,e), and axial (c,f) orientations in a 29-year old healthy male volunteer.40
- Figure 2.3: Average flow rate in the right pulmonary artery (RPA) measured using phase contrast (PC) vs. pulmonary perfusion measured in the right lung using sagittal and coronal FAIR images in nine subjects, showing a moderate correlation. A coronal image was not acquired in one of the volunteers.42
- Figure 2.4: Coronal proton density weighted image (a), SPECT perfusion image (b), FAIR perfusion-weighted image (c), and reconstructed perfusion map derived from FAIR perfusion (d) in a 33-year old healthy female volunteer. Arrows indicate signals from major vessels that are visible on FAIR perfusion images (c,d), and seen as regions of photopenia on SPECT images (b).43

Figure 2.5: Sagittal proton density weighted image (a), SPECT perfusion image (b), FAIR perfusion-weighted image (c), and reconstructed perfusion map derived from FAIR perfusion (d) in a 28-year old healthy male volunteer. Arrows indicate signals from major vessels that are visible on FAIR perfusion images (c,d), and seen as regions of photopenia on SPECT images (b).....43

Figure 2.6: Coronal FAIR perfusion-weighted image (a) shows significant signal from the major pulmonary vessels. When masked using a threshold (e.g. >1000 ml/100g/min), the FAIR perfusion-weighted image (b) shows parenchymal perfusion, matching more closely the SPECT perfusion (c). These images were acquired in a 27-year old male healthy volunteer.44

Figure 2.7: Bland-Altman plots to assess intra-session (top row) and inter-session (bottom row) reliability of FAIR measured pulmonary perfusion, with vessels (left column) and without vessels included in the region of interest (right column). The intra-class correlation coefficients (ICC) are shown on the plots. Four subjects scanned twice each for intra-session and inter-session measurements are shown on the plots.45

Figure 3.1: Evolution of the Z-magnetization of inflowing blood and background tissue throughout the FAIR sequence without (A) and with (B) four background suppression inversion pulses applied during the post labeling delay.53

Figure 3.2: FAIR without background suppression: control image (A), label image (B), and perfusion-weighted image (C). FAIR with background suppression: control image (D), label image (E), and perfusion-weighted image (F). Red arrows indicate the reduction in background signal at the dome of the spleen due to image misregistration, even though these images were acquired in a breathhold. Blue arrows show failed background suppression in the fat in the source images, and green arrows show near the fat in the subtracted perfusion-weighted images.....54

Figure 3.3: the Bloch equation simulation results: (a) HS ($\beta = 4$, $\mu = 6$); (b) HS ($\beta = 4$, $\mu = 18$); (c) HS ($\beta = 12$, $\mu = 6$) and (d) C-FOCI ($\beta = 4$, $\mu = 6$ and $C_{max} = 3$). The red dashed line shows adiabatic threshold at different off-resonance. The white dashed line shows the fat resonance frequency at 3T. (e) Compares the adiabatic thresholds of C-FOCI (red), HS ($\beta = 4$, $\mu = 18$, blue) and HS ($\beta = 12$, $\mu = 6$, green).....56

Figure 3.4: Sagittal 2D FAIR control images acquired with HS (A) and C-FOCI (B) background suppression inversion pulses. The background tissue was more completely suppressed with the C-FOCI pulse compared to HS, particularly in regions of fat.57

Figure 3.5: Coronal T2-weighted (a), FAIR without (b) and with (c) inflow saturation, showing decreased signal in the major vessels (arrows). FAIR perfusion-weighted images were acquired using 2 signal averages.....58

Figure 3.6: Sagittal FAIR perfusion-weighted images in a pulmonary hypertension patient without background suppression, with background suppression, and with background suppression and inflow saturation. Perfusion deficits (arrows) that correlate well with the heterogeneous dark patches across the lung in CT, are visible after suppressing background tissue and bright vascular signal, and are not apparent in the original FAIR image.58

Figure 3.7: ECG-triggered FAIR sequence with background suppression and inflow saturation. The variable inflow saturation duration before the acquisition (τ) saturates inflowing signal that is left in the larger pulmonary vessels at the time of imaging, while inflowing labeled blood before this time can be seen as tissue perfusion.59

Figure 3.8: (a) Imaging slice (red) with 3x wider selective inversion (white) and inflow saturation pulses covering the heart and pulmonary arteries (blue). Non-selective inversion not shown. The labeling inversion and acquisition shift together across the lungs for full coverage (white arrows).....60

Figure 3.9: ASL control images across the right lung with HS and C-FOCI background suppression pulses. Arrows indicate regions where background tissue was more completely suppressed with C-FOCI compared to HS, mostly in fat tissue where off-resonance is higher.61

Figure 3.10: Perfusion-weighted images across the right lung from the scan shown in Figure 3.9, with HS and FOCI background suppression pulses. C-FOCI perfusion images show improved SNR compared to HS, and improved suppression in fat tissue (arrows).61

Figure 3.11: (a) Perfusion-weighted images across the lung with C-FOCI background suppression. The center slice was repeated with increasing inflow saturation duration (τ). As τ increases, more of the inflowing label bolus is saturated, reducing the vascular signal until $\tau=300\text{ms}$, where true tissue perfusion can be seen. After this optimal τ for this subject, the tissue perfusion is saturated as well. The window level has been adjusted between (a) and (b) for improved visualization of each slice and the effects of inflow saturation.62

Figure 4.1: (A) Assumed ECG Signal with constant cardiac period with a diastolic acquisition. (B) Example of an ECG signal with slight heart rate variation after triggering the presaturation pulses. This change in timing leads to a systolic acquisition, producing signal variations unrelated to the ASL signal.....66

Figure 4.2: Coronal proton density weighted image with labeling plane applied over the IVC in red (A) and the corresponding coronal perfusion-weighted image (B). (C) Shows a sagittal perfusion-weighted image with IVC labeling in another volunteer.....67

Figure 4.3: pCASL perfusion-weighted images with IVC labeling, showing the substantial inconsistencies experienced between identically-acquired signal averages.68

Figure 4.4: (A) Phase-contrast velocity measurement in the RPA throughout the cardiac cycle, and (B) the corresponding signal intensity in vessel and lung tissue ROIs (C, red and blue boxes), showing the inverse relationship between SShTSE-measured signal intensity and flow velocity. (D) shows the subtraction of images acquired at 500 ms and 200 ms trigger delays, indicated by vertical red lines in (B), demonstrating the significant signal differences that can be introduced by flow in addition to spin labeling to create a “perfusion-like” image.....	69
Figure 4.5: pCASL pulse sequence implemented with cardiac triggering of the acquisition, such that data acquisition using SShTSE occurs in the diastolic phase of the cardiac cycle for constant heart rates (A) and varied heart rates (B).	70
Figure 4.6: (A-C) show multiple repetitions of the pCASL sequence with IVC labeling after the implementation of a cardiac triggered acquisition to minimize the variations in cardiac phase, showing more consistent perfusion signal, and the perfusion image resulting from the average of 10 repetitions (D).	71
Figure 4.7: (A-C) show multiple repetitions of the pCASL sequence with sagittal labeling of the RPA and cardiac triggered acquisition, showing consistent perfusion signal. The average of 16 repetitions provides a perfusion image with high SNR (D).	73
Figure 4.8: (A) Sagittal proton-density weighted image, (B) FAIR perfusion-weighted image, and (C) pCASL perfusion-weighted image using sagittal labeling of the RPA and a cardiac triggered acquisition.....	74
Figure 5.1: Cardiopulmonary circulation in a normal heart, a congenital heart defect resulting in a missing tricuspid valve (tricuspid atresia), and the result of the Fontan operation to restore venous flow to the pulmonary circulation. Figure adapted from [101].	79
Figure 5.2: Coronal lung perfusion images from representative subjects acquired using FAIR (total perfusion) and pCASL (IVC contribution only), and 4D-flow pathlines from the SVC and IVC. The graphs show the calculated percentages of IVC flow to the left and right lungs, which are visually in agreement with the ASL and 4D-flow results for each subject. An artifact caused by pCASL labeling can be seen below the diaphragm (red arrows).	83
Figure 5.3: Quantified Perfusion with (A) FAIR and (B) pCASL. Quantified FAIR perfusion is in the expected range for normal lungs. pCASL shows reduced perfusion because the perfusion signal is diluted by unlabeled SVC blood flow.	84
Figure 5.4: Percentage of IVC flow to the right lung: (a) showing good agreement between ASL and 4D-Flow measurements. Subjects shown in figure 1 are indicated by the blue data points. (b) Bland-Altman analysis of pCASL and 4D Flow measurements, showing a bias of 4.39%, with 95% confidence intervals shown in red.	85

Figure 6.1: Sampling patterns of a 3D TSE acquisition using linear (a), linear with half-scan (b) and CASPR (c) view ordering shown in k_y - k_z plane, where each point represents an echo. The echoes sampled at the beginning of the echo train are shown in blue and transition to red at the end of each echo train. The CASPR acquisition traverses out in a spiral trajectory but maintains sampling on a Cartesian grid.91

Figure 6.2: Multiple slices showing complete brain coverage using 3D TSE pCASL with (A) linear and (B) CASPR trajectories.95

Figure 6.3: Brain perfusion images of the same slice acquired using (A) 30 repetitions of 2D pCASL EPI, (B) average EPI image from 30 repetitions, and (C) 3D TSE with CASPR View Ordering. The 3D TSE images are axial reformats from a sagittal acquisition.95

Figure 6.4: Axial quantified perfusion slices through the brain acquired with (A) 2D pCASL EPI and (B) reformatted 3D CASPR.96

Figure 6.5: (A) Relative dispersion in each ROI across the brain for both acquisitions, showing more homogenous perfusion with CASPR. (B) Bland-Altman analysis of mean quantified perfusion measurements in each ROI across the brain showed no significant bias between the techniques. 95% confidence intervals of the agreement are shown in red.97

Figure 6.6: Coronal perfusion-weighted images across the kidney acquired with (A) 3D linear-ordered and (B) 3D CASPR TSE, showing reduced artifacts due to physiological noise with CASPR.99

Figure 6.7: Quantified perfusion images acquired using (A) 2D SShTSE and (B) 3D CASPR. 101

Figure 6.8: Coronal kidney CASPR acquisition with axial and sagittal reformats, acquired with (A) 3x3x6mm resolution (B) 3x3x3mm with a SENSE factor of 2, acquired in the same scan time.101

Figure 6.9: Bland-Altman analysis of perfusion to the renal cortex. Perfusion measured with 2D SShTSE and 3D CASPR agreed in all 5 subjects, and no significant bias was found between the techniques. 95% confidence intervals of the agreement are shown in red.101

Figure 7.1: Original phantom design with three sponges in line with the tubing submerged in a water bath.106

Figure 7.2: (a) Coronal T2W image of the flow phantom. The labeling plane is shown in red. (b) perfusion-weighted image with labeling applied for 2 seconds (c) perfusion-weighted image with labeling applied for 6 seconds. Both perfusion images had a post-label delay of 100ms and a flow rate of 300mL/min. The sponge on the right is denser than the other two, and serves as a control with close to zero perfusion. Colored ROIs used for perfusion measurements are shown in (a).107

Figure 7.3: Pump flow rate vs. measured pCASL perfusion in three sponges, showing increased perfusion with increasing flow rate in each sponge.....	107
Figure 7.4: pCASL perfusion measurements in the same sponges with identical flow rates on different days, performed a week apart.....	108
Figure 7.5: (A) Estimated perfusion compared with measured pCASL perfusion. (B) Bland-Altman analysis shows a negative bias in the ASL measurements. The perfusion signal in sponge 1 can be seen tapering off at, particularly at higher perfusion rates in both (A) and (B).	109
Figure 7.6: Phantom schematic (A) with branching inflow vessels that terminate in the larger sponge chamber, and (B) 3D printed phantom containing a sponge with sealed lid and input/output tubes to be connected to the pump.	111
Figure 7.7: Perfusion-weighted images at varied post-label delays acquired with (A) FAIR and (B) pCASL.	112
Figure 7.8: Average ASL signal in the sponge at varied PLDs and flow rates acquired with FAIR and pCASL.....	113
Figure 7.9: Analysis of the agreement between FAIR and pCASL measured perfusion. (A) shows linearly-increasing perfusion as the pump flow rate is increased. (B) shows Bland-Altman analysis of the agreement between FAIR and pCASL measurements.	114
Figure 7.10: Bland-Altman analysis of the reproducibility of FAIR and pCASL quantitative perfusion measurements.....	115
Figure 8.1: Sagittal perfusion-weighted images acquired through the lung using pCASL labeling of the RPA and a cardiac-triggered 3D CASPR acquisition.....	119
Figure 8.2: 3D perfusion-weighted image acquired with pCASL with CASPR view ordering in the sagittal plane (A), with axial (B) and coronal (C) reformats.	119

LIST OF ABBREVIATIONS

1.5T	1.5 Tesla
2D	Two dimensional
3D	Three dimensional
3T	3 Tesla
ASL	Arterial spin labeling
AVM	Arteriovenous malformation
B ₀	Static magnetic field
B ₁	Radiofrequency magnetic field
CASL	Continuous arterial spin labeling
COPD	Chronic obstructive pulmonary disease
CT	Computed tomography
DCE	Dynamic contrast enhanced
EPI	Echo planar imaging
FAIR	Flow alternating inversion recovery
FOCI	Frequency offset corrected inversion
FOV	Field of view
GBCA	Gadolinium-based contrast agent
HS	Hyperbolic secant
IVC	Inferior vena cava
LD	Label duration
LPA	Left pulmonary artery

MRI	Magnetic resonance imaging
MT	Magnetization transfer
PASL	Pulsed arterial spin labeling
pCASL	Pseudo-continuous arterial spin labeling
PET	Positron emission tomography
PH	Pulmonary hypertension
PLD	Post-label delay
RD	Relative dispersion
RF	Radio frequency
ROI	Region of interest
RPA	Right pulmonary artery
SNR	Signal-to-noise ratio
SPECT	Single photon emission computed tomography
SShTSE	Single-shot turbo spin echo
SVC	Superior vena cava
T1	Longitudinal relaxation time constant
T2	Transverse relaxation time constant
TE	Echo time
TI	Inversion time
TR	Repetition time
TSE	Turbo spin Echo
V/Q	Ventilation/perfusion

CHAPTER 1

INTRODUCTION

1.1 Motivation

Chronic obstructive pulmonary diseases (COPD), like chronic bronchitis and emphysema, are a major cause of disability in the US, and are projected to become the third leading cause of death worldwide by 2030 [1]. These diseases heterogeneously disrupt ventilation (V) and perfusion (Q) equilibrium across the lung, causing low arterial blood oxygen, or hypoxemia. Ventilation refers to the amount of air reaching the alveoli in the lungs, where blood is oxygenated through diffusion to the capillaries, and pulmonary perfusion refers to the rate of blood delivery to those capillaries. When the V/Q ratio is properly matched, efficient blood oxygenation can be achieved, but if this ratio is disrupted, known as V/Q mismatch, the rate of oxygen diffusion into the blood decreases. In addition to hypoxemia, these diseases can also lead to difficulty in breathing, high blood pressure, and frequently result in pulmonary hypertension (PH) development, which can eventually cause heart failure and death [2].

Current clinical diagnosis of pulmonary hypertension is performed using spirometry to assess the overall lung capacity to oxygenate blood. Though spirometry is an effective method to measure total lung function, these tests are unable to detect the regional abnormalities that occur in ventilation and perfusion across the lung. Because pulmonary hypertension symptoms do not manifest until significant vascular damage has already occurred, there is a need to develop a non-invasive approach to detect biomarkers of chronic lung disease development at presymptomatic stages [3]. In order to achieve this goal, and to effectively assess disease progression and treatment, imaging evaluation of regional perfusion deficits across the lung is essential.

1.2 Background: Perfusion Imaging

^{15}O PET is regarded as the gold standard for perfusion imaging because it uses H_2O^{15} that can freely diffuse into the tissue, resulting true linear increases in measured tissue perfusion, regardless of the flow rate, while other tracers, such as those based on radioactive Technetium ($^{99\text{m}}\text{Tc}$), will experience reduced extraction into the tissue as flow increases [4]. However, due to the limited half-life of ^{15}O (2 minutes), on-site production with a cyclotron is required. In practice, this process can be difficult and cost-prohibitive, limiting its use to specialized hospitals and research centers. Clinically, V/Q planar scintigraphy is used to detect V/Q mismatches. This technique uses radioactive tracers to image both ventilation and perfusion, and is the preferred screening method for suspected pulmonary hypertension due to its increased sensitivity compared to CT pulmonary angiography [5, 6] using iodinated contrast agents. Although lung V/Q scans can offer functional information about the blood oxygenation process, the resulting images are restricted to 2D projection images and are relatively low resolution. 3D perfusion images of the whole lung can be achieved with single photon emission computed tomography (SPECT) using $^{99\text{m}}\text{Tc}$ [7, 8]. All current clinical imaging techniques require some form of ionizing radiation from either an injected radioactive isotope or exposure to x-ray radiation. This is a concern for patients needing frequent exposure, particularly in children and younger patients who may need repeated scans to monitor disease progression or therapy response [9]. Magnetic Resonance Imaging (MRI) can provide important metrics, particularly those related to hemodynamics and ventricular volumes, which are being increasingly recognized as prognostic biomarkers in the management of pulmonary hypertension (PH) patients [10]. An MRI technique to also evaluate pulmonary perfusion would be beneficial, because it does not require ionizing radiation, and offers improved

spatial resolution over nuclear medicine approaches. The focus of this dissertation is on the development of a perfusion MRI protocol.

1.3 MR Perfusion Imaging

1.3.1 Exogenous Contrast

Perfusion can be measured with dynamic contrast enhanced (DCE) MRI. This technique requires the intravenous injection of a Gadolinium-based contrast agent (GBCA), which creates contrast by shortening the T1 relaxation rate of adjacent spins. After administration, these contrast agents are rapidly distributed throughout the blood, and T1-weighted images are acquired over several minutes as the contrast agent arrives in the extracellular space of the tissue. The rate of GBCA arrival in the tissue can be used to quantify absolute perfusion, although this requires the assumption of an accurate arterial input function to describe the rate of blood delivery to the tissue [11, 12]. Although contrast-based perfusion imaging offers both high temporal resolution and signal to noise ratio (SNR), the need for administration of exogenous contrast restricts the number of repeated measurements in a subject and is highly dependent on the acquisition timing [13]. The vascular permeability of the contrast agent has also been shown to confound quantitative DCE measurements, since GBCAs cannot freely diffuse into the tissue [14]. Additionally, the repeated use of GBCAs has been implicated in several potential health risks. Contrast injection is contraindicated in patients with impaired renal function due to the risk of nephrogenic systemic fibrosis development [15, 16]. There have also been recent reports of long-term Gadolinium deposition in the body, particularly in the brain, skin, and bone samples of patients who have received multiple doses of GBCAs [17-19]. Free Gadolinium (III) is known to be toxic as it can

compete with Calcium (II) due to their similarity in size, disrupting Calcium (II)-dependent signaling. Thus, there has been widespread concern about the use of these agents, though no negative effects have been reported. Nevertheless, DCE provides perfusion maps with high SNR, is routinely used for clinical perfusion evaluation, and has been well-correlated with perfusion scintigraphy in the lungs [20, 21].

1.3.2 Hyperpolarized Gas

An alternative perfusion imaging method based on gas exchange has been demonstrated by measuring the diffusion of inhaled hyperpolarized Xenon-129 gas into the blood. This technique measures spectral peaks from the dissolved-phase Xenon to image the gas that has dissolved in the blood and lung parenchyma, which are simultaneously acquired with the gas-phase Xenon peaks, and can be used to generate ventilation maps [22]. However, the extension to routine clinical applications is impeded by high costs associated with the limited availability of the polarizer, additional scanner hardware, and personnel expertise [23].

1.3.3 Fourier Decomposition

In recent years, the Fourier Decomposition approach was proposed as a non-contrast approach to measure pulmonary ventilation and perfusion [24, 25]. Rather than imaging the wash-in of a contrast agent or inhaled gas, this technique acquires a rapid series of images during free breathing, which are subsequently co-registered. Perfusion and ventilation maps are then generated based on the periodic variations over the time series of images that occur at frequencies near those of the respiratory and cardiac cycles. This technique has shown potential for pulmonary perfusion-weighted imaging [26, 27], and an approach to derive absolute perfusion values from Fourier

Decomposition images has also been proposed [28], although interpretation of these signal variations requires further validation.

1.4 MR Perfusion Imaging: Arterial Spin Labeling

Although DCE-MRI is currently used clinically in the evaluation of perfusion, the widespread adoption of these established techniques has been restricted due to risk associated with contrast administration, limited availability of specialized hardware, and lack of robust perfusion quantification, and no technique to quantify pulmonary perfusion without the need for contrast administration has been established for clinical use. Arterial spin labeling (ASL) is an alternative perfusion MRI approach that can measure perfusion without exogenous contrast administration [29, 30]. ASL has significant clinical potential due to its ability to quantify absolute perfusion [31], and has been extensively studied in the brain [32, 33], kidneys [14, 34-40], and to some degree in the lungs [41-43]. The use of water as an endogenous contrast is especially important in enabling repeated measurements in cases of impaired renal function and in pediatric populations, where the use of contrast agents may be restricted.

1.4.1 Contrast mechanism

Arterial spin labeling refers to the process of magnetically labeling water molecules in the inflowing arterial blood, using them as a source of endogenous contrast. Labeling is achieved by inverting (or saturating) the proton spins in the inflowing blood, such that the resulting signal in the perfused tissue is attenuated when the labeled blood arrives. After labeling, a post-labeling delay (PLD) is used to allow labeled blood to reach the tissue before image acquisition. The sequence is repeated with the labeling inversion applied such that inflowing blood is unaffected,

while maintaining identical magnetization transfer (MT) effects in the imaging slice [44], serving as a “control” sequence. The difference between these control and label images is proportional to the attenuated signal from labeled blood that is delivered to the tissue, and by subtracting these images, a perfusion-weighted image can be created (Figure 1.1). During the post-label delay, the inverted label blood also recovers back to equilibrium (T1 relaxation), reducing the overall ASL signal that can be measured (Figure 1.2). Therefore, a compromise between the time allowed for the delivery of labeled blood and T1 relaxation must be met.

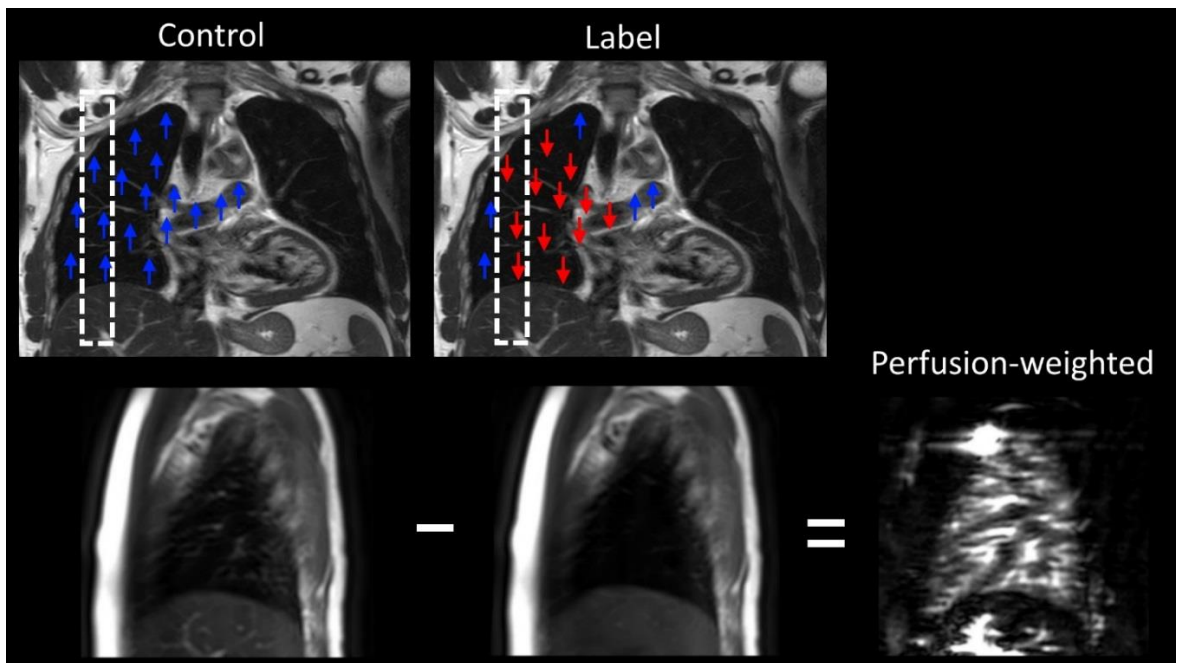


Figure 1.1: ASL control image in the lungs with inflowing blood at equilibrium, and the corresponding label image with inflowing blood inverted. Subtracting the control and label images results in a perfusion-weighted image.

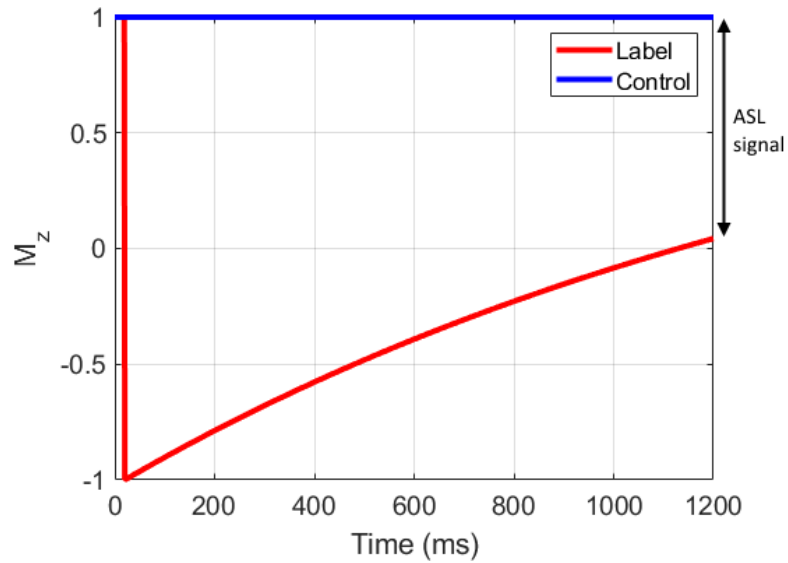


Figure 1.2: Longitudinal magnetization of the control (blue) blood, and labeled (red) blood throughout an ASL sequence. Inverted spins recover back to equilibrium at the rate of T_1 , reducing the resulting ASL signal as the post-label delay is extended.

1.4.2 Blood labeling approaches

There are several different approaches that have been proposed to label inflowing blood [45], which can be generally categorized as continuous-ASL (CASL) and pulsed-ASL (PASL). In recent years, a modified CASL approach known as pseudo-continuous ASL (pCASL) was proposed to overcome technical challenges associated with the application of continuous radio frequency (RF) pulses [46].

Continuous ASL

Continuous spin labeling is achieved through a process known as flow-driven adiabatic inversion. An adiabatic RF pulse is one that can achieve nearly perfect inversion (or excitation) of the affected magnetization with relatively low sensitivity to inhomogeneities in the B_0 and B_1 fields, provided that the B_1 amplitude is high enough, and exceeds the adiabatic threshold [47]. By

sweeping the RF pulse frequency from below to above the resonance frequency, the affected spins will follow the effective magnetic field, and be completely inverted. Continuous labeling, or flow-driven adiabatic inversion, is achieved by the constant application of RF at a fixed frequency and amplitude. When a gradient is applied in the direction of flow during this continuous RF, the flowing spins will experience a sweeping resonance frequency relative to the frequency of the fixed RF pulse. As the spins move through the magnetic gradient, they will undergo adiabatic inversion. This process allows for continuous labeling of inflowing blood moving perpendicularly through a prescribed labeling plane. However, continuous labeling approaches are sensitive to off-resonance effects, which reduces the labeling efficiency. More importantly, to achieve constant application of these long continuous RF pulses, modified hardware is required, making this technique impractical for use on clinical scanners [48]. The original implementations of ASL used continuous labeling to invert blood flowing into the brain of rats [30], which was later extended to human brain and lung imaging [49, 50], but technical challenges have led to it largely being replaced by pCASL.

Pulsed ASL

Pulsed arterial spin labeling (PASL) techniques use a single pulsed inversion slab over the inflowing blood adjacent to the imaging region (Figure 1.3). PASL was proposed to overcome several practical challenges associated with CASL, and enabled the early ASL perfusion studies in humans [51]. These approaches can achieve higher labeling efficiency than CASL, and allow for labeling near the tissue of interest, reducing the transit time of inverted blood signal. However, because all of the inflowing blood is inverted at the same time, spins distal from the imaging region will offer reduced SNR due to T1 relaxation (Figure 1.2), limiting the overall efficiency of PASL

approaches. With high labeling efficiency, continuous labeling can provide a significant SNR advantage over pulsed labeling [52]. Nevertheless, the robust labeling and ease of use have led to the widespread use of PASL approaches for perfusion imaging.

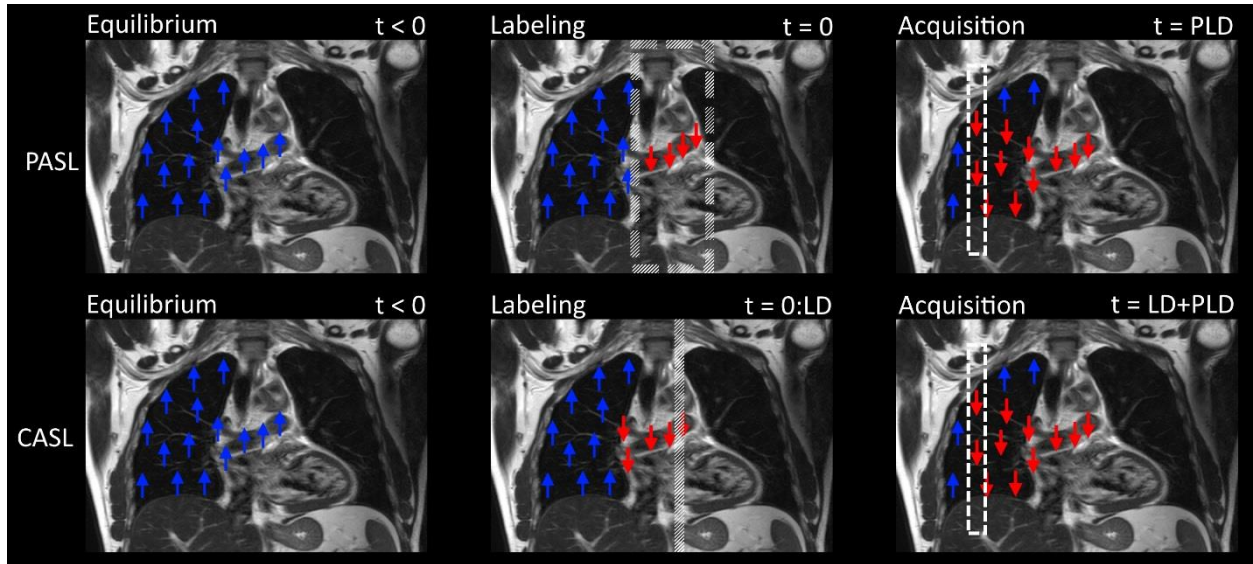


Figure 1.3: Pulsed-ASL (PASL) and Continuous-ASL (CASL) sequences in the lungs at three time points throughout the experiment: equilibrium, labeling, and acquisition. PASL labeling is applied with a single pulsed inversion covering the inflowing blood, while CASL labeling is applied continuously over the inflowing vessel (pulmonary artery) for a chosen label duration, LD. After a post-label delay (PLD) to allow labeled blood to perfuse the lungs, the image is acquired.

Pseudo-Continuous ASL

To achieve continuous labeling on clinical scanner hardware, pseudo-continuous ASL, or pCASL, was proposed by breaking up the RF pulse and gradient into a pulse train that reduces the RF duty cycle to be compatible with standard RF hardware [46] (Figure 1.4). The pCASL approach has become the standard ASL approach at many research institutions for brain perfusion imaging, and has been increasingly used for kidney perfusion imaging by labeling the descending aorta [34, 35]. Due to its theoretical SNR advantage over PASL approaches and ease of implementation on

clinical hardware, pCASL became the recommended brain perfusion ASL technique in a consensus by the International Society for Magnetic Resonance in Medicine (ISMRM) Perfusion study group [53], and has largely replaced CASL.

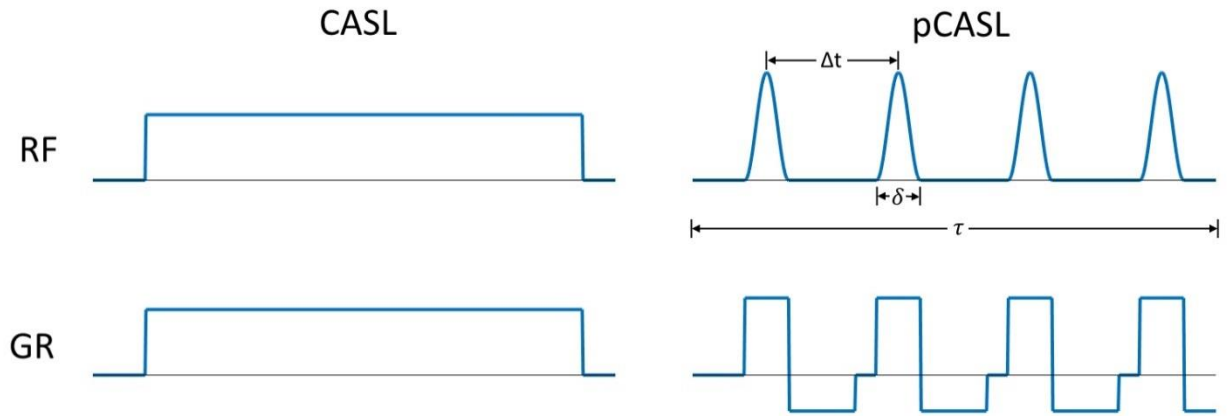


Figure 1.4: RF and gradient diagram for Continuous ASL (CASL) and pseudo-Continuous ASL (pCASL), with reduced RF duty cycle to allow continuous labeling on standard RF amplifiers.

1.4.3 Perfusion Quantification

A significant benefit of ASL is that absolute perfusion can be quantified, allowing for the meaningful comparison of perfusion images acquired over time. Such comparison is crucial for monitoring of disease progression and treatment response assessment, and for cross-center validation. The ASL perfusion model [31] is also independent of an assumed arterial input function, which is required for quantification of DCE perfusion images. The use of water as a freely-diffusible tracer also allows for the measurement of signal proportional to the true tissue perfusion without influence from vascular permeability [14].

To quantify ASL images, the subtracted perfusion-weighted image (ΔM) is normalized by a proton-density image (M_0), which is acquired using the same imaging parameters as the ASL

sequence without any presaturation or labeling pulses. The quantification equations for pulsed-ASL and continuous-ASL are shown in Equation 1.1 and 1.2 below. The evolution of the blood magnetization over time is accounted for in the label duration (τ), post-label delay (w) or inversion time (TI), and the transit delay from the labeling plane to the tissue (δt). λ is the blood-tissue partition coefficient in mL/g, T_1 is the longitudinal relaxation rate, and α is the labeling inversion efficiency, which is typically assumed based on simulations [54], though strategies to measure the true inversion efficiency for improved quantification have been explored [55, 56]. Perfusion is typically reported in units of mL/100g/min, or blood flow per mass of tissue.

$$f = \frac{\Delta M}{M_0} \cdot \frac{\lambda}{2 \cdot TI \cdot \alpha \cdot e^{\left(\frac{-TI}{T_{1,blood}}\right)}} \quad \text{[Equation 1.1]}$$

$$f = \frac{\Delta M}{M_0} \cdot \frac{\lambda}{2 \cdot \alpha \cdot T_{1,tissue}} \cdot \frac{1}{e^{\left(\frac{-\delta t}{T_{1,blood}}\right)} \cdot (1 - e^{\left(\frac{-\tau}{T_{1,tissue}}\right)}) \cdot e^{\left(\frac{-(w-\delta t)}{T_{1,tissue}}\right)}} \quad \text{[Equation 1.2]}$$

The accuracy and precision of quantitative pCASL perfusion measurements has been validated in normal and disease states with the gold-standard ^{15}O PET [57, 58]. A comparison of the precision of various spin labeling approaches showed excellent reproducibility with pCASL [59], suggesting that pCASL could potentially play a significant role in non-invasive clinical perfusion measurements.

1.5 Objectives

The various spin labeling approaches described above have almost exclusively been applied to brain perfusion imaging. The small number of ASL body applications is likely due to the straightforward labeling of the carotid arteries and the significant challenges introduced by respiratory motion and other physiological noise. Nevertheless, ASL has significant potential for body perfusion imaging, and has been demonstrated in a limited number of research studies in the lungs [41, 42, 60]. Once ASL is well established for pulmonary perfusion imaging, it would provide a valuable non-invasive clinical tool to detect and track progression of chronic lung conditions. Therefore, the overall aim of this dissertation is to develop robust non-contrast volumetric quantitative perfusion imaging of the lungs using MRI. Each chapter of the dissertation outlines various developments made towards this goal.

Chapter 2 discusses the initial feasibility and reproducibility of quantified perfusion of the pulsed-ASL technique, FAIR, for lung perfusion imaging at 3T. Chapter 3 further develops the FAIR technique to include complete lung coverage, as well as making the technique more robust for lung imaging using background suppression and inflow saturation.

Lung perfusion imaging using pCASL for improved SNR is proposed in Chapter 4, where different labeling approaches are explored in normal volunteers, and some of the technical challenges are addressed to make pCASL imaging in the lungs more robust.

Following the successful application of pCASL in healthy volunteers, we identified one of the labeling approaches studied in Chapter 4 that could be potentially useful in understanding the abnormal blood flow patterns found in pediatric patients with Fontan circulation. In Chapter 5, we

demonstrate labeling strategies to understand blood flow and measure lung perfusion in these patients.

Initial lung ASL perfusion imaging experiments were performed using 2D acquisitions, largely due to simplicity and ease of reproducibility compared to our experience with 3D acquisitions. However, in order to detect regional perfusion deficits, volumetric mapping of perfusion across the entire lung is desirable. Chapter 6 describes a proposed view ordering modification (CASPR) to the standard linear 3D TSE to make the acquisition more robust for ASL perfusion imaging in the body.

For ASL to be accepted as a viable alternative approach to the established clinical perfusion imaging methods, it must be proven to be accurate and reproducible, regardless of the field strength or scanner manufacturer. Chapter 7 describes the development of a quality control perfusion phantom to be used as a quality assurance test of the precision and repeatability of ASL perfusion measurements.

Finally, Chapter 8 summarizes the work presented in this dissertation, and offers insight into the future work required for ASL to become standard in the clinical assessment of chronic lung disease.

CHAPTER 2

NON-CONTRAST QUANTITATIVE PULMONARY PERFUSION USING FLOW

ALTERNATING INVERSION RECOVERY AT 3T*

2.1 Introduction

Flow Alternating Inversion Recovery (FAIR) is a pulsed-ASL technique has been extensively studied for pulmonary perfusion imaging at 1.5 Tesla (T) [41-43, 60, 61]. This inversion recovery-based technique creates perfusion-weighted images by applying a selective inversion pulse covering only the imaging region for a control image, and a non-selective inversion to invert all inflowing blood for a label image. The difference between these two images will be proportional to the perfusion in the imaging plane. Despite being extensively studied in research environments, the clinical application of FAIR has been limited to 1.5T due to its reduced SNR. Extending the FAIR technique to 3T should provide increased SNR due to the higher field strength and prolonged T1 of blood [62]. This increase in SNR was confirmed to be significant in brain perfusion imaging at 3T [63], however, pulmonary perfusion imaging using FAIR at 3T has never been demonstrated. Thus, the purpose of this study was to demonstrate the feasibility of non-contrast quantitative pulmonary perfusion imaging at 3T using FAIR, and to evaluate the intra-session and inter-session reliability of FAIR measurements at 3T.

* This work was published in Magnetic Resonance Imaging [61]. Portions of this work were presented at the 25th annual meeting of the International Society for Magnetic Resonance in Medicine (ISMRM) in Singapore (May 2016) and at the 102nd annual meeting of the Radiological Society of North America (RSNA) in Chicago (November 2016).

2.2 Methods

This was a prospective, HIPAA-compliant study, approved by the institutional review board. All subjects provided written informed consent prior to their participation in the study. Nine healthy volunteers (age 42 ± 17 years; 6 men 41 ± 17 years and 3 women 42 ± 20 years) participated in the study. As part of a broader pulmonary perfusion study, these subjects were also imaged using SPECT perfusion. Additionally, four healthy volunteers (age 42 ± 14 years; one 59-year-old man and 3 women 36 ± 9 years) were recruited to evaluate the intra-session and inter-session reliability of FAIR measured pulmonary perfusion at 3T.

2.1.1 MR Imaging

All MR imaging was performed on a 3T Ingenia scanner (Philips Healthcare, Best, The Netherlands) using our own implementation of the FAIR sequence. Subjects were positioned in the magnet head-first, supine, with the anterior torso coil, along with respiratory bellows and leads for ECG gating. The FAIR sequence began by saturating the imaging region, followed by labeling with a pair of slice-selective and slab-selective inversions in successive repetitions, using a hyperbolic secant pulse centered on the imaging region (Figure 2.1). The slice-selective inversion thickness was set to three times the imaging plane thickness to ensure complete inversion of the spins in the imaging plane (control image) and the slab-selective inversion was set to ten times the slice-selective inversion (label image). A post-labeling delay of one cardiac period (e.g. 1 second for a heart rate of 60 beats per minute) was used to allow labeled blood to perfuse the lungs [60]. A single-shot turbo spin echo (SShTSE) readout with partial Fourier along the phase encoding direction was used to minimize the sensitivity to B_0 inhomogeneities that are encountered at air/tissue interfaces in the lungs. The FAIR sequence was cardiac-triggered using ECG to ensure

diastolic acquisition in the following cardiac cycle to minimize signal variations due to pulsatile flow [60].

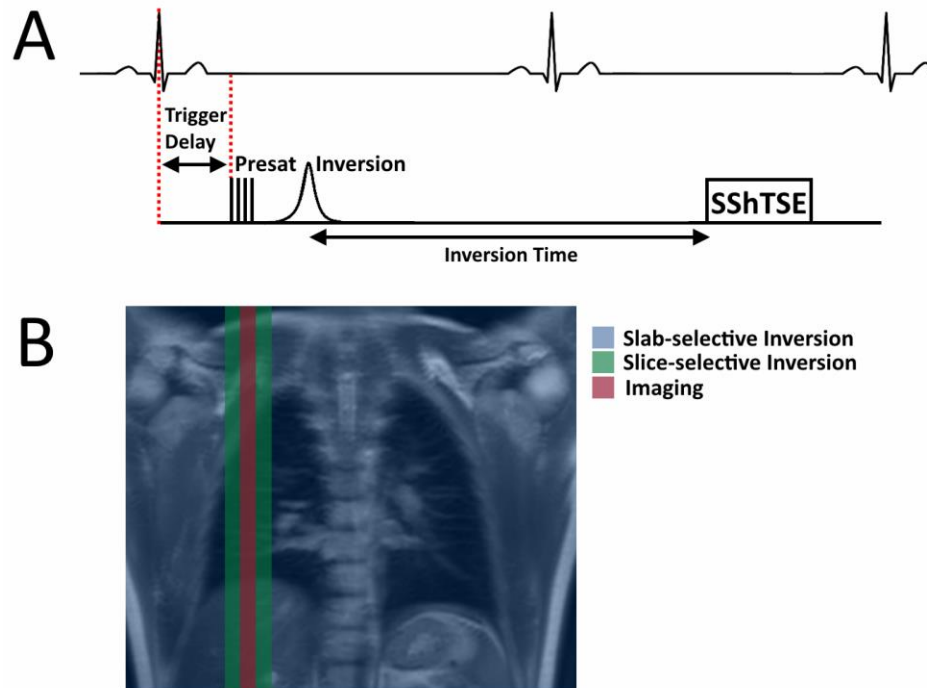


Figure 2.1: Schematic of the ECG-triggered FAIR sequence. (A) On cardiac trigger, the pre-saturation followed by slice/slab selective inversion pulses are applied. After an inversion delay (e.g. 1 R-R interval), data are acquired using a SShTSE acquisition during the diastolic phase of the subsequent cardiac cycle. (B) Schematic of the coronal image showing the sagittal imaging slice (red), slice-selective inversion [64] and slab-selective inversion (blue).

Three pairs of control/label images of a single slice were acquired within an 18 second end-expiration breathhold acquisition using the following parameters: repetition time (TR) = 3 sec; TE = 46 ms; $3 \times 3 \text{ mm}^2$ in-plane resolution; 15 mm slice thickness; 544 Hz/pixel bandwidth, 0.55 partial k-space factor. 2D sagittal and coronal perfusion images of a single slice were acquired in separate breathhold acquisitions for each volunteer. The sagittal imaging plane was positioned over the lateral right lung to avoid the larger vessels of the pulmonary artery, and the coronal imaging plane

was positioned posterior to the descending aorta. The field of view (FOV) was subject specific and typically varied between 250-340 mm along F/H, 180-320 mm along A/P for sagittal acquisitions and 315-360 mm along R/L for coronal acquisitions. Perfusion weighted images were reconstructed using complex k-space subtraction between the label and the control images followed by fermi filtering, homodyne reconstruction, and corrections for coil sensitivity, implemented in MATLAB (The Mathworks, Natick, MA) [35]. Subsequently, a proton density weighted image was acquired using the same acquisition parameters but without any preparation pulses in a separate breathhold for perfusion quantification (see below).

To validate the FAIR measured perfusion (or capillary blood flow), the right pulmonary artery (RPA) flow was measured using a gradient echo based phase contrast (PC) technique acquired in a single slice perpendicular to the main trunk of the RPA. T2-weighted images acquired in the axial and coronal planes, prior to the PC measurement, were used for this planning. Measurements were made over one cardiac cycle in a 15 second breathhold using the following parameters: TR = 4.7 ms; TE = 2.9 ms; 1.7×1.7 mm² in-plane resolution; 5 mm slice thickness; 32 cardiac phases; 721 Hz/pixel bandwidth. A Venc of 130 cm/sec [65] was used in all subjects to achieve aliasing free PC measurement in the RPA.

The intra-session and inter-session reliability of FAIR-measured pulmonary perfusion were assessed in four additional healthy volunteers in the right lung. After the acquisition of the anatomical images and PC-measured flow in the RPA, FAIR perfusion measurements of the right lung were performed twice in a sagittal orientation, each in a 18-second breathhold acquisition (for intra-session). Subsequently, the subject was removed from the scanner table and asked to sit up after removing the anterior torso coil and the respiratory bellows. After a five-minute delay, the

subject was repositioned in the scanner with a new landmark. Immediately afterwards, the PC followed by FAIR measurements in the right lung were performed twice again in the sagittal orientation.

2.1.2 FAIR Perfusion Quantification

The FAIR perfusion difference image (ΔM) was used to calculate the absolute quantitative perfusion (f) using equation 1 [60], where λ is the tissue-blood partition coefficient of water, assumed to be 0.95 mL/g [43], TI is the inversion time, $T_{1,\text{blood}} = 1660$ ms at 3T [66]. The proton density (M_0) value of blood was chosen from a region of interest [67] drawn over a large vessel in the proton density weighted image. The quantitative perfusion from in mL/mL/min was converted to the standard units of mL/100g/min by assuming a 0.33 g/mL lung tissue density [60].

2.1.3 SPECT Perfusion

All of the SPECT imaging was performed on a SPECT/CT system (Symbia T6; Siemens Healthcare; Erlangen, Germany). The subjects were positioned supine with arms raised above the head. Using the standard clinical protocol, the subjects were injected intravenously with 185 MBq technetium-99m-macroaggregated albumin ($^{99\text{m}}\text{Tc-MAA}$), prepared using $^{99\text{m}}\text{Tc}$ (Mallinckrodt Pharmaceuticals; Dublin, Ireland) and a commercial MAA kit (Jubilant DraxImage Inc.; Kirkland, Canada). SPECT perfusion images were acquired immediately after the radiotracer injection in approximately 10 minutes of free breathing using 3° angle steps over 180° ; high-resolution low-energy collimators; 128×128 matrix size; spatial resolution of $5 \times 5 \times 5$ mm³; at 15 seconds per frame. The images were reconstructed online with attenuation correction and exported for analysis.

2.1.4 Image Analysis

For each subject, quantitative tissue perfusion values (Equation 1.1) were measured from FAIR images using a ROI drawn over the entire lung. The quantitative perfusion measurements were performed again by removing the larger pulmonary vessels using a mask based on a perfusion threshold to minimize the contribution of larger pulmonary vessels to the tissue perfusion measurement. The perfusion threshold was manually selected for each subject based on the bright vascular signal that was easily distinguishable from tissue perfusion. The perfusion threshold across all subjects was 1100 ± 280 mL/100g/min. The quantitative FAIR perfusion measurements, both with and without larger pulmonary vessels, were correlated to PC measured blood flow averaged across one cardiac cycle in the RPA using Pearson's correlation. Relative dispersion (RD), defined as the ratio of the standard deviation to the mean was also measured in FAIR perfusion images and compared against SPECT perfusion, to validate the quantitative measures between the two modalities [68]. The SPECT ROI was similarly drawn over the entire lung in a 2D slice matching the FAIR image location. The intra-session and inter-session reliability measurements of quantitative FAIR perfusion were assessed using intra-class correlation coefficient (ICC) and Bland-Altman analysis. All statistical analyses were performed using GraphPad Prism version 6.07 (GraphPad, La Jolla, CA) with $p < 0.05$ considered statistically significant.

2.2 Results

2.2.1 FAIR Perfusion

FAIR perfusion images were successfully acquired in all subjects. The current implementation at 3T allowed acquisition of FAIR perfusion images in multiple orientations

without image degradation (Figure 2.2, top row). The blood signal from the proton density image allowed the calculation of absolute perfusion quantification (Figure 2.2, bottom row). The mean lung perfusion value measured across all subjects was 858 ± 605 mL/100g/min. With the removal of the signal from the larger pulmonary vessels, the mean lung perfusion decreased to 629 ± 294 mL/100g/min, showing tissue perfusion within the expected range of normal subjects (Table 2.1) [60]. The highly vascular structures of the lungs combined with the increased sensitivity of SSHTSE acquisitions to the cardiac cycle provided varying contributions of the large vessels to lung perfusion measurements. Across all subjects, however, the FAIR measured perfusion in the right lung including pulmonary vessels correlated significantly with the phase contrast measured blood flow in the RPA ($r=0.62$; $p<0.01$) and improved for measures without vessels ($r=0.73$; $p<0.001$) (Figure 2.3), providing a validation to the measurement of the lung perfusion.

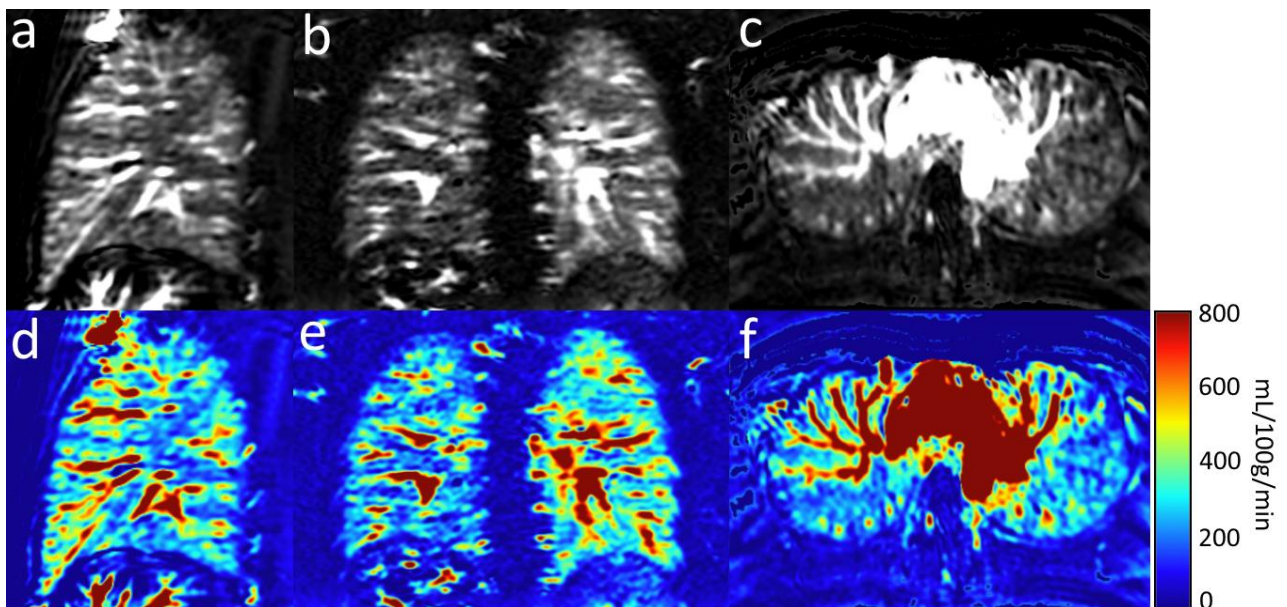


Figure 2.2: FAIR perfusion-weighted images (a-c, top row) and reconstructed quantitative perfusion maps (d-f, bottom row) in the sagittal (a,d), coronal (b,e), and axial (c,f) orientations in a 29-year old healthy male volunteer.

Table 2.1: FAIR-measured quantitative pulmonary perfusion and SPECT perfusion measurements

Subject	Age	Gender	FAIR (ml/100g/min)		FAIR (ml/100g/min)		SPECT (a.u.)	
			With vessels	Without Vessels	With vessels	Without Vessels	Mean \pm SD	RD
1	28	F	481 \pm 633	1.31	319 \pm 206	0.65	6026 \pm 1454	0.24
2	37	M	887 \pm 744	0.84	636 \pm 397	0.62	4605 \pm 888	0.19
3	33	M	769 \pm 655	0.85	647 \pm 438	0.68	5765 \pm 1593	0.28
4	67	M	600 \pm 419	0.70	426 \pm 190	0.45	7111 \pm 2284	0.32
5	27	M	699 \pm 593	0.85	469 \pm 248	0.53	4133 \pm 991	0.24
6	28	M	864 \pm 636	0.74	566 \pm 276	0.49	4430 \pm 917	0.21
7	65	F	441 \pm 282	0.64	363 \pm 170	0.47	5144 \pm 1305	0.25
8	33	F	852 \pm 447	0.52	525 \pm 293	0.56	9757 \pm 2524	0.26
9	59	M	589 \pm 502	0.85	484 \pm 307	0.64	4387 \pm 1059	0.24

2.2.2 FAIR Perfusion vs. SPECT Perfusion

The average time between the MRI and SPECT perfusion examinations was approximately 2:10 \pm 1:42 (hours:minutes). In all subjects, the FAIR measured perfusion matched qualitatively to SPECT perfusion. For example, Figure 2.4 shows coronal images of a healthy volunteer, exhibiting similar tissue perfusion distribution between FAIR and SPECT measurements. The signal in the larger vessels on the FAIR perfusion MRI matches regions of photopenia on SPECT perfusion (Figure 2.4, arrows). Similar qualitative matching can be found in a different subject acquired in a sagittal orientation (Figure 2.5). With the removal of the signal from the larger pulmonary vessels on the FAIR perfusion image, the resulting FAIR lung perfusion exhibited more

similarities with the SPECT perfusion (Figure 2.6). The median RD of SPECT perfusion across all subjects was measured to be 0.23 (mean±SD: 0.25±0.04). The median RD of FAIR perfusion across all subjects was 0.73 (mean±SD: 0.81±0.22). After the removal of signal from the larger pulmonary vessels, the median RD of FAIR lung perfusion was reduced to 0.49 (mean±SD: 0.56±0.08), thus exhibiting more homogeneous perfusion, similar to those of SPECT perfusion. These RD values are in agreement with the values reported previously [42], both with and without masking of the pulmonary vessels.

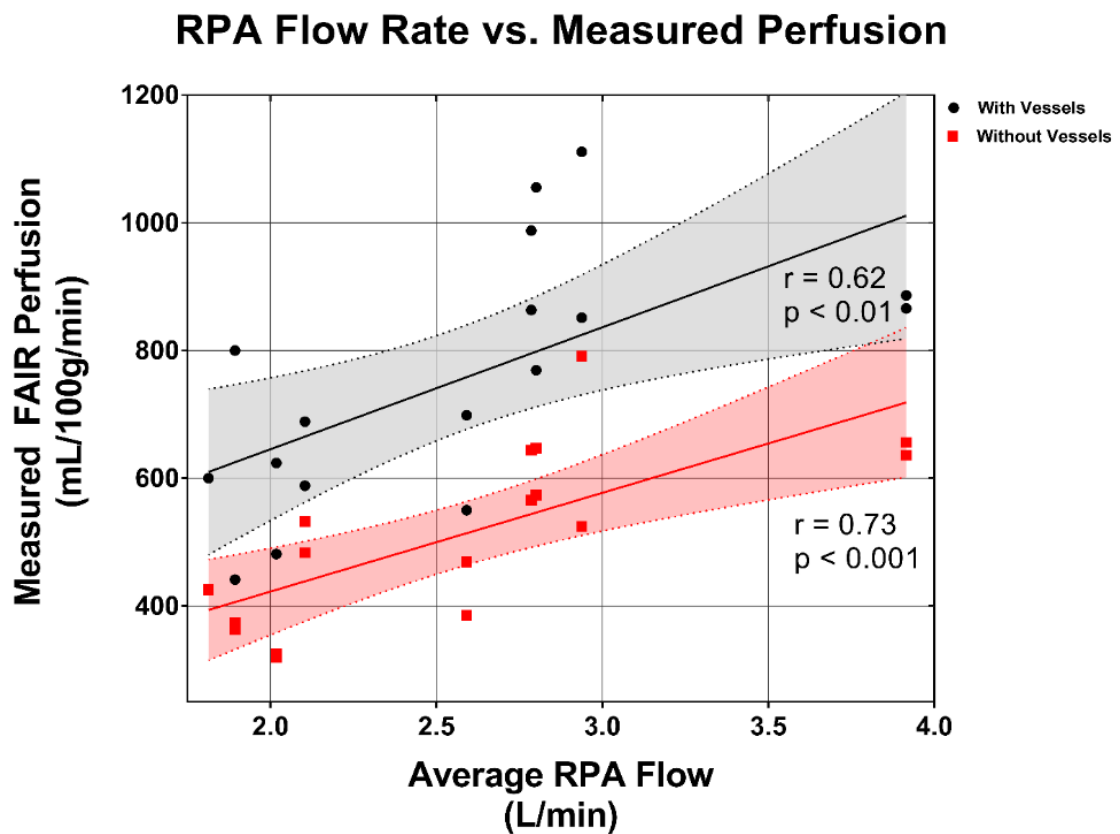


Figure 2.3: Average flow rate in the right pulmonary artery (RPA) measured using phase contrast (PC) vs. pulmonary perfusion measured in the right lung using sagittal and coronal FAIR images in nine subjects, showing a moderate correlation. A coronal image was not acquired in one of the volunteers.

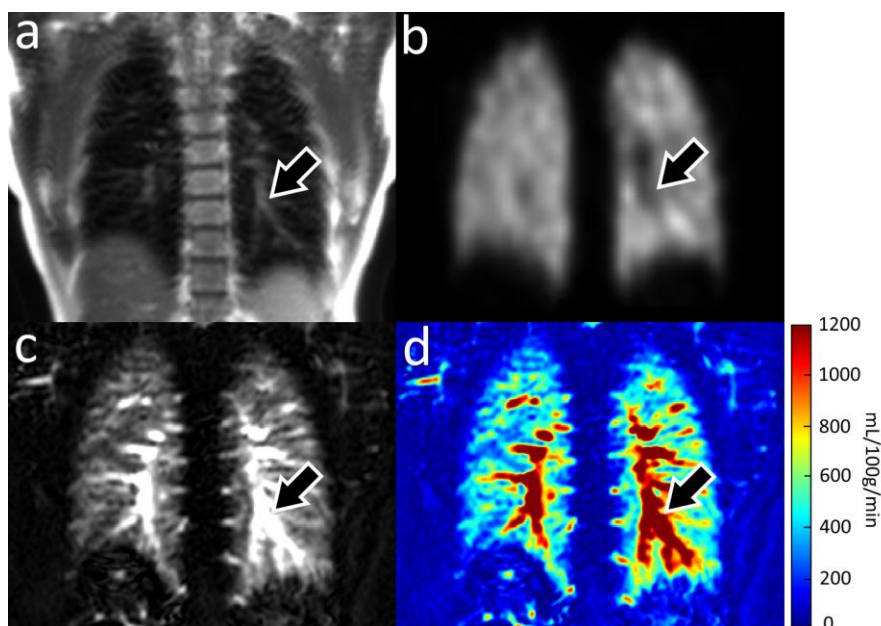


Figure 2.4: Coronal proton density weighted image (a), SPECT perfusion image (b), FAIR perfusion-weighted image (c), and reconstructed perfusion map derived from FAIR perfusion (d) in a 33-year old healthy female volunteer. Arrows indicate signals from major vessels that are visible on FAIR perfusion images (c,d), and seen as regions of photopenia on SPECT images (b).

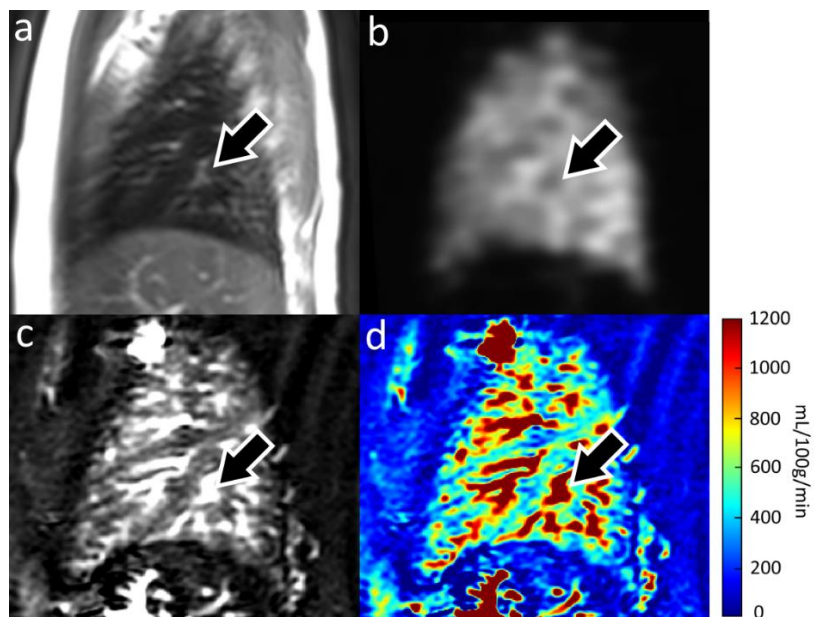


Figure 2.5: Sagittal proton density weighted image (a), SPECT perfusion image (b), FAIR perfusion-weighted image (c), and reconstructed perfusion map derived from FAIR perfusion (d) in a 28-year old healthy male volunteer. Arrows indicate signals from major vessels that are visible on FAIR perfusion images (c,d), and seen as regions of photopenia on SPECT images (b).

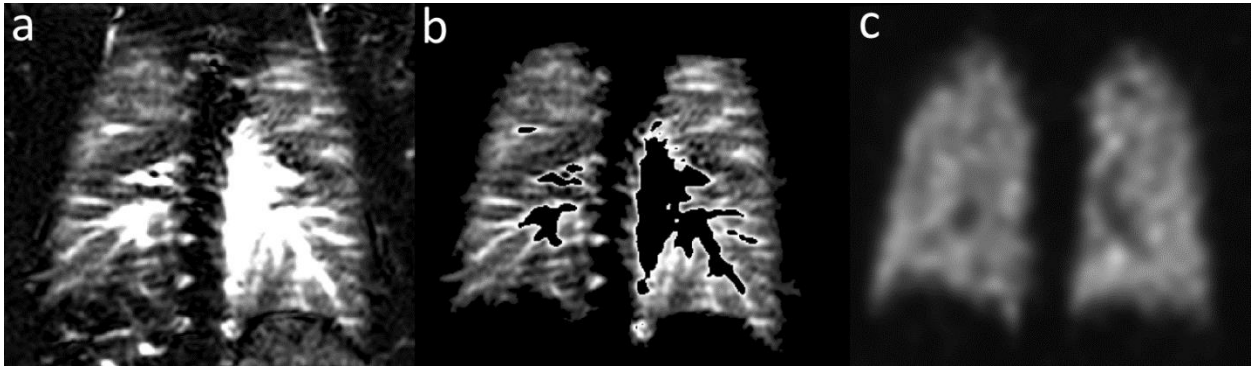


Figure 2.6: Coronal FAIR perfusion-weighted image (a) shows significant signal from the major pulmonary vessels. When masked using a threshold (e.g. >1000 ml/100g/min), the FAIR perfusion-weighted image (b) shows parenchymal perfusion, matching more closely the SPECT perfusion (c). These images were acquired in a 27-year old male healthy volunteer.

2.2.3 Reliability of FAIR Perfusion

Figure 2.7 shows the Bland-Altman plots for the intra-session and inter-session repeatability measurements of FAIR perfusion in four healthy volunteers, measured twice within each subject (Table 2.2). The average delay between intra-session measurements was 180 ± 60 seconds and between inter-session measurements was 35 ± 12 minutes. The intra-session reliability of FAIR perfusion, measured by ICC was 0.95 (Figure 2.7a), which increased to 0.96 with the removal of the signal from the larger pulmonary vessels (Figure 2.7b). The ICC measured inter-session reliability was 0.59 (Figure 2.7c), which increased to 0.72 with the removal of the signal from the larger pulmonary vessels (Figure 2.7d).

2.3 Discussion

Although nuclear imaging examinations (i.e. SPECT/CT) are currently the established techniques to measure pulmonary perfusion, they suffer from limited spatial resolution and exposure to ionizing radiation. Non-contrast pulmonary perfusion using arterial spin labeled [55]

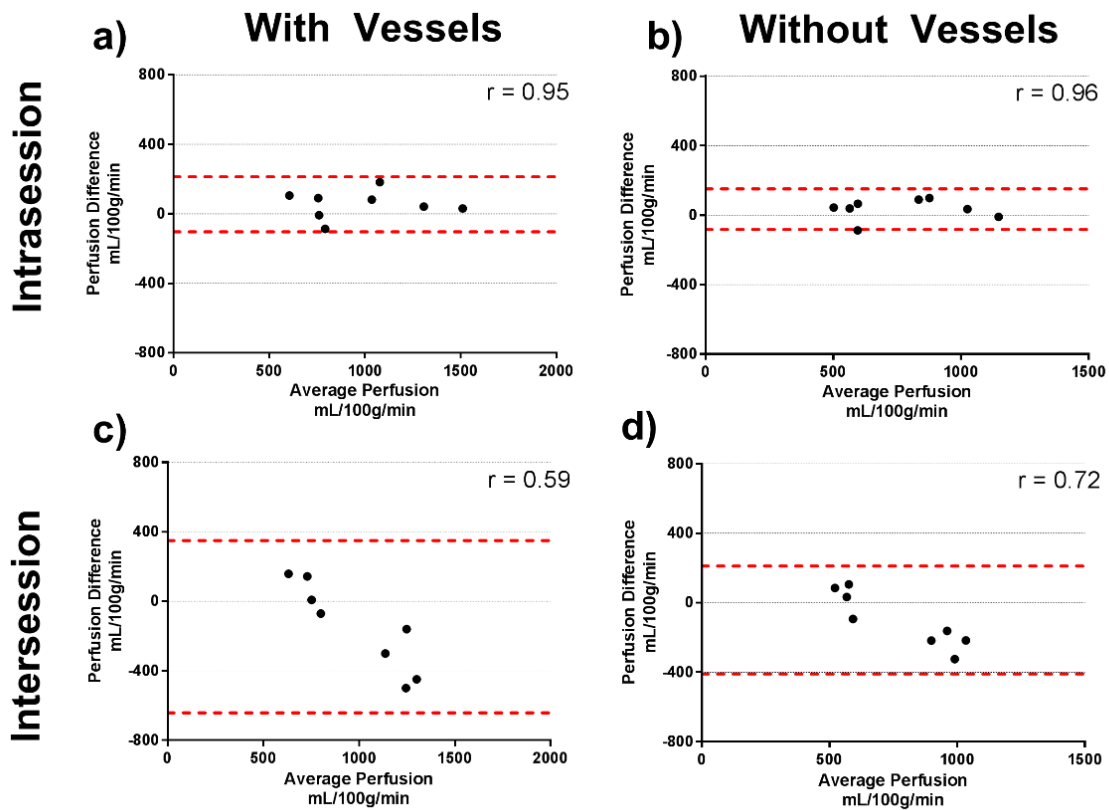


Figure 2.7: Bland-Altman plots to assess intra-session (top row) and inter-session (bottom row) reliability of FAIR measured pulmonary perfusion, with vessels (left column) and without vessels included in the region of interest (right column). The intra-class correlation coefficients (ICC) are shown on the plots. Four subjects scanned twice each for intra-session and inter-session measurements are shown on the plots.

MRI (i.e. FAIR) has been developed at 1.5T as an alternative technique due to its ability to perform repeated measurements without the exogenous contrast agent. However, the clinical applicability of FAIR has been limited at 1.5T due to its reduced signal-to-noise ratio (SNR), and the extension of this technique to 3T MRI scanners are lacking. Furthermore, the availability of 3T scanners in the clinical settings has been steadily increasing over the past decade. In this study, we performed the initial evaluation of a FAIR based non-contrast pulmonary perfusion acquisition at 3T including the assessment of intra-session and inter-session reliability and compared the FAIR

perfusion measurements against clinical standard SPECT perfusion values. To the best of our knowledge, this is the first study of FAIR measured quantitative pulmonary perfusion at 3T.

Table 2.2: FAIR quantitative pulmonary perfusion test/retest measurements in four additional healthy volunteers

			FAIR (ml/100g/min)				FAIR (ml/100g/min)			
			With Vessels				Without Vessels			
			Measurement 1		Measurement 2		Measurement 1		Measurement 2	
Subject	Age	Gender	Mean \pm SD	RD	Mean \pm SD	RD	Mean \pm SD	RD	Mean \pm SD	RD
10	41	F	711 \pm 365	0.51	801 \pm 419	0.52	564 \pm 223	0.40	628 \pm 235	0.37
11	41	F	995 \pm 415	0.42	1076 \pm 424	0.39	828 \pm 254	0.31	925 \pm 270	0.29
12	59	M	836 \pm 551	0.66	748 \pm 471	0.62	639 \pm 275	0.43	551 \pm 225	0.40
13	25	F	1287 \pm 789	0.61	1328 \pm 725	0.54	1009 \pm 389	0.39	1042 \pm 403	0.38

FAIR measured pulmonary perfusion in the right lung correlated significantly with the PC measured average blood flow in the RPA. This correlation increased with the removal of the blood flow signal within major pulmonary vessels, likely due to the signal variations in these major vessels introduced by the cardiac cycle. With the removal of these major vessels, the remaining tissue signal represented true parenchymal perfusion. In our preliminary experience, the manually selected threshold to mask the larger pulmonary vessels provided consistent results among all subjects compared to statistics-based methods [42]. This is currently being investigated including methods to prospectively suppress the blood vessel signal using inflow saturation [69]. This should also reduce the contribution of large blood volume signal to the pulmonary perfusion measurements, which should be nominally about 500-600 ml/100g/min. To further minimize the

variations due to cardiac motion that are more pronounced in the left lung, the test/retest measurements in this study were performed in the right lung.

Although MR measured pulmonary perfusion using FAIR exhibited similarities qualitatively with ^{99m}Tc -MAA based SPECT perfusion, the quantitative comparison between these two modalities is challenging [25]. The physiological interpretation of these two modalities is different: MR based perfusion (either measured using FAIR or Fourier Decomposition [25]) shows the amount of blood that perfuses pulmonary parenchyma, while the SPECT perfusion is proportional to the amount of blockage in the capillaries by ^{99m}Tc -MAA [70]. Although these effects are visually similar in the capillaries and provide diagnostic information [25], the major discrepancy is noticed in the large vessels (e.g. Figure 2.4, Figure 2.5). Several methods have been proposed to remove the signal from the large pulmonary vessels during post-processing to reflect the pulmonary perfusion [42, 71]. Nevertheless, the signal in the major vessels measured on MRI could be useful to detect large intravascular thrombi in patients with acute pulmonary embolism in addition to the pulmonary perfusion measurement.

FAIR based non-contrast pulmonary perfusion also has several advantages compared to SPECT perfusion. In addition to the lack of ionizing radiation, FAIR does not depend upon the availability of radioactive materials or exogenous contrast agents. It also reduces the total imaging procedure times. Currently, the SPECT perfusion imaging takes approximately 10 minutes of continuous acquisition time during free breathing combined with the intravenous injection of ^{99m}Tc -MAA. Compared to that, FAIR requires a single 18-second breathhold with three signal averages to acquire a single 15 mm thick slice. Covering the entire lung would require approximately 8-10 slices, with a total acquisition time of 3-5 minutes. This can be combined with

additional morphological imaging as well as cardiac functional imaging for a comprehensive cardiopulmonary examination using a whole-body 3T clinical MR scanner. Further, the quantitative assessment of pulmonary perfusion using FAIR provides an objective quantitative measurement for the assessment and longitudinal monitoring of chronic lung disease. This will be particularly beneficial to observe the lack of regional perfusion in interstitial lung disease, asthma, cystic fibrosis and COPD and improvements with targeted treatments without the concerns of exposure to ionizing radiation or exogenous contrast agents.

There are several limitations with our study. First, we only included the evaluation in a small number of healthy subjects, given the radiation associated to SPECT perfusion in our study. Despite the small cohort we found significant correlation between PC measured average blood flow and FAIR measured pulmonary perfusion. Additionally, the assumption of a constant lung density across all subjects may likely introduce error in quantification. This aspect of quantification could be strengthened by including an additional scan to estimate lung density [72]. Furthermore, our preliminary results in this initial feasibility study need further validation in a patient cohort. Our current evaluation was limited to a single slice acquired in a breathhold. However, in majority of the cases, a single signal average provided sufficient SNR to accurately quantify perfusion due to the inherent high SNR at 3T combined with complex subtraction. This could potentially allow for the acquisition of additional slices for more complete coverage of the lung perfusion during a breathhold, rather than acquiring multiple signal averages. Alternatively, triggered acquisitions using signals from either respiratory bellows or navigators could potentially allow for prolonged acquisitions for complete coverage of the lungs in approximately 3-5 minutes. This will allow the applicability of FAIR to patient studies, where larger volumetric coverage is

needed. Our study also lacked a direct comparison between the FAIR measured pulmonary perfusion at 3T vs 1.5T. However, we achieved sufficient SNR with FAIR images in 1-3 signal averages at 3T compared to 3-5 signal averages at 1.5T [42, 43] and 25 signal averages at 0.2T [73].

In summary, we have demonstrated the initial feasibility of non-contrast quantitative pulmonary perfusion using FAIR at 3T. This quantitative approach may be beneficial for assessing regional perfusion measurement in chronic lung disease to characterize and monitor treatment response without the concerns of repeated exposure to ionizing radiation or the accumulation of exogenous contrast agent.

CHAPTER 3

ROBUST NON-CONTRAST PERFUSION IMAGING OF WHOLE-LUNGS USING MULTI-SLICE FAIR AT 3T*

3.1 Introduction

The FAIR technique has been successfully applied at 3T for improved SNR [74], but has some disadvantages that, if improved upon, could make FAIR a more useful tool for clinical perfusion imaging. Respiratory motion and other physiological noise can introduce motion artifacts and other errors into the subtracted FAIR perfusion-weighted images. Background suppression, which was originally introduced to improve the SNR of MR angiograms [75], has been shown to be essential in improving the SNR of ASL perfusion images by significantly reducing background tissue signal [76], which then reduces subtraction errors caused by both physiological noise and motion artifacts, while retaining the ASL signal difference in the blood. FAIR images also contain characteristic bright signal in the larger pulmonary vasculature (Figure 2.6). This signal represents larger volumes of labeled blood that has pooled in the major vessels before reaching the capillaries, rather than actual perfusion, which obstructs the view of the underlying tissue perfusion. To remove this signal, pulmonary perfusion studies that use FAIR often apply perfusion threshold masks, calculated either manually [74], or with automated masking based on histogram curve fitting [42] or a percentage of the maximum signal intensity [77]. These masking approaches can successfully remove vascular signal to aid in quantitative perfusion

* This work is in preparation for publication submission. Portions of this work were presented at the 25th annual meeting of the ISMRM in Singapore (May 2016).

analysis, but they completely remove the underlying signal in the lungs, making assessment of perfusion deficits challenging. An alternate approach to reduce signal in the vasculature is inflow saturation [35], which saturates the perfusion signal further up the vascular tree, which arrives in the major vessels at the time of imaging. This technique can reduce bright vascular signal without masking the vessels or the underlying tissue perfusion, and should therefore make FAIR images better represent true pulmonary perfusion without contribution from pooled blood in the vasculature. Finally, perfusion imaging using FAIR has so far been limited to a single slice, limiting its applicability for clinical perfusion evaluation. Since chronic pulmonary diseases heterogeneously affect the lung, assessment of disease progression and treatment requires whole-lung perfusion imaging. The purpose of this study was to combine multi-slice (MS) FAIR for whole-lung coverage with inflow saturation to suppress signal from major pulmonary vasculature for improved visualization of perfusion, and optimize background suppression to minimize image misregistration artifacts and improve SNR.

3.2 Background Suppression

3.2.1 Theory

ASL is an inherently low SNR technique that measures only about a 1-2% change in signal relative to the equilibrium magnetization [45], rendering the technique sensitive to any additional sources of noise. Background suppression uses an even number of non-selective inversion pulses applied with optimized timings during the post-labeling delay to reduce the signal of background tissue within a wide range of T1 relaxation rates near the level of noise, while retaining the ASL signal difference. By nulling this background tissue signal, the resulting subtracted images will be

less sensitive to random noise and motion that may have occurred between control and label acquisitions. Figure 3.1 shows the signal evaluation of inflowing blood and background tissue signal throughout the FAIR sequence without (A) and with (B) background suppression applied.

The FAIR sequence begins with a saturation pulse over the imaging region, followed by a labeling inversion pulse, and a post-labeling delay before the acquisition. Blood magnetization during the control and label sequences is shown with blue and red, and a wide range of background tissues (T1 relaxation times from 200-4200ms) are shown by multiple other colors. Without background suppression (A), at the time of imaging, the background tissue has nearly recovered to equilibrium, leaving sufficient signal to introduce subtraction artifacts. By applying four optimally-timed background suppression inversion pulses during the post-labeling delay (B) [78], this wide range of T1 values can be significantly reduced at the time of image acquisition. Background suppression has proven effective in ASL imaging in the brain [76] and kidney [35], and is anticipated to be especially important in the lungs for reducing artifacts introduced by respiratory motion.

An example of the results of background suppression using a hyperbolic secant (HS) inversion pulse in a 2D slice are shown in Figure 3.2. (A) and (B) show the FAIR control and label source images without background suppression, and (C) shows the corresponding subtracted perfusion-weighted image. The control, label, and perfusion-weighted images with background suppression are shown in (D, E, and F). Pulmonary perfusion appears similar between the two acquisition strategies, but background suppression significantly reduced the artifacts caused by breathing, seen in the diaphragm (red arrow) and fat tissue (green arrow), and also reduced background signal variations at the edges of the field of view (FOV) (black arrow). Incomplete

background suppression can be seen in the fat tissue (blue arrow). While there was minimal subject motion in this case, this incomplete suppression could potentially result in subtraction errors due to respiratory motion, such as those seen near the diaphragm without background suppression.

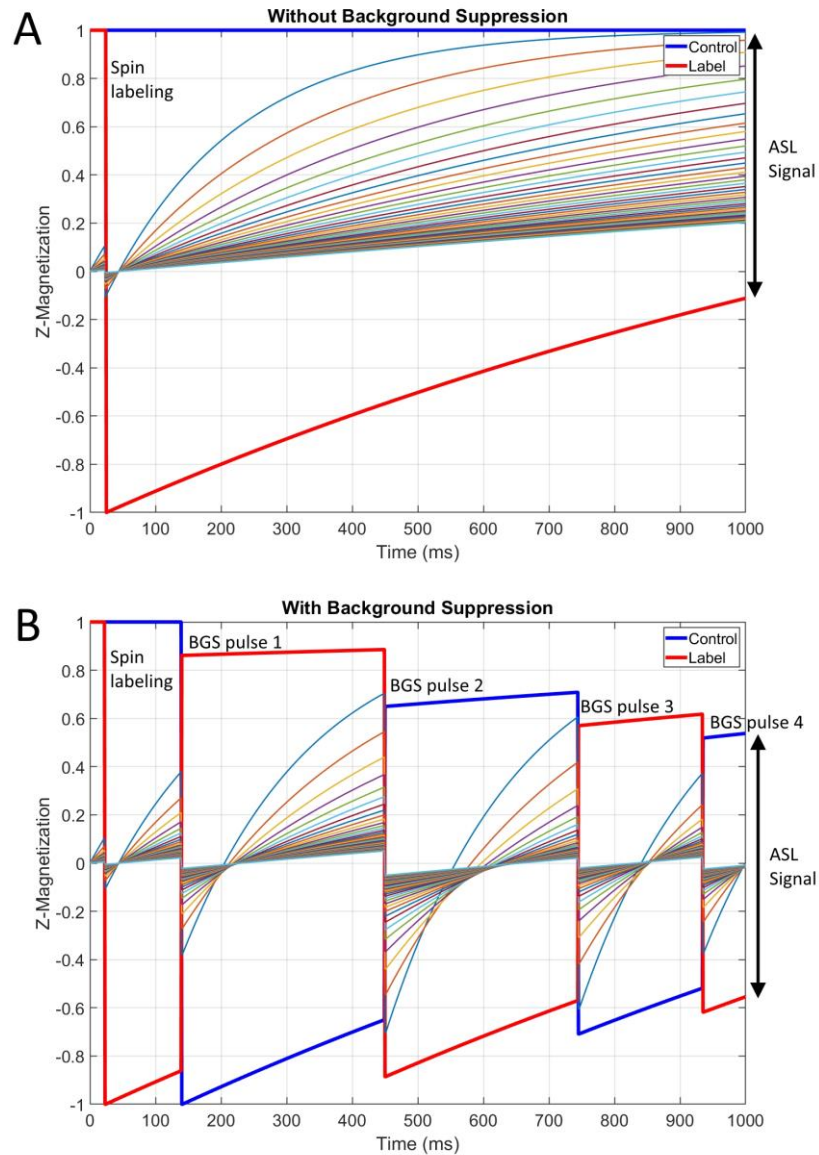


Figure 3.1: Evolution of the Z-magnetization of inflowing blood and background tissue throughout the FAIR sequence without (A) and with (B) four background suppression inversion pulses applied during the post labeling delay.

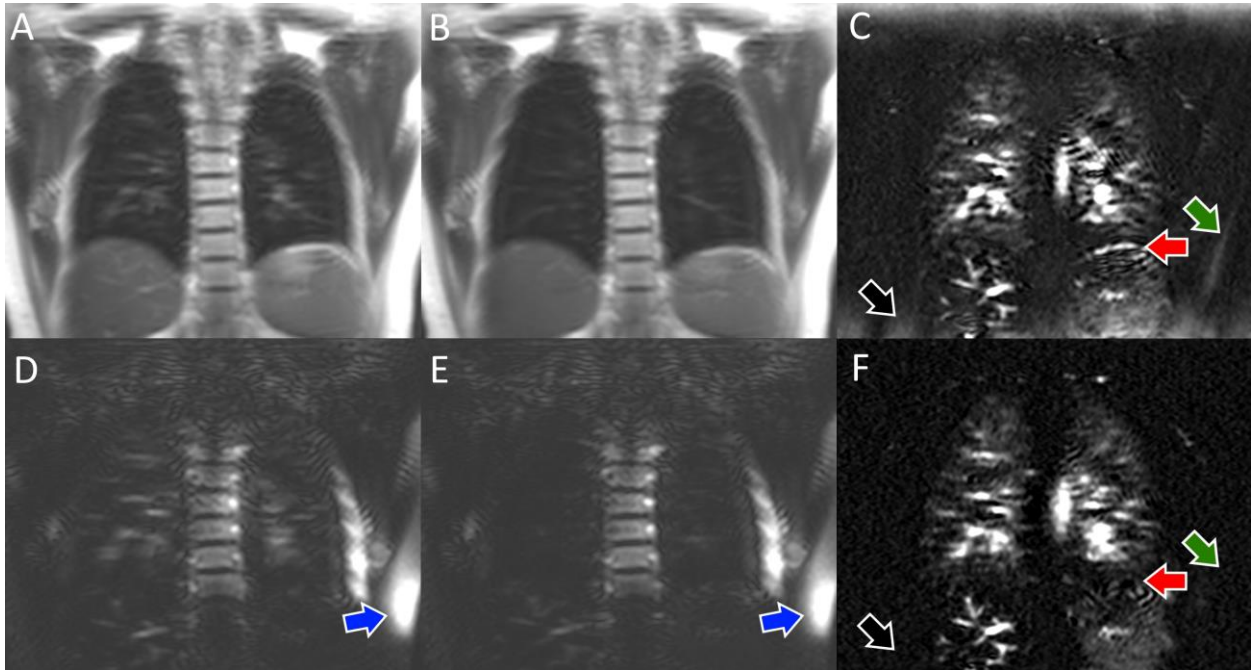


Figure 3.2: FAIR without background suppression: control image (A), label image (B), and perfusion-weighted image (C). FAIR with background suppression: control image (D), label image (E), and perfusion-weighted image (F). Red arrows indicate the reduction in background signal at the dome of the spleen due to image misregistration, even though these images were acquired in a breathhold. Blue arrows show failed background suppression in the fat in the source images, and green arrows show near the fat in the subtracted perfusion-weighted images.

3.2.2 Background suppression optimization

The failed suppression of the fat signal in Figure 3.2 can likely be attributed to off-resonance effects, resulting in the loss of efficiency of the background suppression inversion pulses. The standard hyperbolic secant pulse [54] implemented on the scanner has an approximate bandwidth of $\pm 450\text{Hz}$, which is sufficient for brain applications where very little fat is present. However, since the fat resonance (440Hz at 3T) is near the limit of this pulse's bandwidth, the fat suppression fails in the regions of increased B_0 inhomogeneities (Figure 3.3a). In body imaging

applications, the increased FOV and presence of abdominal fat introduce additional challenges due to increased B_0 inhomogeneities across the volume.

The bandwidth of the HS pulse can be broadened by modifying its shape (Figure 3.3 B, C) at the expense of raising the adiabatic threshold, which the B_1 field must exceed to achieve adiabatic inversion, making the pulse more sensitive to B_1 variations. The C-FOCI adiabatic inversion pulse has been shown to be more robust to B_0 and B_1 variations for fat suppression (Figure 3.3 D) [79], and should therefore have a higher inversion efficiency in areas of increased field inhomogeneities for background suppression applications. Both pulses were implemented for background suppression using automatically calculated timings for the chosen inversion time [78] to assess suppression performance in fat in a 2D slice, and later for multi-slice coverage of the lung.

The performance of the HS and C-FOCI background suppression inversion pulses is shown in the FAIR control source images in Figure 3.4. The HS pulse (Figure 3.4 A) leaves residual unsuppressed signal in regions of fat tissue, similar to the failed suppression in Figure 3.2 (D, E). The C-FOCI pulse (Figure 3.4 B) completely suppresses the background signal across the imaging slice.

3.3 Inflow Saturation

Signal from labeled blood in the major pulmonary vasculature can be suppressed by saturating the tail end of the inflowing perfusion bolus that flows into the vessels towards the end of the post-label delay. This results in a labeled bolus with a well-defined duration [80], which can be tailored to appear further down the vascular tree, reducing signal in the larger vessels, thus improving the

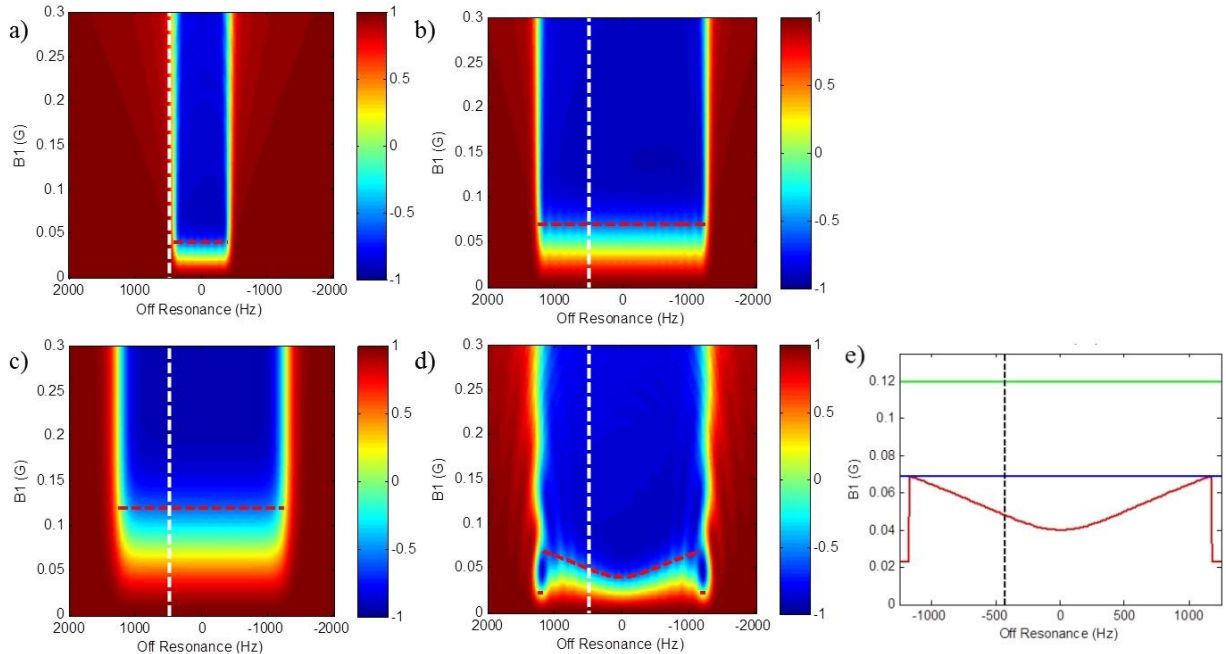


Figure 3.3: the Bloch equation simulation results: (a) HS ($\beta = 4, \mu = 6$); (b) HS ($\beta = 4, \mu = 18$); (c) HS ($\beta = 12, \mu = 6$) and (d) C-FOCI ($\beta = 4, \mu = 6$ and $C_{\max} = 3$). The red dashed line shows adiabatic threshold at different off-resonance. The white dashed line shows the fat resonance frequency at 3T. (e) Compares the adiabatic thresholds of C-FOCI (red), HS ($\beta = 4, \mu = 18$, blue) and HS ($\beta = 12, \mu = 6$, green).

visualization of true perfusion. To assess the effectiveness of this technique for pulmonary perfusion imaging with the 2D FAIR technique described in Chapter 2, three equally-spaced saturation pulses were applied over the inflowing blood adjacent to the imaging region during the final 500ms prior to the image acquisition. The FAIR perfusion images acquired with inflow saturation (Figure 3.5) contained reduced signal in the major vasculature, including in the aorta and larger pulmonary vessels, allowing for better evaluation of the pulmonary parenchyma.

The potential for background suppression and inflow saturation techniques to aid in clinical evaluation of pulmonary perfusion is demonstrated in Figure 3.6. In this pulmonary hypertension (PH) patient, the FAIR perfusion image acquired with 3 signal averages suffered from motion artifacts and reduced SNR (A), possibly due to the patient's difficulty in tolerating the extended

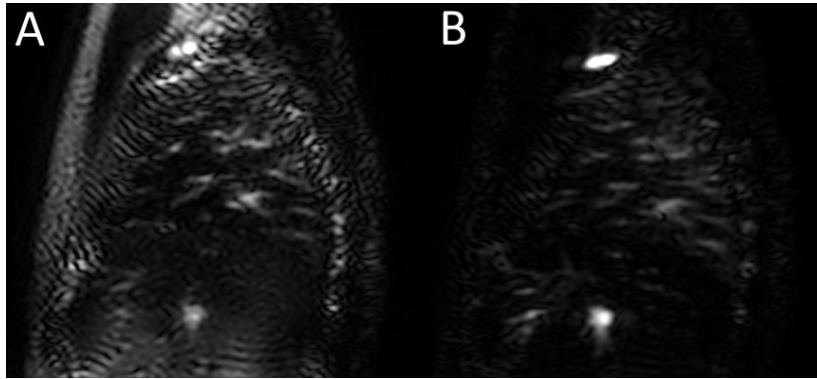


Figure 3.4: Sagittal 2D FAIR control images acquired with HS (A) and C-FOCI (B) background suppression inversion pulses. The background tissue was more completely suppressed with the C-FOCI pulse compared to HS, particularly in regions of fat.

breath hold and reduced perfusion as a result of increased pressure in the pulmonary vasculature. The use of background suppression significantly improved SNR and suppressed motion artifacts, although the perfusion image was still dominated by bright vascular signal that obstructed the view of underlying perfusion (B). By interleaving inflow saturation pulses between the background suppression towards the end of the post-labeling delay, the resulting perfusion image shows true parenchymal perfusion without bright signal in the vessels (C). Background suppression also allowed for the acquisition of additional signal averages with a guided breathing approach (D, E). Although guided breathing will introduce motion between acquisitions and increase the likelihood of introducing motion artifacts, by suppressing the liver signal, images can be produced with no artifacts at the diaphragm with improved SNR. This PH patient also previously received a chest CT, where several dark patches are visible across the lung that are characteristic of more advanced cases of pulmonary hypertension. It is interesting to note that these patches, which are thought to be related to the vasoconstrictive occlusion of smaller pulmonary arteries [81], appear to correlate well with the regions of lower perfusion in the FAIR images (arrows), which were not apparent in the original FAIR perfusion image without background suppression or inflow saturation.

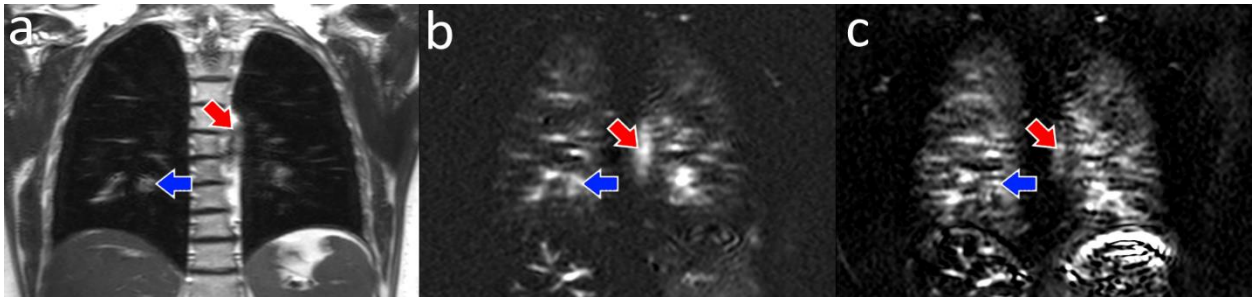


Figure 3.5: Coronal T2-weighted (a), FAIR without (b) and with (c) inflow saturation, showing decreased signal in the major vessels (arrows). FAIR perfusion-weighted images were acquired using 2 signal averages.

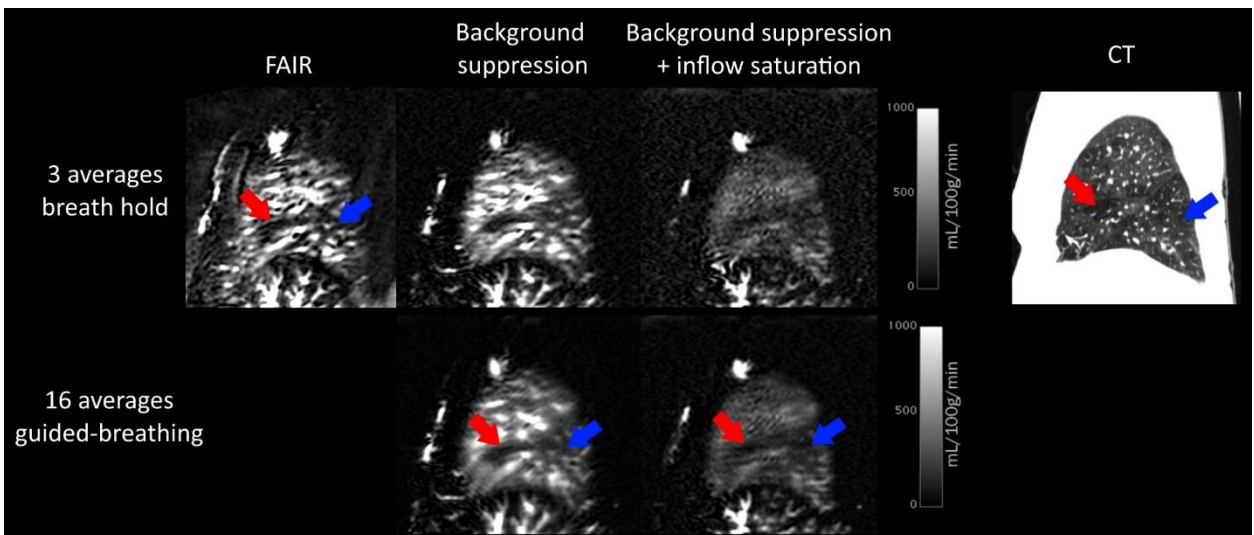


Figure 3.6: Sagittal FAIR perfusion-weighted images in a pulmonary hypertension patient without background suppression, with background suppression, and with background suppression and inflow saturation. Perfusion deficits (arrows) that correlate well with the heterogeneous dark patches across the lung in CT, are visible after suppressing background tissue and bright vascular signal, and are not apparent in the original FAIR image.

3.4 Whole-lung coverage using multi-slice FAIR

The previous FAIR sequence developments to improve SNR and reduce motion artifacts and vascular signal should enable more robust measurement of FAIR perfusion imaging across the lungs. For complete evaluation of whole-lung perfusion, the FAIR sequence was modified to allow

multi-slice perfusion imaging, such that the selective labeling inversion pulses shift along the slice encoding direction with the imaging plane. 5 sagittal slices were acquired to cover the entire right lung with 3 signal averages. Subjects were given breathing instructions in synchronization with the TR of the sequence, and were instructed to breathe in and out during labeling and the post-label delay, and to hold their breath at end-expiration until the image acquisition was completed. The TR was 6s to allow a normal subject breathing rate, the acquisition took 3 minutes to complete, slice thickness = 15mm, and resolution = $3 \times 3 \text{mm}^2$. Background suppression was applied with both the HS and C-FOCI inversion pulses to assess the predicted improvements across the body enabled by the B_0 and B_1 insensitive C-FOCI pulse. To evaluate the effects of inflow saturation on the bright vascular signal across the lung, saturation was applied repeatedly for a duration, τ , which was varied from 0-400ms in 100ms increments to progressively suppress perfusion signal further down the vascular tree (Figure 3.7). The saturation slab was positioned adjacent to the imaging region, covering the heart, to suppress the late-arriving perfusion bolus (Figure 3.8).

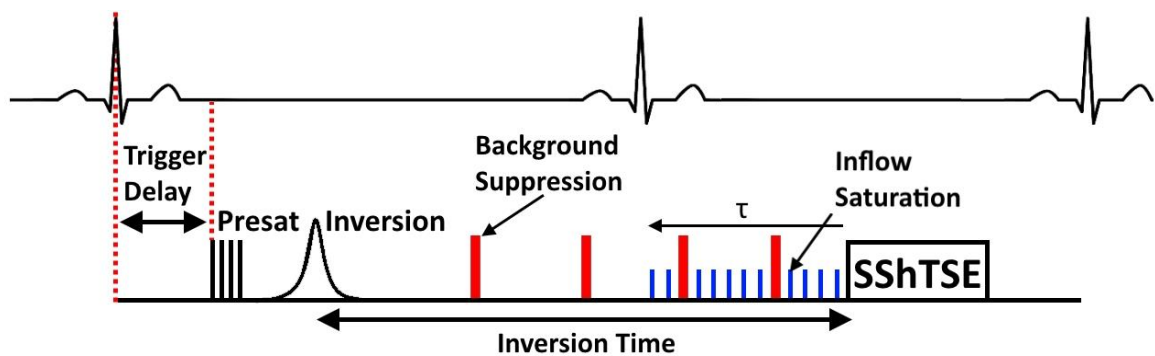


Figure 3.7: ECG-triggered FAIR sequence with background suppression and inflow saturation. The variable inflow saturation duration before the acquisition (τ) saturates inflowing signal that is left in the larger pulmonary vessels at the time of imaging, while inflowing labeled blood before this time can be seen as tissue perfusion.

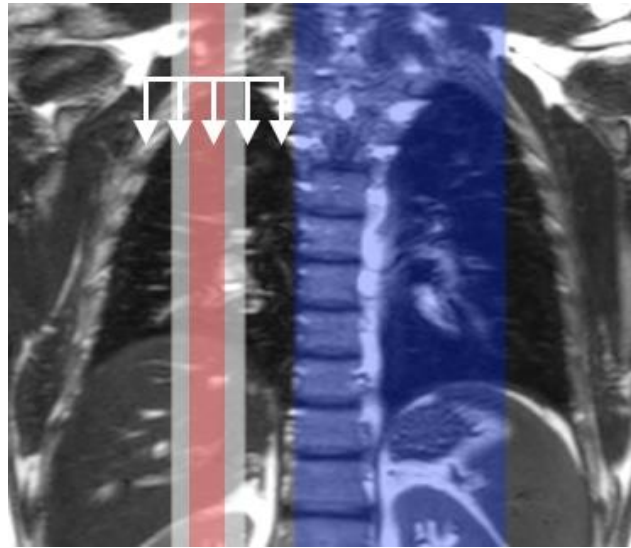


Figure 3.8: (a) Imaging slice (red) with 3x wider selective inversion (white) and inflow saturation pulses covering the heart and pulmonary arteries (blue). Non-selective inversion not shown. The labeling inversion and acquisition shift together across the lungs for full coverage (white arrows)

Figure 3.9 shows the control sequence images across the lung with HS and C-FOCI background suppression pulses, showing more complete suppression in regions of increased off-resonance with C-FOCI, similar to the results achieved in a single 2D slice. Figure 3.10 shows the corresponding subtracted perfusion-weighted images from the same scan with the C-FOCI pulse providing reduced artifacts near fat (colored arrows) and improved SNR, likely due to improved inversion efficiency of the labeled blood, providing an overall increase in the measured ASL signal.

Figure 3.11A shows perfusion-weighted images across the lung with C-FOCI background suppression in a different volunteer with bright vascular signal obstructing the view of the underlying perfusion, especially in the larger vessels near the heart, which are also visible in Figure 3.10. By increasing the inflow saturation duration, τ , the bright vascular signal is reduced progressively starting from the larger vessels down to almost complete saturation of the tissue

perfusion, as saturation pulses are applied earlier in the post-labeling delay (Figure 3.11B). In this subject, the optimal τ was around 300ms, where perfusion in the parenchyma is visible with minimal vascular signal.

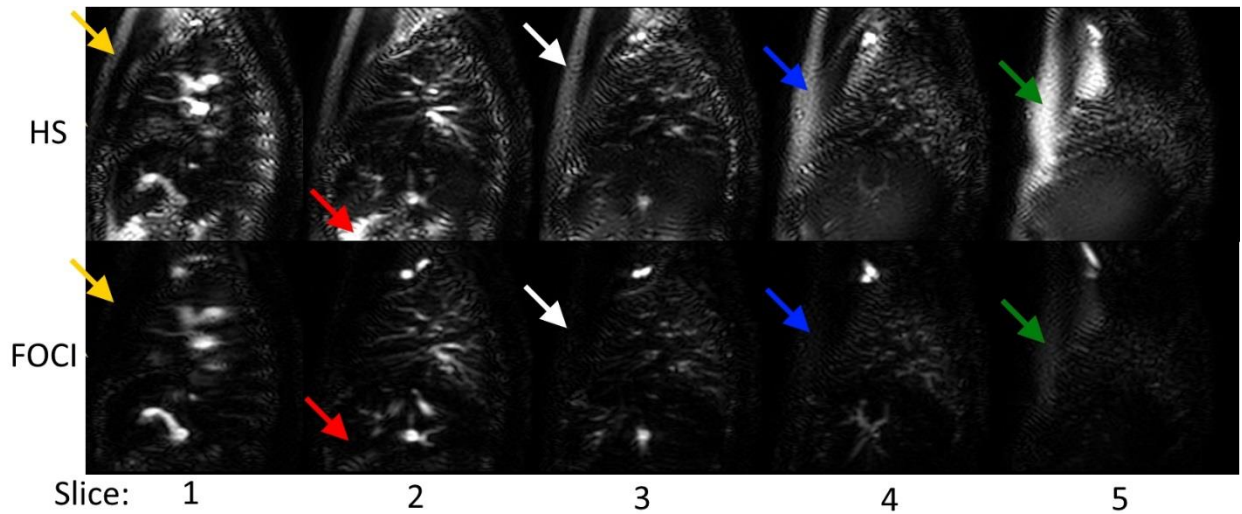


Figure 3.9: ASL control images across the right lung with HS and C-FOCI background suppression pulses. Arrows indicate regions where background tissue was more completely suppressed with C-FOCI compared to HS, mostly in fat tissue where off-resonance is higher.

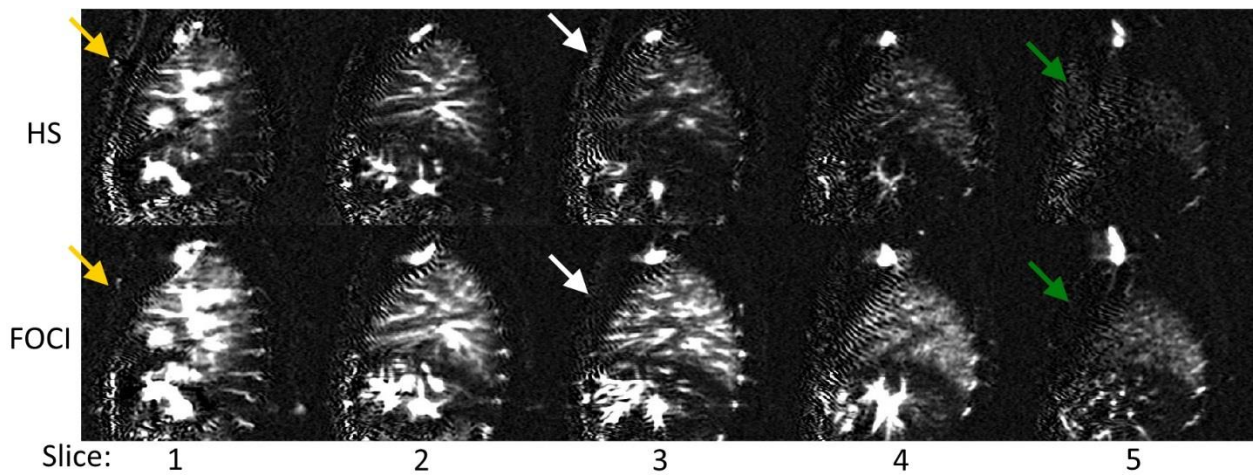


Figure 3.10: Perfusion-weighted images across the right lung from the scan shown in Figure 3.9, with HS and FOCI background suppression pulses. C-FOCI perfusion images show improved SNR compared to HS, and improved suppression in fat tissue (arrows).

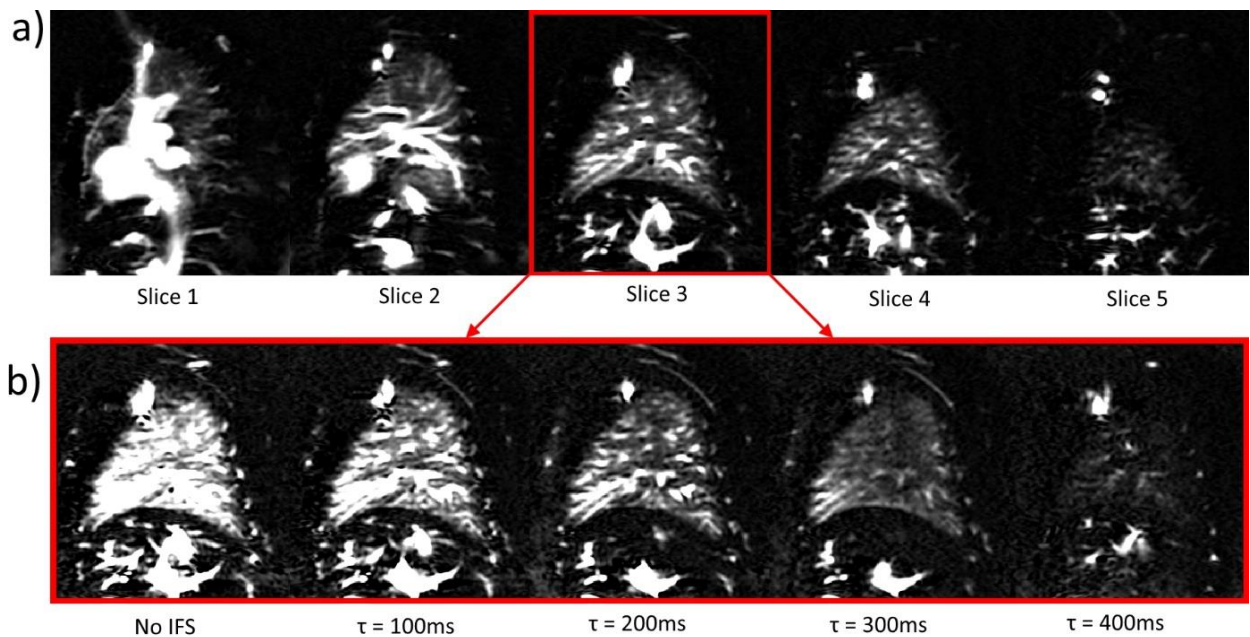


Figure 3.11: (a) Perfusion-weighted images across the lung with C-FOCI background suppression. The center slice was repeated with increasing inflow saturation duration (τ). As τ increases, more of the inflowing label bolus is saturated, reducing the vascular signal until $\tau=300\text{ms}$, where true tissue perfusion can be seen. After this optimal τ for this subject, the tissue perfusion is saturated as well. The window level has been adjusted between (a) and (b) for improved visualization of each slice and the effects of inflow saturation.

3.5 Discussion

We have demonstrated MS-FAIR perfusion imaging across the entire lung, which is essential for the clinical evaluation of heterogenous chronic lung diseases. Background suppression improved the visualization of pulmonary perfusion by reducing noise and respiratory motion artifacts, and will likely be necessary in patient populations who may have difficulty with extended breath holds or following breathing instructions. Although the standard HS background suppression inversion pulse significantly improved perfusion images, it was not adequate for complete fat suppression due to its limited bandwidth. This sensitivity in regions of increased off-resonance is likely to be more of an issue in whole-lung imaging due to the larger FOV.

Improvements in background fat suppression using the C-FOCI pulse that were predicted by Bloch simulations were achieved in vivo due to its decreased sensitivity to B_0 and B_1 inhomogeneities. An added benefit of background suppression is that it enabled prolonged guided-breathing acquisitions for additional signal averages and more complete lung coverage without the introduction of respiratory motion artifacts.

By saturating the inflowing ASL signal that flowed into the imaging plane at the end of the post-labeling delay, the bright vascular signal in the FAIR perfusion images was minimized, allowing for more accurate assessment of the underlying tissue perfusion. Varying the inflow saturation duration prior to the acquisition showed that an optimal perfusion bolus width can be found that suppresses major vessels without diminishing tissue perfusion. The application of these developments in a pulmonary hypertension patient showed their value in detecting perfusion deficits where the standard FAIR sequence was inadequate. While the blood arrival time will vary between different subjects, an average saturation duration could be established as a compromise between vessel saturation and remaining ASL signal, possibly based on heart rate. Future work will include determining an optimized τ in additional normal volunteers. A similar τ to that found in this study may provide sufficient vessel suppression in other subjects, although more data is needed before a standard value can be established. This saturation timing will also need to be optimized for different patient populations with varied arrival times of inflowing blood. Finally, whole-lung perfusion will also be quantified using the modified equation for the fixed-width perfusion bolus [80], and inflow saturation and C-FOCI background suppression will be applied using multi-slice FAIR across both lungs for complete evaluation of pulmonary perfusion.

CHAPTER 4

**ON THE APPLICATION OF PSEUDO-CONTINUOUS ASL FOR PULMONARY
PERFUSION IMAGING***

4.1 Introduction

Pulmonary perfusion imaging using pulsed ASL (e.g. FAIR [42, 60]) has been extensively used in research settings at 1.5T, and more recently at 3T for improved SNR [74]. However, PASL approaches are lower in SNR compared to CASL based methods. CASL has been applied for pulmonary perfusion imaging [50] but in recent years, pCASL [46] has become the standard for non-contrast perfusion imaging due to its comparable SNR and ease of implementation on standard clinical scanners [53]. pCASL has been successfully applied to cerebral and renal perfusion studies by labeling the carotid arteries [53] and abdominal aorta, [35] respectively. The extension of pCASL to study pulmonary perfusion has been non-trivial due to the highly pulsatile blood flow, and the complex anatomy of the lungs posing a significant challenge in identifying the vessel of interest for successful labeling.

The purpose of this exploratory study was to investigate the challenges associated with pulmonary perfusion imaging using pCASL by targeting both the inferior vena cava (IVC) and the right pulmonary artery (RPA) and to evaluate the efficacy of cardiac triggering in minimizing the effects of pulsatile flow in the lungs.

* This work is in preparation for publication submission. Portions of this work were presented at the 24th and 25th annual meetings of the ISMRM in Toronto (May 2015) and Singapore (May 2016).

4.2 Methods

This was a HIPAA-compliant study approved by the institutional review board. All subjects provided written informed consent prior to the participation in the study. 10 healthy volunteers were scanned using axial labeling of the inferior vena cava, 5 of which were scanned after implementation of the cardiac triggered acquisition, and 5 subjects were scanned using sagittal labeling of the right pulmonary artery. All subjects also underwent sagittal FAIR perfusion scans for qualitative comparison.

The pCASL pulse sequence was implemented on a 3T Ingenia scanner (Philips Healthcare, Best, The Netherlands). The sequence began with saturation pulses applied axially to cover the lungs and destroy magnetization build-up from previous repetitions. Cardiac triggering was used to reduce signal variations between acquisitions introduced by pulsatile flow [60, 74]. Two pCASL labeling approaches were evaluated: axial labeling of the IVC and sagittal labeling of the RPA. To improve the SNR of pCASL images, multiple pairs of label/control images were acquired in approximately 3:30 min [35], and a guided breathing approach was used to reduce motion artifacts [35]. Subjects were given breathing instructions in synchronization with the 6 second TR of the pCASL sequence, and were instructed to breathe in and out during the LD/PLD, and to hold their breath at end-expiration until the image acquisition was completed. Other imaging parameters were slice thickness=15mm, TE=46ms, TR=6s. Using similar acquisition parameters, 2D FAIR perfusion images with cardiac triggering were also acquired with an inversion delay equal to one cardiac period [60, 74], which can reliably place the acquisition during diastole. Three signal averages were acquired within an 18-second breathhold. After the PLD, a SSHTSE acquisition was used to minimize susceptibility artifacts due to B_0 inhomogeneities for both labeling approaches.

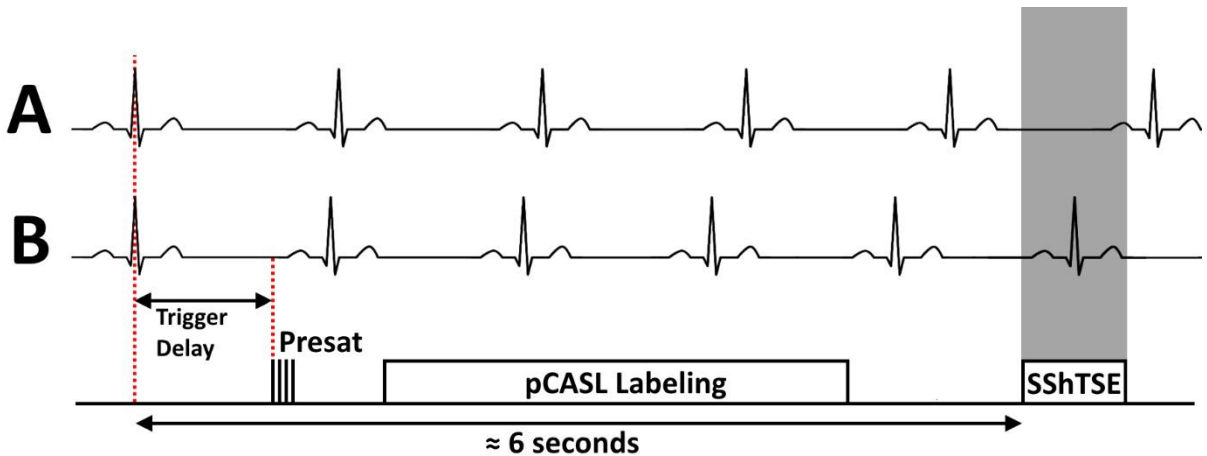


Figure 4.1: (A) Assumed ECG Signal with constant cardiac period with a diastolic acquisition. (B) Example of an ECG signal with slight heart rate variation after triggering the presaturation pulses. This change in timing leads to a systolic acquisition, producing signal variations unrelated to the ASL signal.

4.3 Labeling approach 1: Inferior Vena Cava

Initially, venous blood flowing through the IVC was labeled axially below the diaphragm [82]. With this approach, the labeled blood first passes through the right heart before being delivered to the lungs through the pulmonary arteries. Standard cardiac triggering was used, which triggered the beginning of the sequence to place the SShTSE acquisition during diastole (Figure 4.1 A). This approach allows for the imaging of both lungs simultaneously since the labeled blood mixes in the heart and is delivered to both lungs. However, this will result in reduced effective labeling efficiency since the blood delivered to the lungs is a combination of labeled IVC blood and unlabeled SVC blood. The labeling duration (LD) was 2s to ensure sufficient labeled blood was delivered to the highly-perfused lungs, and the post-labeling delay (PLD) was 1s to allow labeled blood to reach the lungs. Figure 4.2 shows a coronal T2-weighted image (A) with the axial pCASL labeling plane shown in red, and coronal (B) and sagittal (C) pCASL perfusion-weighted

images in two representative subjects, showing promising results with high SNR and good visualization of the pulmonary parenchyma.

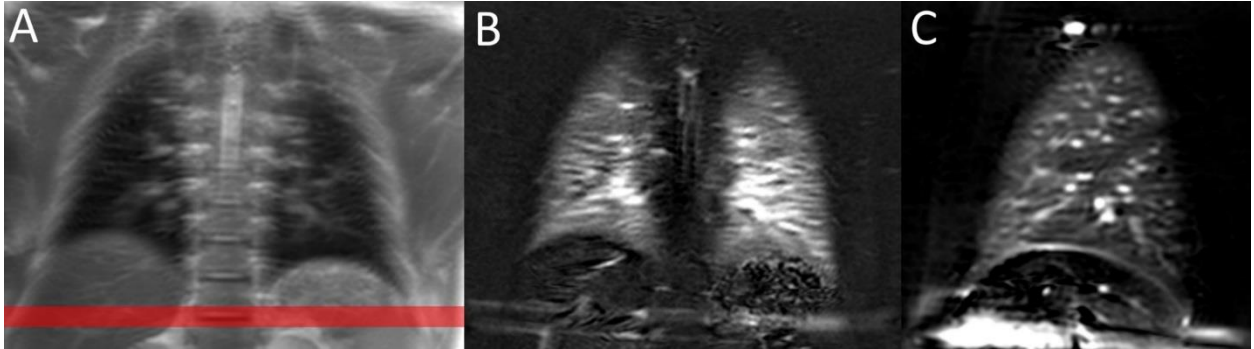


Figure 4.2: Coronal proton density weighted image with labeling plane applied over the IVC in red (A) and the corresponding coronal perfusion-weighted image (B). (C) Shows a sagittal perfusion-weighted image with IVC labeling in another volunteer.

4.3.1 *Influence of cardiac phase*

Despite the use of cardiac triggering at the beginning of the sequence to place the acquisition during diastole, irregular variations in the measured ASL perfusion signal were observed over consecutive, identical acquisitions in many subjects (Figure 4.3). It was discovered that the combination of standard cardiac triggering and extended repetition time of the pCASL sequence (5-6s) rendered the sequence sensitive to slight variations in heart rate. The prolonged delay after cardiac triggering, which is consisted of the Pre-LD, LD, and PLD, led to small changes in heart rate causing significant variability in the cardiac phase of the acquisition (Figure 4.1B). This was verified by comparing scanner log files containing the cardiac phase of the acquisitions with the resulting perfusion-weighted images. Images with higher “perfusion” signal corresponded to the control and label images that had significant differences in the cardiac phase of the

acquisitions, implying that the inconsistencies in these images could likely be attributed to pulsatile flow effects.

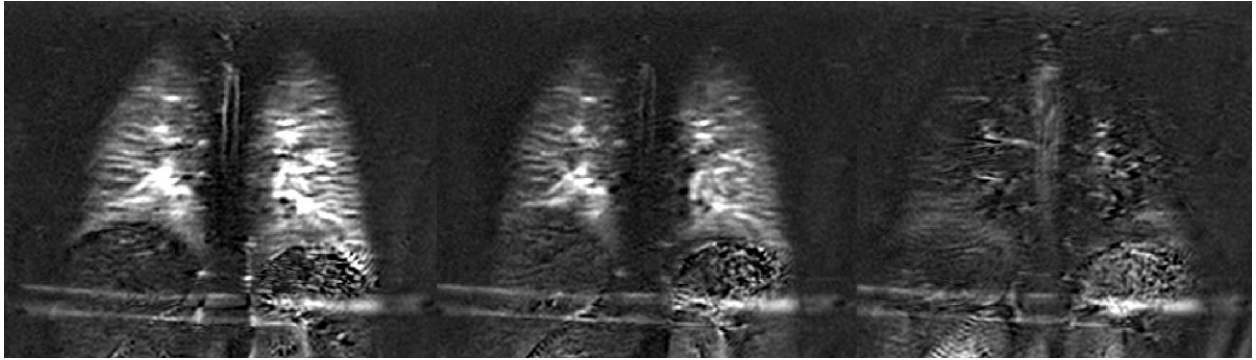


Figure 4.3: pCASL perfusion-weighted images with IVC labeling, showing the substantial inconsistencies experienced between identically-acquired signal averages.

To verify that the observed signal variations could be potentially introduced by cardiac phase effects and not some other inconsistency in the labeling efficiency, cardiac-triggered SShTSE images were acquired without spin labeling at 100ms increments throughout the cardiac cycle in a separate volunteer. Phase contrast velocity measurements were acquired in the RPA to compare flow velocity with SShTSE-measured signal intensity. Figure 4.4 shows the RPA flow velocity (A) and the SShTSE signal intensity (B) in the vessel and lung tissue throughout the cardiac cycle, taken from ROIs in (C). The SShTSE signal intensity exhibited an expected inverse relationship with flow velocity, since moving spins accumulated additional phase during the acquisition, resulting in a signal void. By subtracting images acquired during systole and diastole, at 200ms and 500ms trigger delays, a “perfusion-like” image was produced (D), showing the signal differences that can be induced by pulsatile flow. The flow-dependence of the SShTSE has been previously described, and could result in as much as a 30% reduction in signal [83, 84], far outweighing the small 1-2% signal changes measured by ASL. While these “perfusion-like”

images mimic ASL images and could possibly be used to visualize flow reductions in the lungs, they are weighted by flow velocity, rather than tissue perfusion, and would not provide quantitative perfusion maps. For SSHTSE-based pulmonary perfusion imaging with ASL, acquiring images with consistent cardiac phase is essential [60].

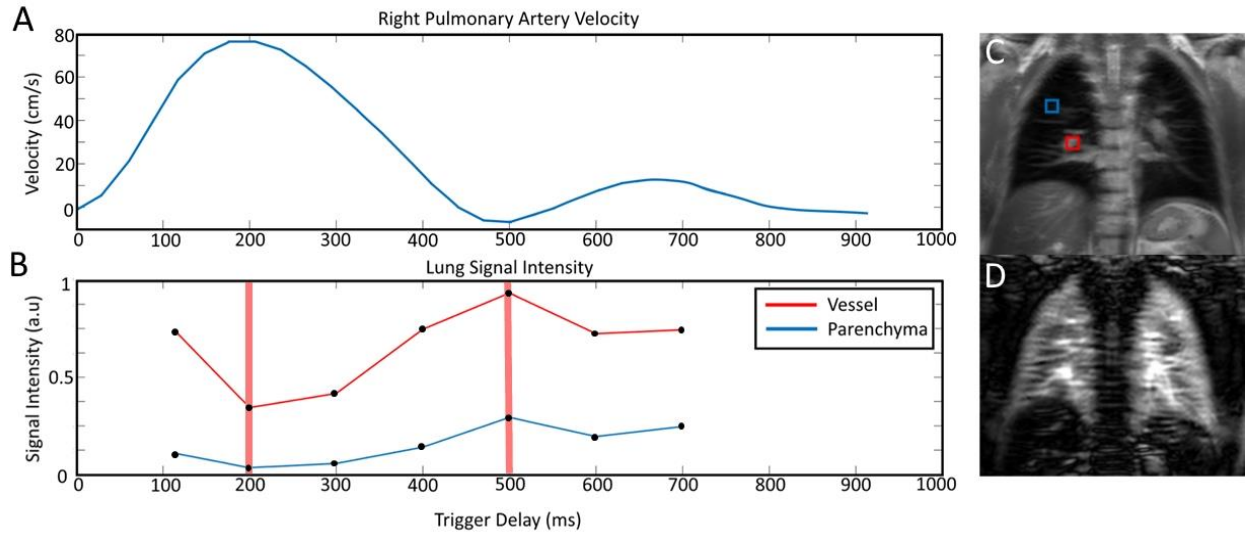


Figure 4.4: (A) Phase-contrast velocity measurement in the RPA throughout the cardiac cycle, and (B) the corresponding signal intensity in vessel and lung tissue ROIs (C, red and blue boxes), showing the inverse relationship between SSHTSE-measured signal intensity and flow velocity. (D) shows the subtraction of images acquired at 500 ms and 200 ms trigger delays, indicated by vertical red lines in (B), demonstrating the significant signal differences that can be introduced by flow in addition to spin labeling to create a “perfusion-like” image.

4.3.2 Cardiac-triggered acquisition

The standard cardiac triggering approach implemented at the beginning of the ASL sequence proved unsuitable for ASL imaging with the prolonged repetition times in the presence of pulsatile flow. To reduce these flow-induced signal variations, the sequence was modified to cardiac trigger the acquisition after a pre-defined post-labeling delay (Figure 4.5) such that, following any changes in heart rate, a diastolic acquisition would still be achieved.

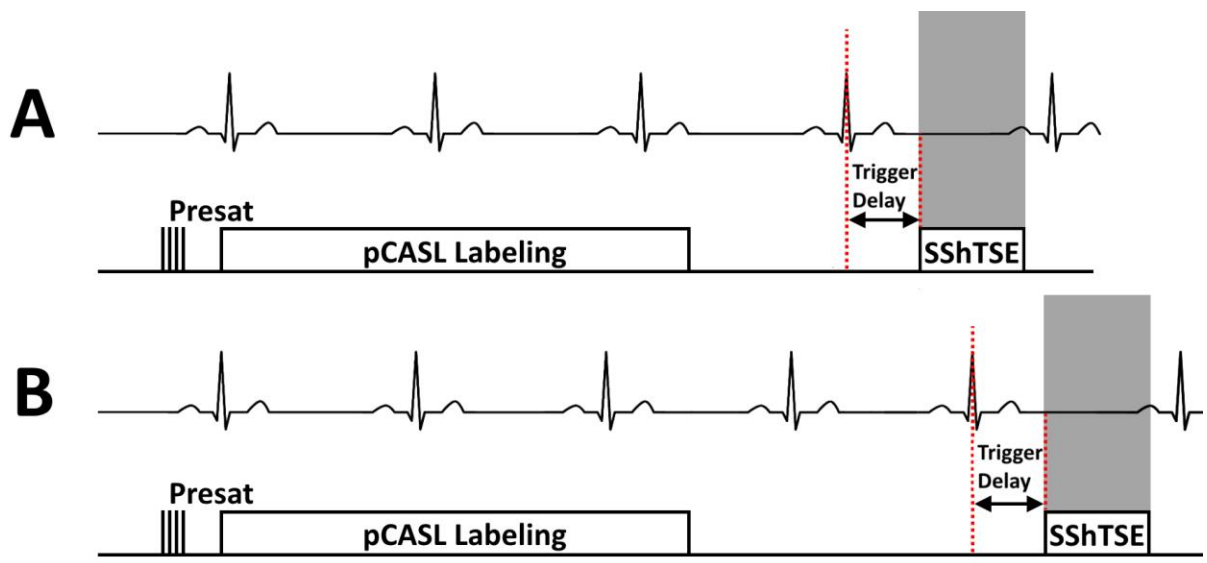


Figure 4.5: pCASL pulse sequence implemented with cardiac triggering of the acquisition, such that data acquisition using SShTSE occurs in the diastolic phase of the cardiac cycle for constant heart rates (A) and varied heart rates (B).

This cardiac triggering approach does introduce some limitations. Varying the PLD according to cardiac phase leads to varied T_1 relaxation of labeled blood between acquisitions, which in turn complicates perfusion quantification, requiring a specialized model to account for the differences [85]. A second disadvantage to this cardiac triggering approach is that background suppression is not compatible with variable PLDs because the exact time between the start of the sequence and the acquisition is unknown. Nevertheless, cardiac triggering after the PLD will ensure consistent cardiac phase of the acquisition, leading to more reproducible perfusion imaging.

After implementing the cardiac triggered acquisition, perfusion-weighted images with IVC labeling were more consistently generated. Figure 4.6 (A-C) shows three repetitions of the pCASL sequence with IVC labeling after the implementation of a cardiac triggered acquisition. By minimizing the variations caused by cardiac phase, the repetitions show a more consistent

perfusion signal. Although the apparent SNR of each repetition was decreased compared to that shown in Figure 4.3, the signal variations are from spin labeling alone, and are proportional to true tissue perfusion, rather than added effects from flow velocity. The perfusion image resulting from the average of the 10 consistent repetitions is shown in Figure 4.6 (D). In this subject, there were substantial motion artifacts below the diaphragm, which could likely be significantly reduced with background suppression. Successful application of background suppression with pCASL IVC labeling is shown in Chapter 5.

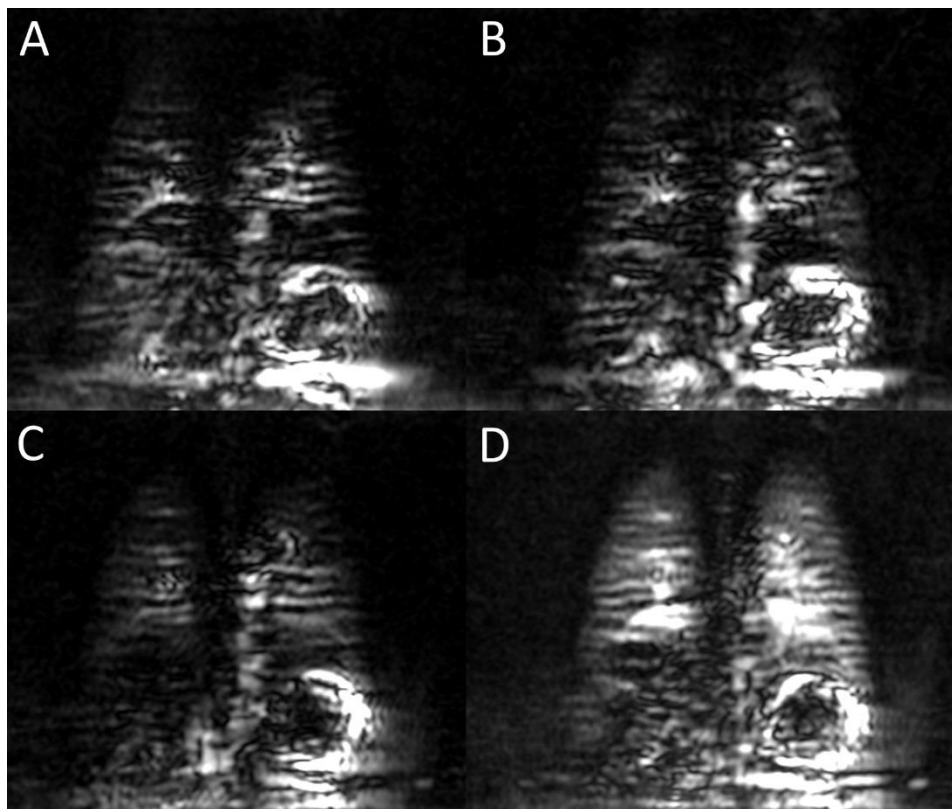


Figure 4.6: (A-C) show multiple repetitions of the pCASL sequence with IVC labeling after the implementation of a cardiac triggered acquisition to minimize the variations in cardiac phase, showing more consistent perfusion signal, and the perfusion image resulting from the average of 10 repetitions (D).

4.4 Labeling approach 2: Right pulmonary artery

To further improve SNR by shortening the transit delay of blood between the labeling plane and the lungs, a sagittal labeling plane was used to invert venous blood flowing directly to the right lung through the RPA. This allows for a shorter PLD, and will therefore increase the ASL signal difference. This shorter path length between labeling and the tissue will also make the arrival time of the perfusion bolus less variable. This approach does, however, limit the target tissue to a single lung due to the sagittal RPA labeling. The right lung was chosen to avoid motion artifacts from heart for simplicity in this preliminary study. We chose to demonstrate the feasibility of the new technique in the right lung due to reduced cardiac motion artifacts. Based on our experience with IVC labeling, a cardiac triggered acquisition was applied to the RPA labeling approach.

Figure 4.7 (A-C) shows multiple repetitions of the pCASL sequence with sagittal labeling of the RPA and cardiac triggered acquisition, again showing consistent perfusion signal across repetitions. The average of 16 repetitions provides a perfusion image with improved SNR compared to IVC labeling (Figure 4.7D). In the same patient, Figure 4.8 shows a qualitative comparison between FAIR (B) and pCASL (C) perfusion-weighted images. RPA labeling provided improved SNR due to the shorter path length of labeled blood, comparable to FAIR perfusion images. Both approaches provided sufficient SNR to distinguish the three separate lobes of the lungs.

4.5 Discussion

In this work, we demonstrated pulmonary perfusion imaging using two pCASL labeling strategies, and evaluated the performance of the standard cardiac triggering approach. Labeling of

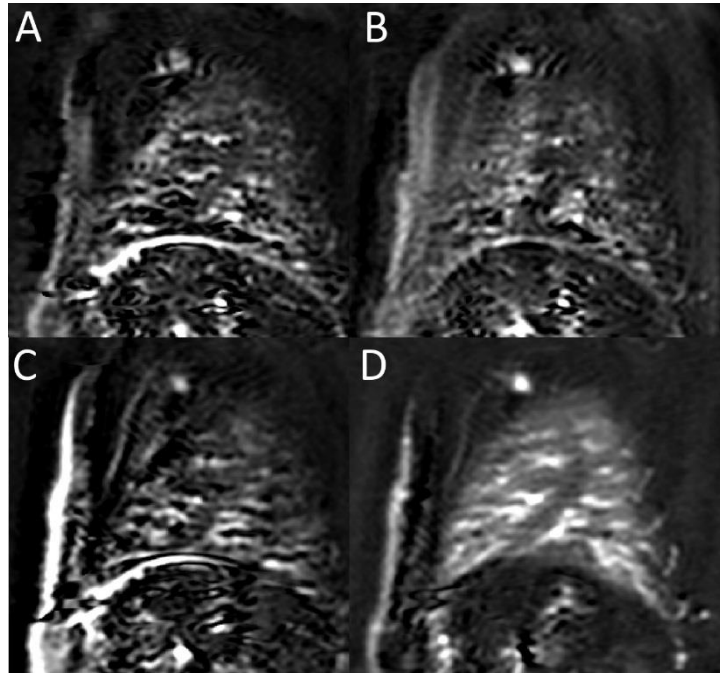


Figure 4.7: (A-C) show multiple repetitions of the pCASL sequence with sagittal labeling of the RPA and cardiac triggered acquisition, showing consistent perfusion signal. The average of 16 repetitions provides a perfusion image with high SNR (D).

the IVC to visualize perfusion in both lungs using the standard cardiac triggering implementation was found to be significantly affected by cardiac phase due to the extended repetition time of the pCASL sequence. This resulted in inconsistent images that were more heavily weighted by flow velocity than perfusion. Although “perfusion-like” images that may also be sensitive to perfusion deficits were acquired, quantifying this perfusion signal would be challenging. This cardiac phase influence is not as pronounced in FAIR perfusion images, since the post-labeling delay is shorter (on the order of 1-2 cardiac periods) and the sequence can be more easily timed to place the acquisition during diastole.

By cardiac triggering the SSHTSE image acquisition, we demonstrated true perfusion-weighted images using pCASL. This approach guaranteed that the signal variations between control and label images are only from spin labeling, and not introduced by cardiac cycle induced

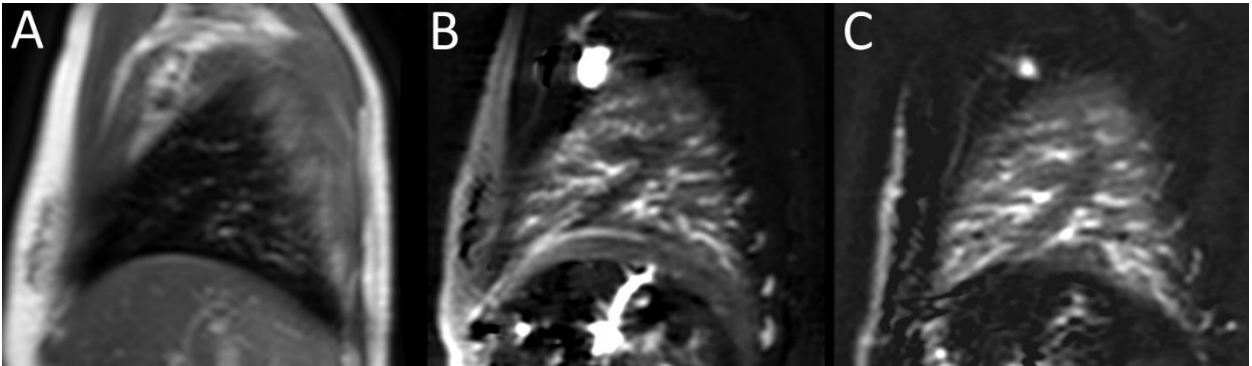


Figure 4.8: (A) Sagittal proton-density weighted image, (B) FAIR perfusion-weighted image, and (C) pCASL perfusion-weighted image using sagittal labeling of the RPA and a cardiac triggered acquisition.

variations. However, this technique posed new challenges with the variable PLD between the control and label acquisitions. Quantification assumes that the PLD between control and label acquisition is the same [31]. Consequently, varying the PLD will introduce errors in quantification due to varied T_1 relaxation between the control and label images, though a technique for accounting for varied PLDs has been proposed [85]. Since perfusion quantification is a key benefit of ASL, this variable PLD approach may not be recommended for most applications, though it did confirm suspicions that cardiac phase was an important factor in making the pCASL sequence more robust. More importantly, variable PLDs prevent the use of background suppression, as the timing between inversion pulses and the acquisition is important to sufficiently suppress a wide range of tissues. Differences in the effectiveness of background suppression between control and label sequences will introduce subtraction errors, and because ASL provides relatively low SNR, reducing physiological noise with background suppression is essential [53].

The shorter transit delay offered by RPA labeling improved image quality considerably compared to IVC labeling. Even though this approach limits the imaging region to a single lung, labeling the pulmonary arteries may be appropriate for most lung imaging applications, since the

shortened path length between the labeling plane and the lungs will result in more predictable blood arrival times across subjects, as well as SNR improvements. While pCASL images with RPA labeling and additional signal averages provided similar image quality as FAIR (Figure 4.8), continuous labeling should theoretically have a significant SNR advantage over pulsed ASL approaches. A likely source of this decrease in the anticipated SNR is the sensitivity of pCASL labeling efficiency to pulsatile flow B_0 inhomogeneities, which are present at the air-tissue interfaces in the lungs and probably affect labeling in the RPA. Approaches to make pCASL B_0 insensitive have been proposed [86, 87], and would likely make RPA-labeled pCASL for lung perfusion imaging more robust in the future.

In conclusion, we have demonstrated the initial feasibility of pulmonary perfusion imaging using pCASL. Our experience with continuous labeling in the lungs has been encouraging, but the labeling and cardiac triggering strategies require further optimization. Our study has influenced the development and optimization of pCASL labeling in the lungs in other groups as well [88-90]. In the future, background suppression pulses could be applied according to the timings derived for the unconstrained CASL sequence [78], allowing background suppression to be interleaved with pCASL labeling. This would result in a significantly shorter delay between cardiac triggering and the acquisition, similar to FAIR [74], allowing diastolic acquisitions to be consistently achieved. Extending this technique to a 3D acquisition using the CASPR view ordering, described later in Chapter 6, should also improve the SNR of perfusion-weighted images. While important advances were made in this pCASL approach, and comparable images were achieved to the established FAIR technique, this study included only qualitative evaluation of image quality. After the sequence is made more robust to sources of labeling inefficiency, a more complete analysis of the

achieved SNR should be conducted. Finally, the reproducibility and accuracy of quantified perfusion should be evaluated in a larger cohort of normal subjects, as well as in patients with chronic lung diseases resulting in disrupted pulmonary perfusion.

CHAPTER 5

**ASSESSMENT OF CAVAL BLOOD FLOW DISTRIBUTION IN FONTAN
CIRCULATION USING ARTERIAL SPIN LABELED MEASUREMENT OF
PULMONARY PERFUSION***

5.1 Introduction

The Fontan procedure is performed in pediatric patients with various congenital heart defects that result in the development of a univentricular heart. This procedure directs venous blood from the superior and inferior venae cavae (SVC/IVC) to the left and right pulmonary arteries (LPA/RPA), bypassing the right heart, so that venous blood can reach the lungs to be oxygenated. While this procedure is necessary for the survival of these patients, the direct connection of the SVC and IVC to the pulmonary arteries can lead to unequal distribution of venous flow towards the lungs, particularly when the vena cavae are offset. Figure 5.1 illustrates normal cardiopulmonary circulation (A) compared with circulation in tricuspid atresia, a congenital heart defect which lacks a right atrioventricular connection due to a missing tricuspid valve (B), which leads to an underdeveloped (hypoplastic) or absent right ventricle. To restore systemic venous flow to the pulmonary circulation, the Fontan operation connects the vena cava to the pulmonary arteries, bypassing the hypoplastic right heart (C). In the past, the IVC and SVC were deliberately offset to minimize hemodynamic energy losses [91], since the systemic and pulmonary circulation are driven by a single ventricle. However, in recent years, the uneven

* Portions of this work was presented at the 21st annual meeting of the Society for Cardiovascular Magnetic Resonance (SCMR) in Barcelona (January 2018) and at the 27th annual meeting of the ISMRM in Paris (June 2018). This work is being prepared for publication submission.

distribution of flow from the IVC has been shown to play a role in the development of pulmonary arteriovenous malformations (AVMs) due to the exclusion of hepatic flow from the affected lungs [92-94]. While the underlying hepatic factor responsible for suppressing AVM development remains unknown, its presence is supported by Fontan revision surgeries that redistribute venous IVC flow equally between the lungs resulting in the regression of pulmonary AVMs [95, 96]. There have also been reports of abnormal pulmonary perfusion in patients with Fontan circulation using radionuclide imaging [93, 97] due to the decrease in pulsatile flow [98], since there is no ventricular contraction pumping blood into the pulmonary circulation.

To evaluate risk for AVM development, the preferential flow of hepatic blood can be measured using selective angiography, requiring the invasive injection of contrast into the IVC via catheterization [92]. 4D-flow MRI has also been demonstrated as a non-invasive approach to measuring IVC flow direction using particle trace simulations [99, 100]. However, 4D-flow requires long scan times and extensive post-processing, and does not provide pulmonary perfusion maps. These various imaging techniques can help answer important clinical questions about caval flow direction and pulmonary perfusion, but a non-invasive, non-ionizing approach would be beneficial for repeated evaluation in these pediatric patients. Therefore, the purpose of this study was to investigate the use of the previously demonstrated ASL techniques, FAIR and pCASL, to quantify lung perfusion and assess the origin of pulmonary blood in Fontan patients, and compare the IVC flow measurements with 4D-flow MRI.

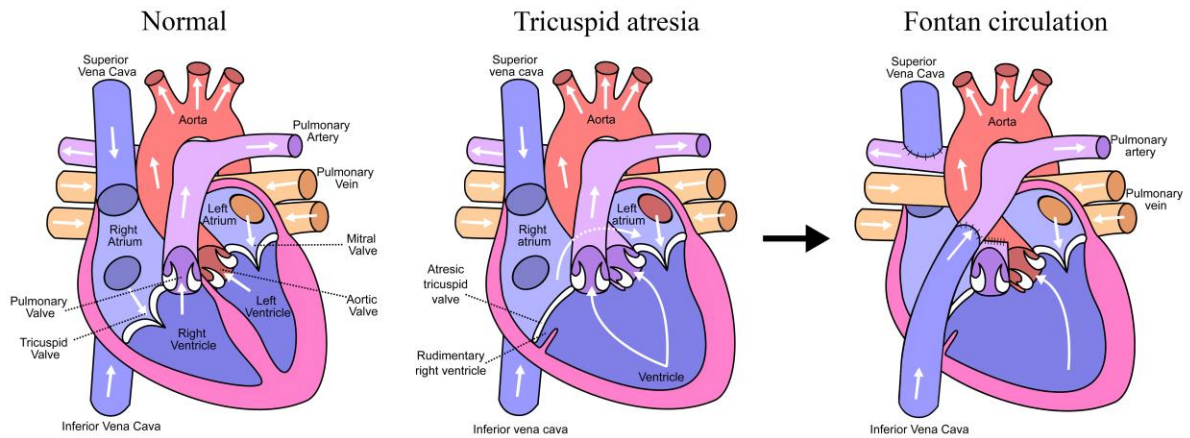


Figure 5.1: Cardiopulmonary circulation in a normal heart, a congenital heart defect resulting in a missing tricuspid valve (tricuspid atresia), and the result of the Fontan operation to restore venous flow to the pulmonary circulation. Figure adapted from [101].

5.2 Methods

24 patients with Fontan circulation (age 15.2 ± 2.4 years, 15 male) were scanned on a 1.5T Philips Ingenia scanner (Philips Healthcare, Best, The Netherlands) between December 2016 and July 2017, with IRB approval and informed assent from their guardians.

5.2.1 ASL-MRI

The FAIR technique, described in Chapter 2, was used to measure pulmonary perfusion in a coronal 2D slice through the lungs, providing a non-ionizing alternative to radionuclide imaging. The FAIR perfusion signal is generated from the inflowing inverted blood from outside of the imaging plane (Figure 2.1). It can therefore provide a measure of total perfusion to the imaging slice, and does not discriminate based on the source of inflowing labeled blood.

pCASL uses a prescribed labeling plane to invert blood flowing perpendicularly through a vessel of interest, resulting in a perfusion image containing only blood originating from that

labeled vessel. By labeling the IVC, the resulting images will be weighted only by blood flow originating from the IVC, allowing for the contribution of hepatic venous flow to each lung to be calculated. Although this IVC labeling approach resulted in significant flow artifacts related to cardiac phase in normal cardiopulmonary circulation (Figure 4.3, Figure 4.4), venous flow to the lungs in Fontan circulation is passive and much less pulsatile. Analysis of the signal measured during systole and diastole in the first patient in this study (similar to Figure 4.4) confirmed the expected reduction in flow artifacts. Therefore, cardiac triggering was not used in this study to enable the use of background suppression.

The FAIR images were acquired with 3 signal averages in a breathhold. Since the pCASL-labeled blood signal in the lungs is diluted by unlabeled blood contribution from the SVC, 16 signal averages were acquired using a guided breathing approach to ensure sufficient SNR in a clinically acceptable scan time (3:30 min). Both labeling approaches used a coronal 2D-SShTSE acquisition to minimize effects of B_0 inhomogeneities in the lungs, and background suppression to improve SNR and reduce motion artifacts.

To quantify perfusion, a reference (M_0) image was acquired for each view ordering to measure the fully-relaxed magnetization of the blood. These images were acquired during a breathhold with identical timings and acquisitions to the ASL imaging sequences without labeling or background suppression applied. The proton density of blood was measured from the average value of an ROI drawn over the descending aorta [74]. Perfusion quantification for FAIR and pCASL was performed using the standard model for pulsed and continuous ASL, respectively [31]. Reported perfusion values were taken from the mean value from an ROI drawn around each lung. The bright vascular signal was removed using an automated masking approach based on a

threshold derived from the histogram of each lung [42]. The perfusion distribution in each lung was fitted to a lognormal distribution, and the threshold was taken as the distribution mean + 0.25*standard deviation to adapt the cutoff to each subject and to minimize the contribution of larger pulmonary vessels to the tissue perfusion measurement. IVC contribution to each lung based on ASL was calculated as the ratio between the ROIs drawn over the left and right lungs in pCASL images.

5.2.2 4D-Flow MRI

Caval flow direction can be measured using 4D-flow MRI, which is used to acquire volumetric velocity maps throughout the cardiac cycle. This technique acquires phase contrast velocity measurements in 3 dimensions, as well as over time. From these 4D velocity vectors, particle traces can be generated to simulate the flow from each voxel in the vasculature over time. These traces have been demonstrated in the quantification of differential flow in a phantom mimicking Fontan anatomy [102] and in Fontan patients [100, 103].

In each patient, a sagittal 4D-flow acquisition was performed over the heart and junction of the vena cavae with the pulmonary arteries. Images were acquired over 10-15 minutes, with velocity encoding of 150cm/s and ECG triggering to acquire images over 24 heart phases. Data was processed using *GFlow* (*GyroTools, Zurich, Switzerland*). Linear phase correction was performed before analysis to correct offsets introduced by eddy currents. Caval flow distribution was visualized by generating particle traces towards the pulmonary arteries from an ROI drawn in the vena cavae. Particles that reached ROI's drawn around the LPA and RPA originating from the IVC were counted to quantify the hepatic flow reaching each lung. The density of emitted particles was consistent across all subjects.

5.3 Results

Five patients were excluded from the results due to susceptibility artifacts in the 4D-flow images caused by metal stents, embolization coils, or fenestration closure devices, which prevented differential flow analysis. Four additional patients were excluded due to low SNR in pCASL images, likely due to low labeling efficiency or extended transit delays from the labeling plane to the lungs.

Figure 5.2 shows FAIR and pCASL lung perfusion images in three representative subjects. FAIR images measure total perfusion to the imaging slice, while pCASL allows for the visualization of pulmonary blood flow originating from the IVC, and showed good visual agreement with 4D-flow path lines generated from the IVC (blue path lines).

Figure 5.3 shows perfusion-weighted images in another patient acquired with FAIR (A), pCASL (B), and their corresponding quantified perfusion images (C, D). Mean total lung perfusion measured with FAIR across all subjects was 469 ± 198 mL/100g/min, within the accepted normal range [60]. Quantified pCASL perfusion values were expectedly lower than FAIR values, since only the fraction of perfusion originating from the IVC contributes to the final ASL signal in the lungs. This difference in absolute perfusion to each lung from FAIR and pCASL images could theoretically be used to infer the SVC contribution to each lung as well, though this flow distribution is not as important as the hepatic flow in gauging patient outcomes.

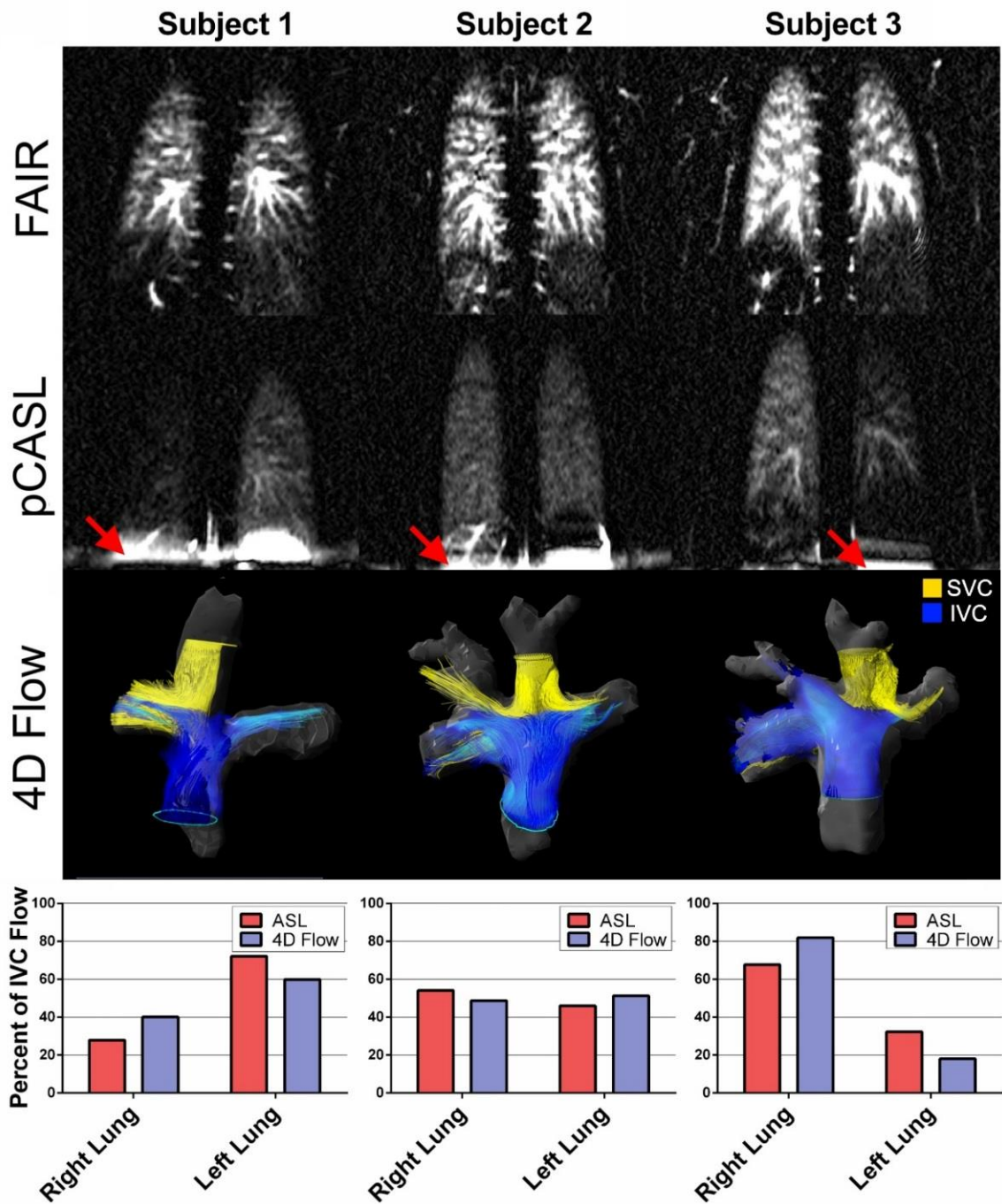


Figure 5.2: Coronal lung perfusion images from representative subjects acquired using FAIR (total perfusion) and pCASL (IVC contribution only), and 4D-flow pathlines from the SVC and IVC. The graphs show the calculated percentages of IVC flow to the left and right lungs, which are visually in agreement with the ASL and 4D-flow results for each subject. An artifact caused by pCASL labeling can be seen below the diaphragm (red arrows).

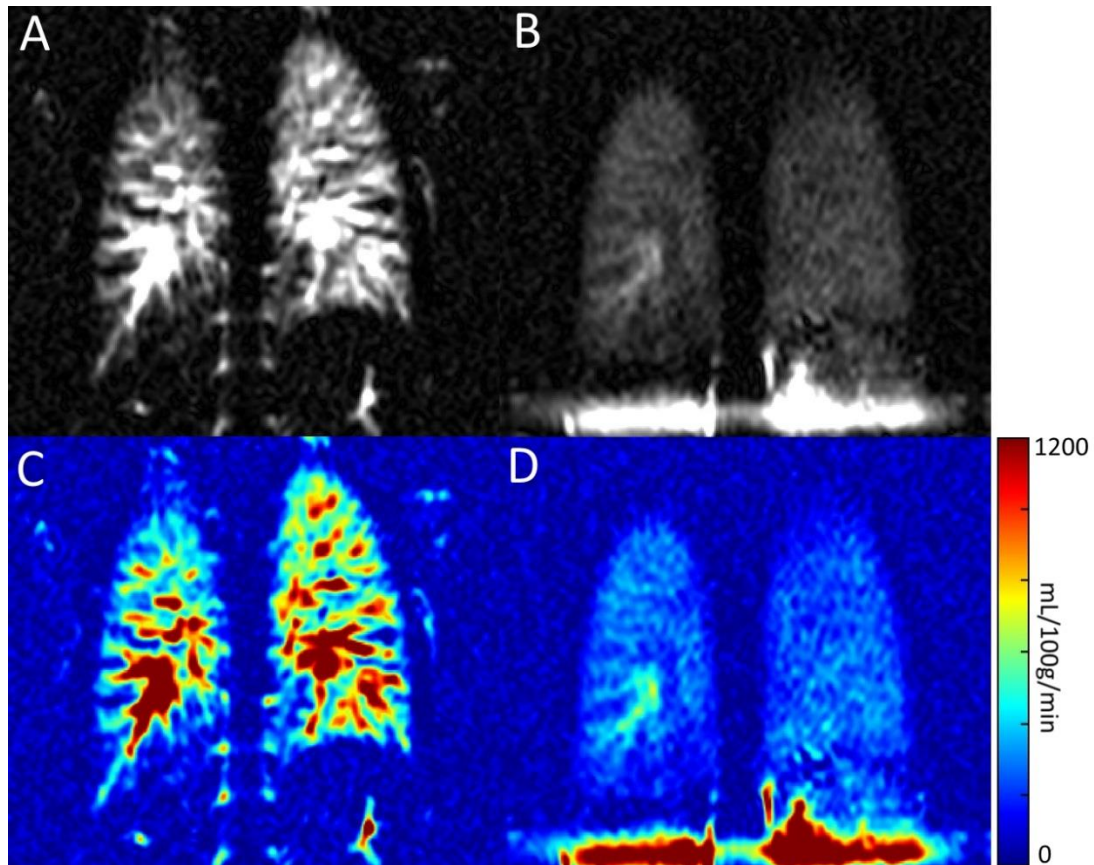


Figure 5.3: Quantified Perfusion with (A) FAIR and (B) pCASL. Quantified FAIR perfusion is in the expected range for normal lungs. pCASL shows reduced perfusion because the perfusion signal is diluted by unlabeled SVC blood flow.

Figure 5.4 shows analysis of agreement between the 4D-flow and ASL measurements of preferential IVC flow towards the right lung. The two measurement approaches showed good agreement with a Pearson correlation coefficient of 0.72 ($p < 0.01$). Bland-Altman analysis (B) shows a relatively low bias of 4.39% between the two techniques. The average measured preferential flow to the right lung was 52% with ASL and 56% with 4D-flow. However, in individual patients, the percent of IVC flow through the RPA ranged from 28-71% with ASL and 36-78% with 4D-flow, indicating that the preferential flow in these subjects can be quite extreme.

The outliers on the either end of these distributions are the patients who may be expected to have increased risk for AVM development.

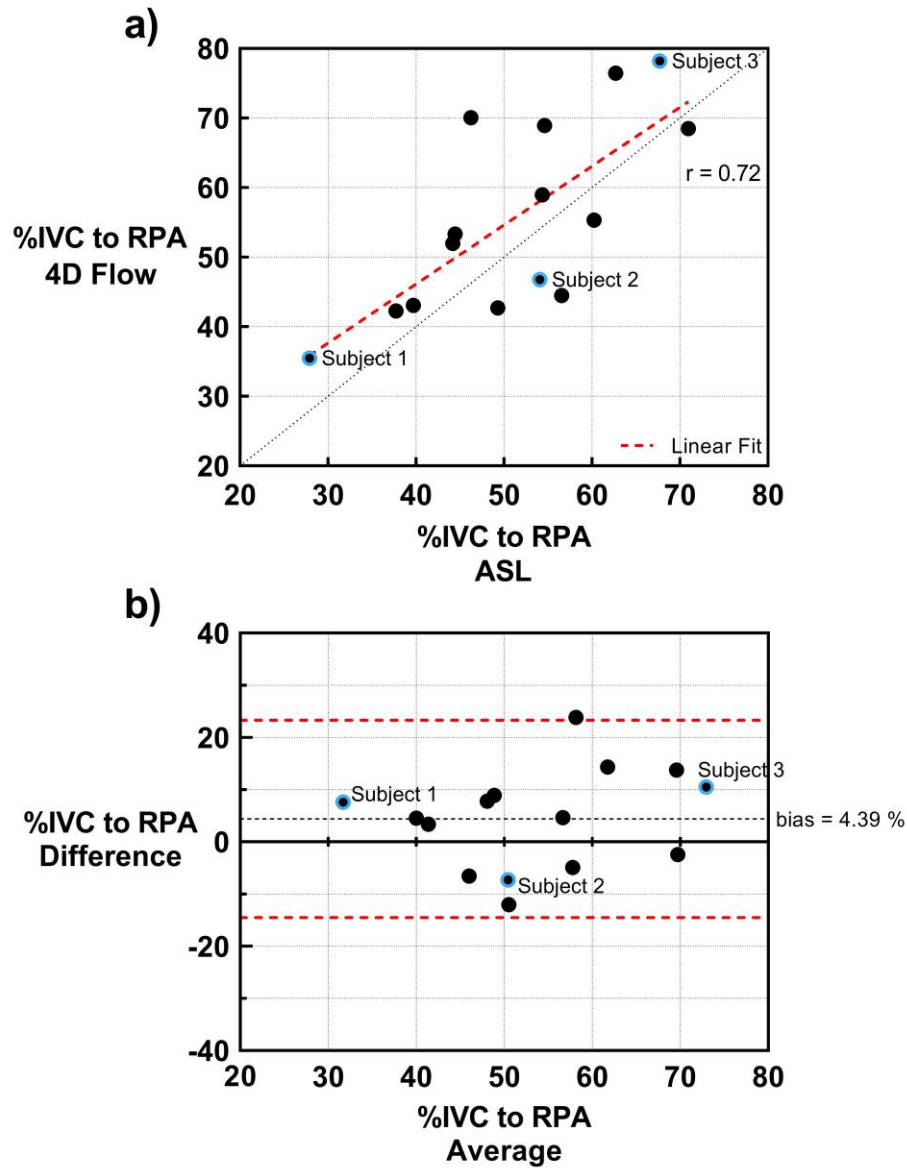


Figure 5.4: Percentage of IVC flow to the right lung: (a) showing good agreement between ASL and 4D-Flow measurements. Subjects shown in Figure 5.2 are indicated by the blue data points. (b) Bland-Altman analysis of pCASL and 4D Flow measurements, showing a bias of 4.39%, with 95% confidence intervals shown in red.

5.4 Discussion

We have demonstrated simultaneous measurement of pulmonary perfusion and differential flow from the IVC in Fontan patient populations using arterial spin labeling. pCASL allows contrast to be precisely generated in the IVC, allowing for the immediate evaluation of differential pulmonary blood flow. This was previously not possible with scintigraphy or other contrast-based techniques due to the injection site limitations [104]. Although this IVC labeling approach resulted in significant flow artifacts related to cardiac phase in normal circulation (Figure 4.3, Figure 4.4), venous flow to the lungs in Fontan circulation is passive and less pulsatile. This allowed for consistent acquisitions throughout the cardiac cycle without ECG triggering, enabling the use of background suppression. The shorter path length from the IVC to the lungs also indicated that IVC labeling in these patients may provide more robust perfusion measurements than in normal subjects. This spin-labeling approach also provides both pulmonary perfusion and IVC flow measurements in a shorter scan time (3:30 and two breathholds) than the 4D-flow acquisition (10-15 minutes). Post-processing with ASL is simpler, and only requires an ROI to be drawn over each lung. This processing could potentially be done online at the scanner, compared to the time-consuming processing required for 4D-flow path line analysis.

The differential IVC flow measurements showed good agreement with the established non-invasive 4D-flow technique, though this agreement could be improved, particularly in a few cases where the preferential flow was measured to be in opposing directions. There are several possible factors that could introduce this error into flow estimations. Background phase errors can introduce quantification error into the 4D-flow simulations [105], and metal susceptibility artifacts can cause errors in flow path lines, some of which were severe enough to exclude subjects from the analysis.

The 2D ASL acquisition also only samples the IVC-labeled signal in the chosen imaging plane. While this should provide a good approximation of the IVC flow distribution, a 3D acquisition could improve the differential flow measurements by measuring the total labeled blood that is delivered to the lungs. The addition of cardiac triggering may also improve ASL measurements in future studies. Although we did not observe signal variations related to cardiac phase in this patient cohort, they have been reported in the past [106], and likely had some influence on the differential flow measurements.

Nine subjects had to be excluded due to failure of the 4D-flow acquisition or pCASL labeling. Failure to completely invert blood flowing through the IVC could possibly be attributed to low flow velocity or B_0 inhomogeneities, which decrease pCASL labeling efficiency [86]. The 4D-flow acquisition may be optimized for use around metallic implants, though it may not be feasible in patients with metal implants near the caval junction.

As described in previous chapters, ASL images also showed bright signal in the larger pulmonary vasculature, especially in FAIR images, since the FAIR signal bolus contains all inflowing labeled blood, some of which will sit in the vasculature at the time of imaging. This was not observed in most pCASL perfusion images because the labeled bolus of blood has a fixed duration (LD) and flowed beyond the major vessels at the time of imaging. Though the FAIR images were not used in the calculation of differential IVC flow, the application of inflow saturation could improve the appearance of FAIR-measured perfusion, and eliminate the need for masking during post-processing.

It has been previously reported that the IVC preferentially flows towards the left lung in Fontan patients [100, 107]. We observed a slight preference in IVC flow towards the right in this

study (55% average flow towards the RPA), though a larger number of patients is required to understand the flow trends in these patients. Regardless, the flow direction will largely depend on the patient-specific surgical planning [108], and the flow distribution measured in individual patients is more important in making clinical decisions.

Further studies with cardiac triggering, 3D acquisitions, and reduced sensitivity of pCASL to B_0 inhomogeneities [86] may improve the agreement between 4D-flow and ASL measurements of differential IVC flow in the future. The reduction of bright pulmonary vessels during acquisition using inflow saturation pulses [69] will also further simplify ASL post-processing. A non-contrast approach to estimate IVC flow direction was demonstrated in a limited number of sedated patients immediately after Fontan completion [107]. Our current proposed combination of ASL techniques allows not only the measurement of preferential IVC flow, but also quantification of pulmonary perfusion.

In conclusion, ASL can be used to simultaneously assess pulmonary perfusion and differential flow from the IVC. This technique can be applied with no additional risk to pediatric patients, providing a repeatable cardiopulmonary MR examination without the need for catheterization or contrast-based scans.

CHAPTER 6

ROBUST 3D PCASL PERFUSION IMAGING USING A CARTESIAN ACQUISITION WITH SPIRAL PROFILE ORDERING (CASPR)*

6.1 Introduction

ASL perfusion images are generally acquired using multiple signal averages to account for the low SNR and random signal variations introduced by physiological noise. Spiral acquisitions can overcome these challenges by repeatedly sampling the center of k-space, averaging out signal variations throughout the acquisition. As a result, spiral acquisitions were recommended in a consensus paper by the ISMRM's ASL expert panel [53] for 3D brain imaging. However, there are several challenges in extending spiral acquisitions outside of the brain, particularly in body imaging with larger fields of view and areas of increased B_0 inhomogeneities. Since spiral acquisitions use both in-plane gradients simultaneously, field inhomogeneities can induce additional phase in all directions, causing blurring and distortion. Image reconstruction is also complicated by spiral trajectories, since the acquired data must be mapped onto a Cartesian grid before performing the discrete Fourier transform.

In this study, we introduce a 3D segmented TSE acquisition using Cartesian Acquisition with Spiral PRofile Ordering (CASPR) to improve the stability and robustness of ASL measurements [109, 110]. The acquisition was evaluated for both brain and kidney perfusion imaging where labeling strategies have been well established. Perfusion images were qualitatively

* This work has been submitted for publication. Portions of this work were presented at the 26th annual meeting of the ISMRM in Honolulu (April 2016) and at the 55th annual meeting of the American Society of Neuroradiology (ASNR) in Long Beach (April 2017).

and quantitatively compared with frequently used acquisition schemes for perfusion imaging with pCASL for the brain and kidney applications.

6.2 Methods

6.2.1 3D Cartesian Acquisition with Spiral PRofile Ordering (CASPR)

The CASPR view ordering (Figure 6.1C) [109, 110], begins each repetition by sampling the center of k-space, and follows a pseudo-spiral trajectory towards the edge of k-space. By maintaining a Cartesian sampling scheme on a k_y - k_z grid, reconstruction can be performed using the standard Fourier transform without the need for remapping data to a Cartesian grid. Repeated sampling of the center of k-space at the start of each echo train improves the stability of the acquisition to motion. It also results in a shorter effective echo time, maximizing the measured ASL signal. By increasing this measured signal, prolonged echo trains can be achieved to shorten the scan time. The spiral trajectory also allows the center of k-space to be more heavily sampled earlier in each echo train compared to radial ordering schemes [34, 111].

6.2.2 MR Imaging

This study was approved by the institutional review board. Written consent was provided prior to subject participation in the study. Brain perfusion imaging was performed on 6 healthy volunteers, and kidney perfusion imaging was performed on 5 healthy volunteers. Imaging was performed on a 3T Philips Ingenia scanner (Philips Healthcare, Best, The Netherlands). Subjects were placed in the supine, head-first position. An anterior torso coil and respiratory bellows were used in kidney imaging. In the brain, the proposed CASPR acquisition was compared to a 3D

linear-ordered TSE and a multi-slice 3D gradient echo EPI, which is commonly used for brain perfusion imaging [53]. In the kidneys, the performance of 3D CASPR was evaluated against the 3D linear-ordered TSE and the 2D SShTSE, which has been established for renal perfusion imaging [35].

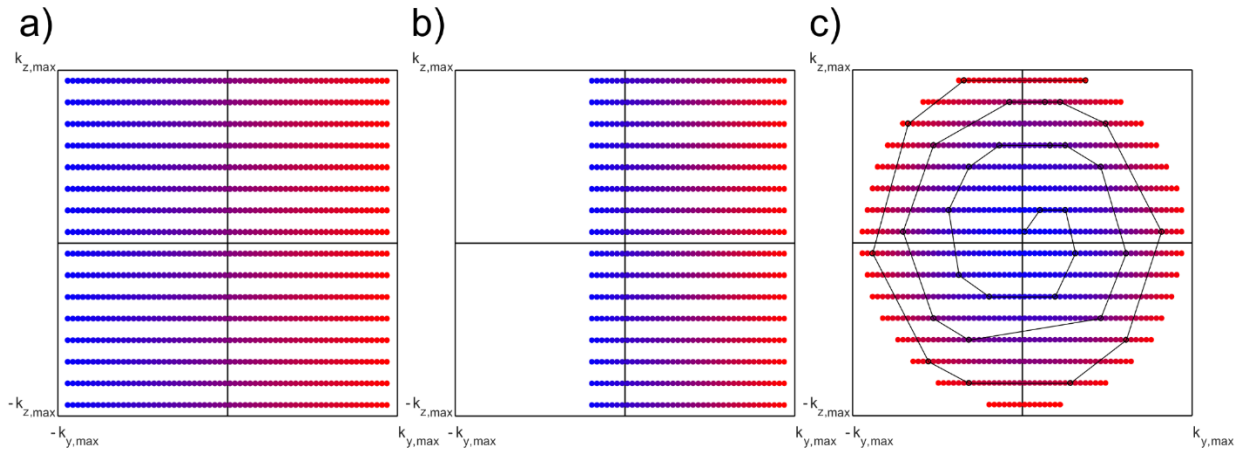


Figure 6.1: Sampling patterns of a 3D TSE acquisition using linear (a), linear with half-scan (b) and CASPR (c) view ordering shown in k_y - k_z plane, where each point represents an echo. The echoes sampled at the beginning of the echo train are shown in blue and transition to red at the end of each echo train. The CASPR acquisition traverses out in a spiral trajectory but maintains sampling on a Cartesian grid.

6.2.3 Quantification

To quantify perfusion, reference (M_0) images were acquired using each of the compared acquisition schemes to measure the fully-relaxed magnetization of the blood. These images were acquired with identical timings and acquisition parameters to the ASL imaging sequences without labeling, background suppression, or inflow saturation. Perfusion quantification was performed using the standard model for continuous ASL [31].

6.2.4 *Image Reconstruction*

Image reconstruction was implemented in MATLAB (The Mathworks, Natick, MA). The control and label images were subtracted in k-space, followed by Fourier transformation and homodyne reconstruction [112] to generate the perfusion difference images. The 2D images acquired with SShTSE partial k-space acquisitions followed the same reconstruction pipeline. Homodyne reconstruction [112] was used to fill the partial k-space .

6.2.5 *Statistical Analysis*

Perfusion homogeneity was assessed by the coefficient of variance, or relative dispersion (RD), providing a measure of the level of noise and other random signal variations. RD was calculated in several gray matter ROIs (upper frontal lobe, upper parietal lobe, parietal operculum, thalamus, occipital lobe, cerebellum, and brainstem) in 2D EPI and 3D CASPR images. The agreement between quantified mean perfusion values was evaluated between 2D EPI and 3D CASPR in the brain, and between the 2D SShTSE and 3D CASPR acquisition in the renal cortex.

6.3 Application in the Brain

6.3.1 *Arterial Spin Labeling*

Inflowing blood to the brain was labeled using pseudo-Continuous Arterial Spin Labeling (pCASL) [46]. The sequence consisted of a presaturation pulse covering the imaging region, followed by pseudo-continuous labeling, a PLD (to allow labeled blood to perfuse the tissue), and the acquisition. Labeling was applied axially over the carotid arteries for a LD of 1.8 sec [53]. Following a 1.8 sec PLD, images were acquired covering the entire brain.

6.3.2 *Background Suppression and Inflow Saturation*

Background suppression was applied to reduce signal in the background tissue to reduce artifacts due to physiological noise. For the TSE-based images, background suppression was applied using a selective C-FOCI inversion pulse [113] over the brain immediately before labeling, and four non-selective HS inversion pulses were applied during the post-labeling delay [35] to null background tissue signal with a wide range of T1 relaxation rates. Non-selective inversion pulses were applied 30, 200, 675, and 1750 ms before the acquisition. Timing for these pulses were calculated using the label duration and the post-label delay [78].

Inflow saturation pulses were applied axially over a 15 cm slab covering inflowing vessels inferior to the labeling plane. These saturation pulses reduce signal in the major vessels from unlabeled inflowing blood, and were evenly spaced between the four background suppression inversion pulses during the post-label delay.

For the EPI acquisition, background suppression was applied according to the established clinical imaging protocol, with two non-selective HS inversion pulses. The HS pulses were applied 500 and 1000 ms before the acquisition with no inflow saturation.

6.3.3 *Acquisitions*

The proposed 3D CASPR acquisition (Figure 6.1C) was performed in the sagittal plane, and compared against a 2D multi-slice gradient-echo EPI and 3D linear-ordered TSE (Figure 6.1B). The EPI images were acquired in the axial plane to cover the entire brain (resolution: 3x3x5 mm³, number of slices: 24, signal averages: 30). A SENSE reduction factor of 2.3 was used to reduce the overall scan time to 4:20 minutes. The linear 3D TSE images were acquired in the

sagittal plane, similar to CASPR (resolution: $3 \times 3 \times 3 \text{ mm}^3$, number of slices: 56 slices, half scan factor along k_y : 0.6, echo train length: 86). Sagittal CASPR images were acquired with similar parameters as the linear images, and were fully sampled, taking 5:34 minutes. The sagittal TSE acquisitions were reformatted for comparison with the axial EPI images.

6.3.4 Results

Figure 6.2 shows sagittal slices across the brain acquired using 3D linear (A) and 3D CASPR (B) view ordering. CASPR showed reduced physiological noise and improved definition of gray matter features across the brain compared to 3D linear acquisition. Figure 6.3 shows the repetitions of 2D EPI pCASL in a single slice of the brain (A), including significant signal variations across each dynamic. Generating a perfusion-weighted image from the average of these repetitions reduces random signal variations (B). Compared to EPI, the axial reformat of 3D CASPR in the same slice (C) shows improved SNR due to the repeated acquisition of central k -space. This allows for acquisition of the whole volume in a similar scan time without additional signal averages.

Figure 6.4 shows quantified perfusion maps across the brain measured with (A) EPI and (B) reformatted 3D CASPR. Perfusion homogeneity is compared in

Figure 6.5 (A) for each gray matter ROI across the brain. Increased perfusion homogeneity, indicated by a lower RD, is observed in each region of the brain with 3D CASPR compared to 2D EPI ($p < 0.01$). The agreement between 2D EPI and 3D CASPR is compared using Bland-Altman analysis in Figure 6.5 (B), where no significant bias was found between the measurements.

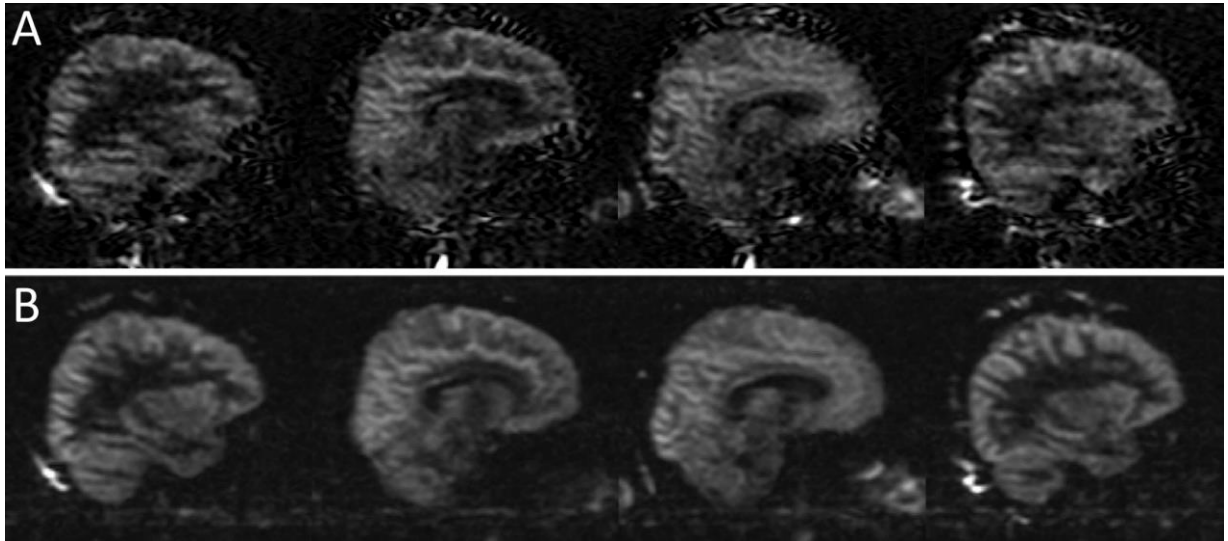


Figure 6.2: Multiple slices showing complete brain coverage using 3D TSE pCASL with (A) linear and (B) CASPR trajectories.

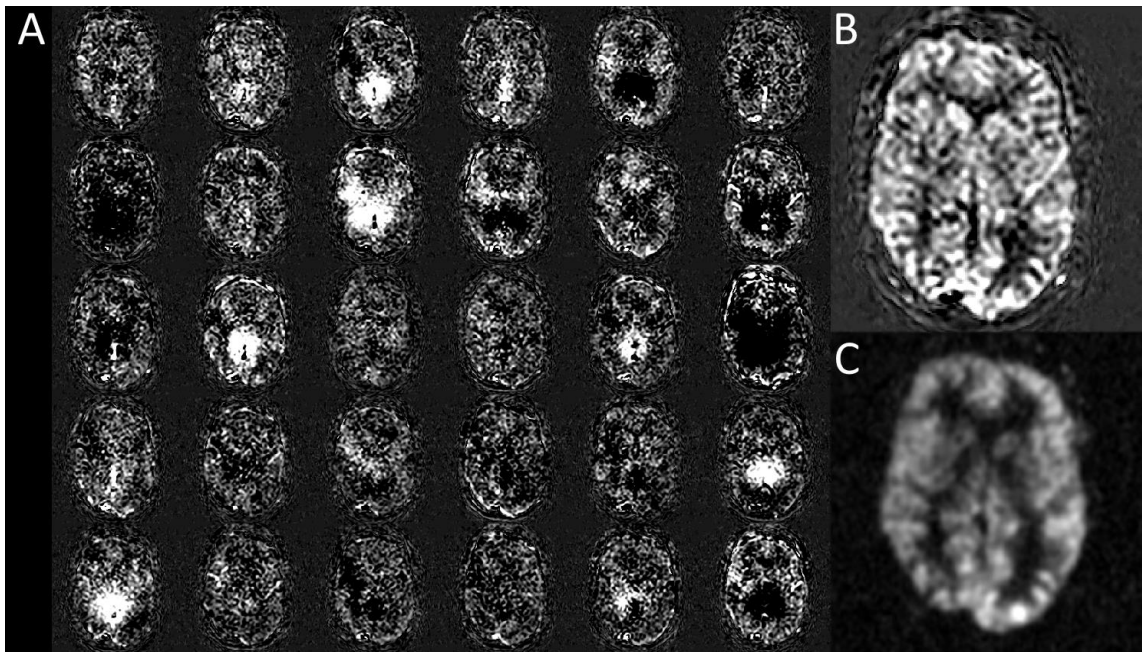


Figure 6.3: Brain perfusion images of the same slice acquired using (A) 30 repetitions of 2D pCASL EPI, (B) average EPI image from 30 repetitions, and (C) 3D TSE with CASPR View Ordering. The 3D TSE images are axial reformats from a sagittal acquisition.

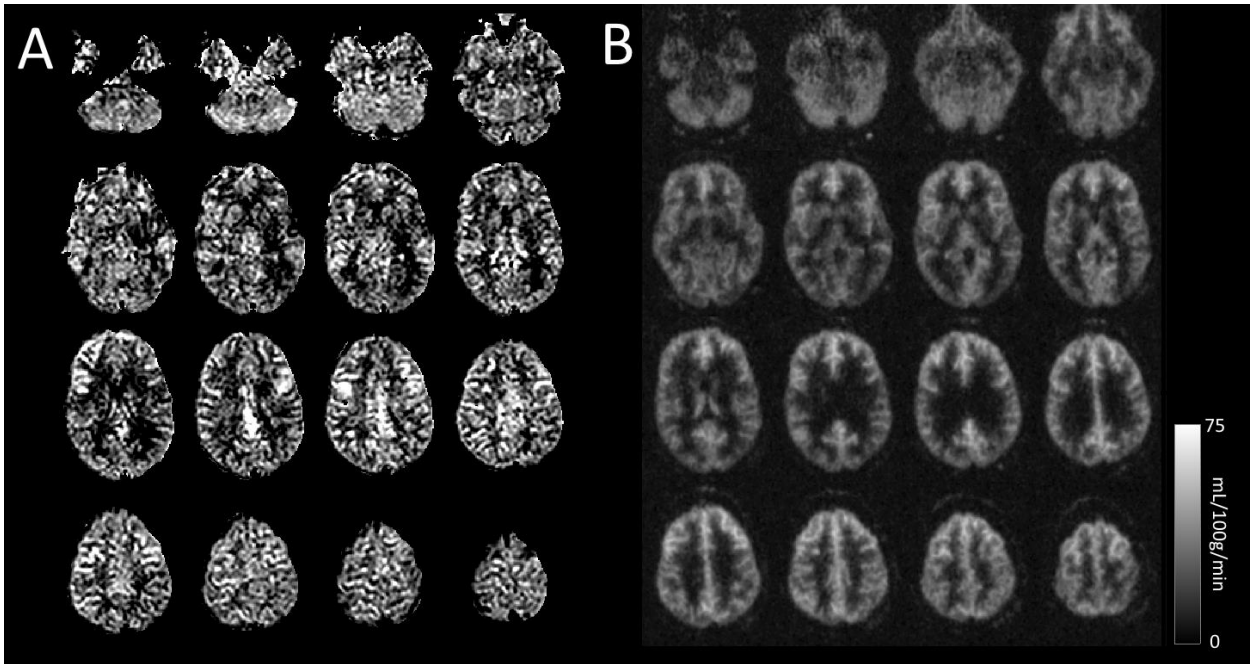


Figure 6.4: Axial quantified perfusion slices through the brain acquired with (A) 2D pCASL EPI and (B) reformatted 3D CASPR.

6.4 Application in the Kidneys

6.4.1 Arterial Spin Labeling

Inflowing blood to the kidneys was labeled using pCASL [46]. The sequence consisted of a presaturation pulse covering the imaging region, followed by pseudo-Continuous labeling, a post-label delay (to allow labeled blood to perfuse the tissue), and the acquisition. Labeling was applied axially over the descending aorta for 1.5 s, with a 1.5 s PLD, followed by a coronal acquisition. A guided breathing approach was used during imaging to reduce motion artifacts [35]. Subjects were given breathing instructions in synchronization with the 6 s TR of the pCASL sequence, and were instructed to breathe in and out during labeling and the PLD, and to hold their breath at end-expiration until the image acquisition was completed.

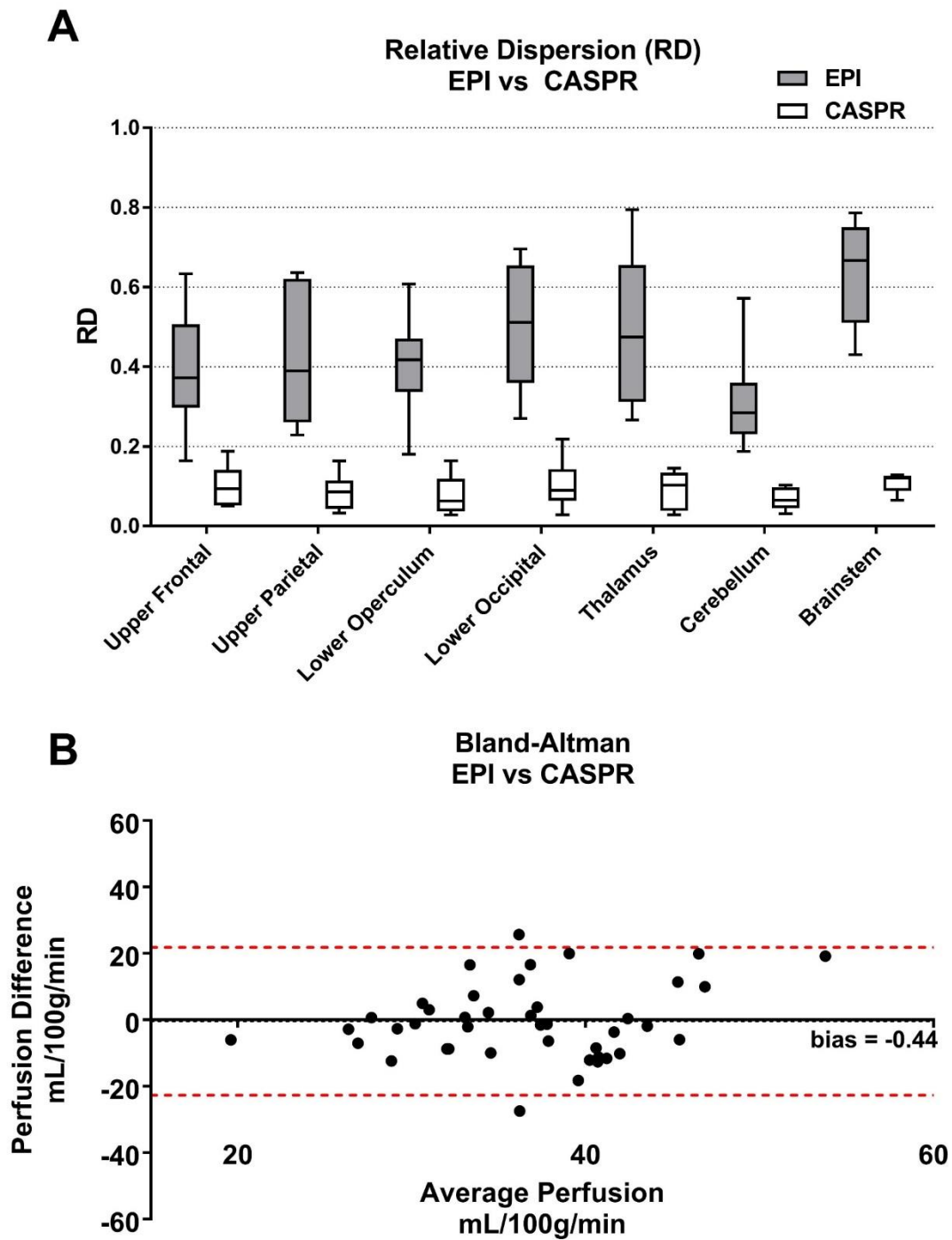


Figure 6.5: (A) Relative dispersion in each ROI across the brain for both acquisitions, showing more homogenous perfusion with CASPR. (B) Bland-Altman analysis of mean quantified perfusion measurements in each ROI across the brain showed no significant bias between the techniques. 95% confidence intervals of the agreement are shown in red.

6.4.2 *Background Suppression and Inflow Saturation*

Background suppression was applied to reduce physiological noise and motion artifacts that could be introduced by the guided-breathing approach. Background suppression was applied using a selective C-FOCI inversion pulse [113] over the kidneys immediately before labeling. Four additional non-selective HS inversion pulses were applied 48, 239, 671, and 1491 msec before the acquisition [35]. Timing for the non-selective background suppression pulses were calculated using the label duration and the post-label delay [78] .

Inflow saturation pulses were applied axially over a 15 cm slab to cover inflowing vessels superior to the labeling plane. These saturation pulses reduce signal in the major vessels from unlabeled inflowing blood, and were evenly spaced between the four background suppression inversion pulses during the post-labeling delay.

6.4.3 *Acquisitions*

In the kidneys, the CASPR images were acquired in the coronal plane, and compared with a coronal 3D Linear TSE and coronal 2D SShTSE partial k-space acquisition with 16 signal averages [35]. 3D CASPR was also acquired with and without SENSE (2x acceleration) to increase slice resolution in the same scan time.

6.4.4 *Results*

Perfusion-weighted images acquired in the kidney with linear view ordering and CASPR are shown in Figure 6.6. Linear ordering (A), which passes through the center of k-space halfway through the acquisition, shows significant artifacts from physiological noise and respiratory motion. These signal variations are averaged out over the duration of the CASPR acquisition (B)

as the center of k-space is repeatedly sampled. This vastly improved the visualization of sub-structures in the renal cortex.

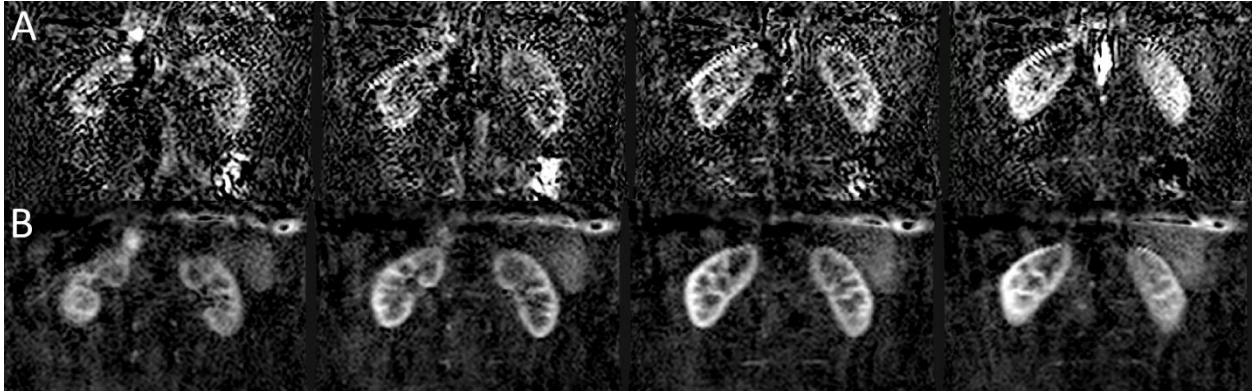


Figure 6.6: Coronal perfusion-weighted images across the kidney acquired with (A) 3D linear-ordered and (B) 3D CASPR TSE, showing reduced artifacts due to physiological noise with CASPR.

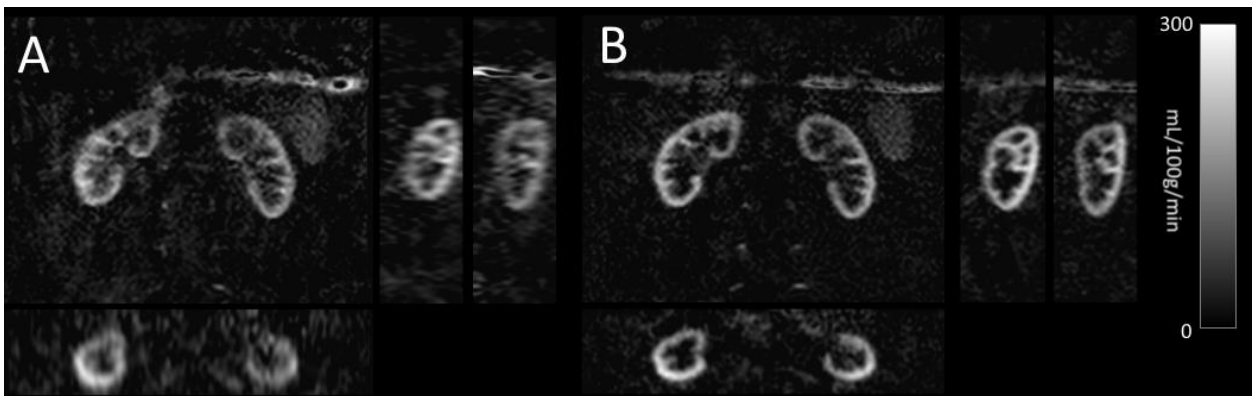


Figure 6.7 shows quantified kidney perfusion maps acquired with 2D SShTSE in a single slice (A), and the volumetric acquisition of the entire kidney (B) that can be acquired in a similar scan time. Motion introduced between dynamic scans due to the respiratory cycle can lead to blurring of anatomical structures in the kidney when the 2D repetitions are averaged together, but 3D CASPR preserved these details with an identical timed-breathing approach, allowing for improved corticomedullary differentiation.

Figure 6.8 shows quantified 3D CASPR perfusion images and orthogonal reformats acquired in the same volunteer as Figure 6.6. Images were acquired with 6mm slice thickness reconstructed to 3mm (A), and 3mm slice thickness with a SENSE factor of 2, reconstructed to 1.5mm (B). 3D CASPR provided sufficient SNR for acceleration to achieve higher slice resolution in the same scan time, allowing for improved differentiation of the cortex.

Agreement between quantified perfusion in the renal cortex in five volunteers with 2D SSHTSE and 3D CASPR is evaluated with Bland-Altman analysis in Figure 6.9, showing no significant bias between the acquisitions.

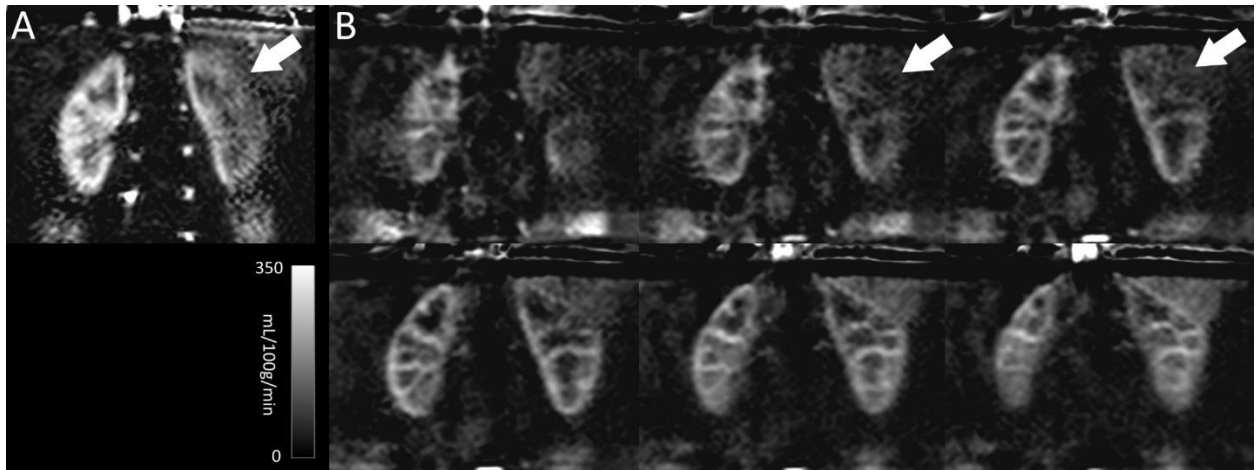


Figure 6.7: Quantified perfusion images acquired using (A) 2D SSHTSE and (B) 3D CASPR.

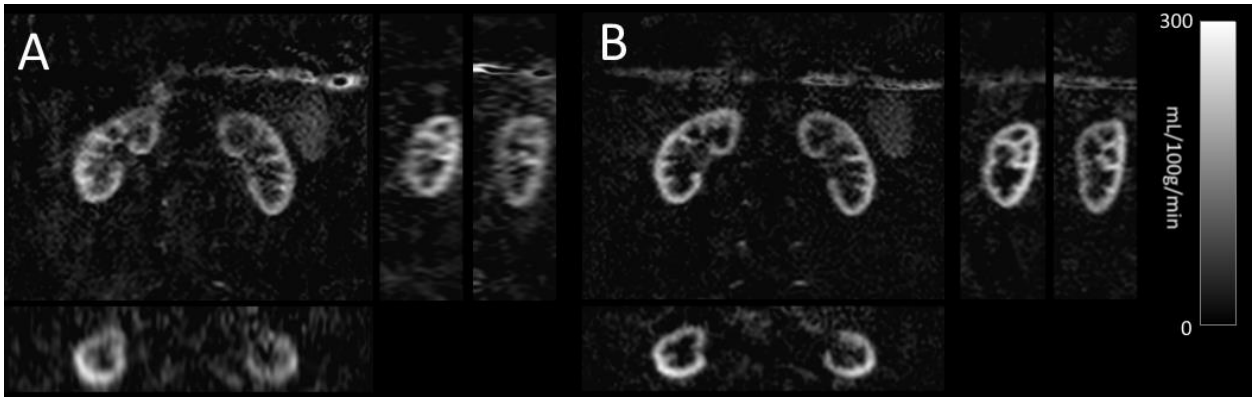


Figure 6.8: Coronal kidney CASPR acquisition with axial and sagittal reformats, acquired with (A) 3x3x6mm resolution (B) 3x3x3mm with a SENSE factor of 2, acquired in the same scan time.

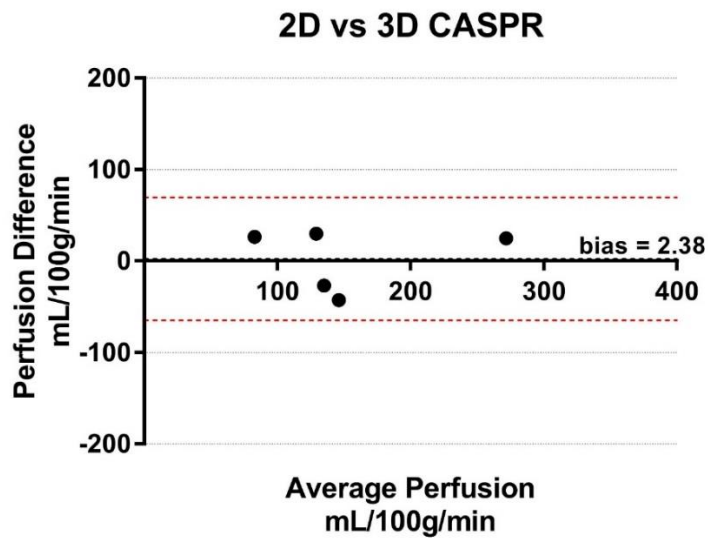


Figure 6.9: Bland-Altman analysis of perfusion to the renal cortex. Perfusion measured with 2D SSHTSE and 3D CASPR agreed in all 5 subjects, and no significant bias was found between the techniques. 95% confidence intervals of the agreement are shown in red.

6.5 Discussion

This study demonstrated successful implementation of a 3D Cartesian Acquisition with Spiral PRofile ordering (CASPR) sampling technique, which provides a more robust acquisition

for 3D perfusion imaging than the linear TSE. With ASL acquisitions, it is critical to consistently sample the labeled signal for improved image quality and sufficient SNR. The CASPR trajectory repeatedly samples the center of k-space at the beginning of each repetition, maximizing the measured signal. The spiral ordering also allows the center of k-space to be densely sampled early in each echo train, allowing for extended echo trains and shorter scan times. To achieve sufficient SNR in 2D ASL images, multiple signal averages are acquired. Due to SNR improvements and extended echo trains offered by 3D CASPR, complete coverage of the brain and kidneys was achieved in similar scan times as multiple 2D signal averages.

In the brain, 3D CASPR showed improved image quality and reduced noise compared to the 3D linear TSE. Since CASPR is more robust to the random signal variations observed across repetitions of 2D EPI, it also provided improved image quality over the EPI images with multiple signal averages. In the selected ROIs across the brain, perfusion measured with 3D CASPR was more homogeneous than that measured with the multi-slice EPI and 3D linear TSE acquisitions. This result suggests that 3D CASPR is less sensitive to the random signal variations observed in other acquisitions. Quantified perfusion values were also shown to have no bias between the EPI and CASPR acquisitions.

CASPR significantly improved the visualization of renal structures, which were obscured by significant artifacts in the linear ordered 3D TSE. Quantified perfusion values agreed between 2D SSHTSE and 3D CASPR images, though measurements in a larger number of subjects would help confirm this agreement. The SNR improvements offered by the CASPR view ordering also enabled 2x SENSE acceleration with a 2x increase in slice resolution. Using SENSE acceleration while increasing the resolution improved differentiation of the renal cortex and medulla in the

same scan time. Due to the Cartesian sampling, the CASPR trajectory is also readily amenable to pseudo-random undersampling with compressed sensing reconstruction to significantly reduce the scan time [114, 115].

The CASPR view ordering is currently being evaluated to measure perfusion in renal cell carcinoma (RCC). In these patients, ASL-measured perfusion has been shown to correlate well with tumor vascularity [14, 40], and could be used as a biomarker of tumor angiogenesis to assess treatment response. In upcoming studies, 3D CASPR will also be applied to evaluate tumor response to chemoradiation and antiangiogenic therapy in patients with glioblastoma (GBM) and RCCs [116].

In the future, 3D CASPR will be applied for pulmonary perfusion mapping. Since this trajectory is less sensitive to respiratory motion and physiological noise, it may also improve the SNR of volumetric acquisitions across the lungs. Our initial experience with CASPR and pCASL labeling in the lungs is briefly explored in Chapter 8.

CHAPTER 7

A PERFUSION PHANTOM FOR QUALITY CONTROLLED MEASUREMENT OF ARTERIAL SPIN LABELED PERFUSION*

7.1 Introduction

Arterial spin labeling is a rapidly growing area of interest with significant clinical potential, primarily because it can provide non-invasive quantitative perfusion maps. ASL-measured quantitative perfusion can provide a direct measurement of tumor vasculature and has been shown to have clinical utility in therapy response monitoring of various cancers, including glioblastoma (GBM) [117] and renal cell carcinoma (RCC) [39, 40]. While ASL has been shown to be accurate in vivo with respect to ^{15}O PET [57, 58], true assessment of its reproducibility, or precision, will require multiple repeated measurements of known absolute perfusion values. Due to the high number of measurements required and variations in normal physiology, determining the true precision of ASL is not feasible in vivo. Errors can also be introduced to ASL measurements by several confounding factors such as manufacturer-specific signal scaling, image reconstruction technique, and labeling efficiency, which can be influenced by flow velocity and B_0 inhomogeneities [86]. Due to these uncertainties, regular quality assurance checks are needed to ensure consistent perfusion values can be attained.

To meet this need, we modified an existing diffusion imaging phantom for ASL perfusion imaging. After initial testing, we designed a new 3D-printed perfusion phantom to mimic the

* This work is in preparation for publication submission. Portions of this work were presented at the 25th, 26th, and 27th annual meetings of the ISMRM in Singapore (May 2016), Honolulu (April 2017), and Paris (June 2018).

branching of arterial vessels. This approach allows for straightforward reproduction of the phantom so the precision of ASL-measured perfusion across scanner field strength, manufacturer, and imaging site can be validated.

7.2 Perfusion phantom

7.2.1 Design

The initial perfusion phantom was modified from a diffusion phantom in our department [118, 119], which used sponges with different densities embedded within poly-vinyl carbon (PVC) pipes (Figure 7.1). Three tubes containing the sponges were split from a common plastic tubing. The entire set-up was submerged in a water bath to minimize B_0 inhomogeneities. A pump outside the MR scanner room circulated water through the tubing. The pump was set to different flow rates (0-300 mL/min) to create varied perfusion effects, which was measured using pCASL in the sponges. Axial perfusion-weighted images were acquired through the center of the sponges using a SSHTSE acquisition after 6 sec of labeling for all perfusion measurements (Figure 7.2). A proton-density image was acquired separately to quantify perfusion using the standard ASL model [31]. To evaluate the precision of pCASL measurements, average perfusion in each sponge was compared with expected perfusion. Phase contrast velocity measurements were made to calculate flow rate in each branch of the tubing. The flow rate (mL/min) was divided by the sponge volume to calculate perfusion in mL/mL/min. An assumed partition coefficient of the sponge, λ (g/mL), used for conversion to mL/g/min, was omitted from quantification until it can be estimated in the future. Finally, pCASL measurements were repeated with identical pump flow rates a week apart to evaluate the repeatability of pCASL measured quantitative perfusion.



Figure 7.1: Original phantom design with three sponges in line with the tubing submerged in a water bath.

7.2.2 Results

Figure 7.2a shows a coronal T2-weighted image of the 3 sponges and the pCASL labeling plane shown in red. To show the effects of labeling duration, labeling was applied for 2 sec (b) and 6 sec (c), showing an extended perfusion bolus with the longer labeling duration. Figure 7.3 shows a linear increase in pCASL-measured perfusion as the pump flow rate is increased, showing a good correlation for sponge 1 and 2 (blue and green ROIs). Sponge 3 (red ROI) has the highest density and serves as a control measurement providing close to zero perfusion.

Bland-Altman analysis showed excellent reproducibility of pCASL measurements acquired one week apart (Figure 7.4). Figure 7.5 (A) shows quantified perfusion compared to the estimated perfusion based on the flow rate to each sponge. Perfect agreement is shown by the unity line. Measured perfusion was consistently below estimated perfusion. Bland-Altman analysis (B) also showed a negative bias in ASL measurements, especially at perfusion rates above 10 mL/mL/min.

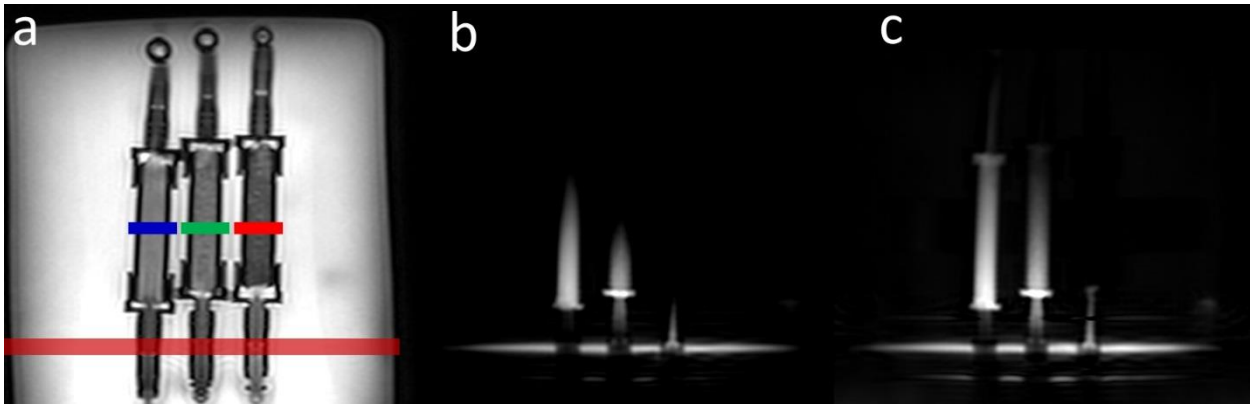


Figure 7.2: (a) Coronal T2W image of the flow phantom. The labeling plane is shown in red. (b) perfusion-weighted image with labeling applied for 2 seconds (c) perfusion-weighted image with labeling applied for 6 seconds. Both perfusion images had a post-label delay of 100ms and a flow rate of 300mL/min. The sponge on the right is denser than the other two, and serves as a control with close to zero perfusion. Colored ROIs used for perfusion measurements are shown in (a).

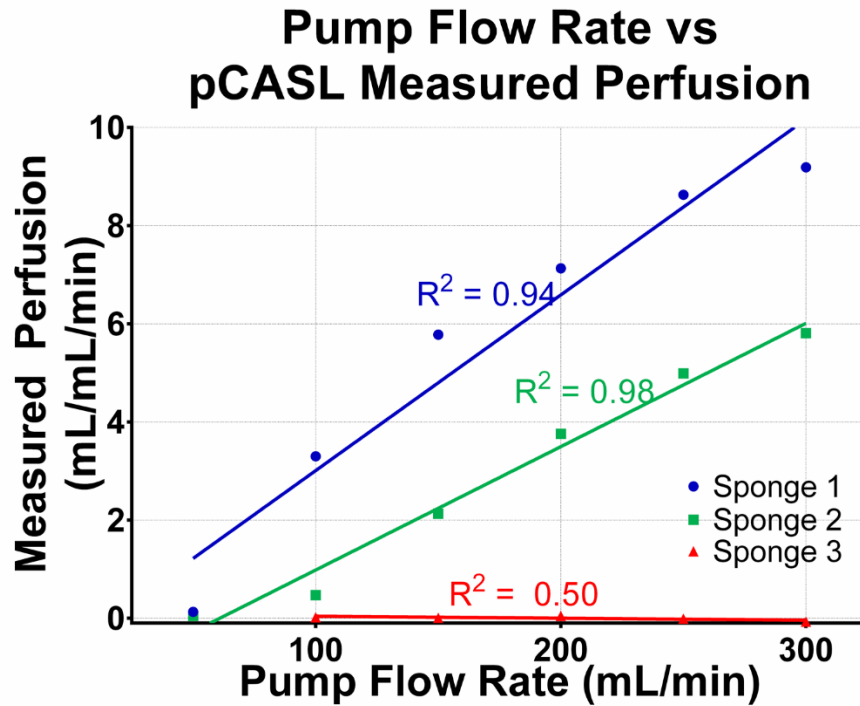


Figure 7.3: Pump flow rate vs. measured pCASL perfusion in three sponges, showing increased perfusion with increasing flow rate in each sponge.

pCASL Reproducibility

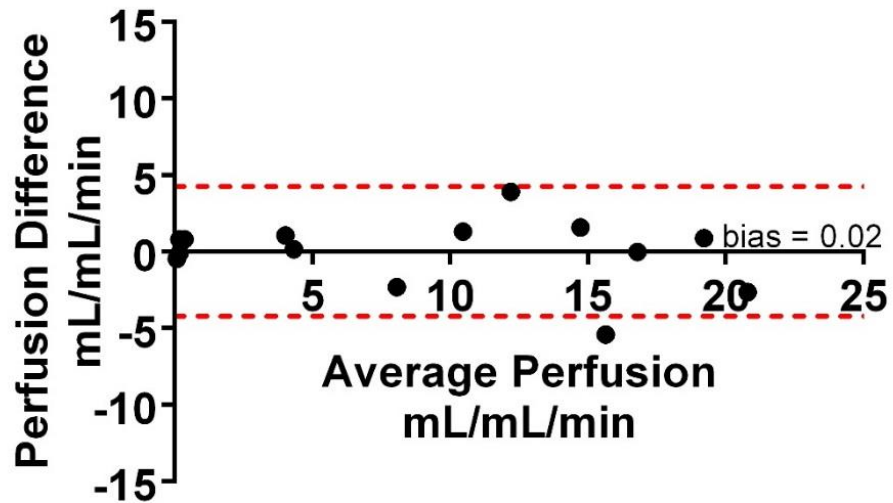
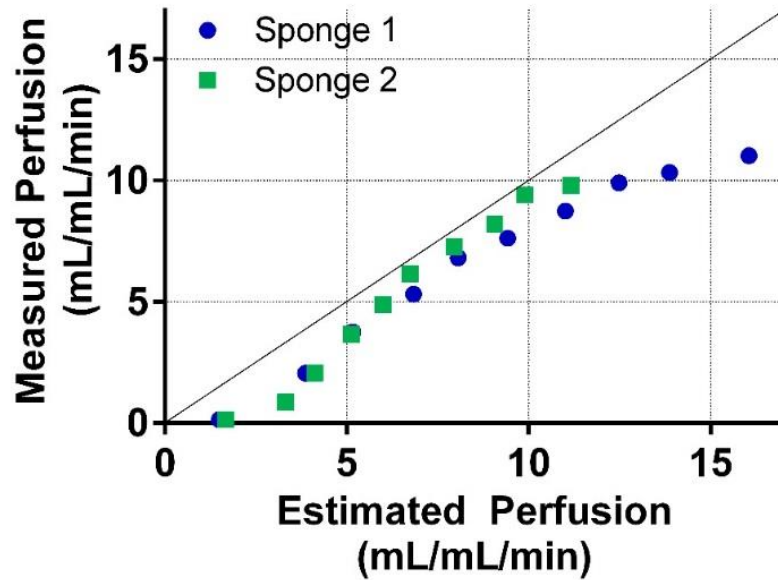


Figure 7.4: pCASL perfusion measurements in the same sponges with identical flow rates on different days, performed a week apart.

Perfusion measurements made in this initial phantom design were highly reproducible on different scan dates. However, the accuracy of the measurements suffered at higher flow rates. This is likely a limitation of the phantom design: the existing water in the sponge is completely replaced with labeled water at high flow rates. This results in a maximum perfusion rate that can be measured with ASL. Since sponge 1 was the least dense and received the highest flow rates, it suffered the most from this perfusion-tapering effect (Figure 7.5). To overcome this problem, a new perfusion phantom was designed to split inflowing water into multiple branches.

A Measured vs Estimated Perfusion



B Bland-Altman Measured vs Estimated Perfusion

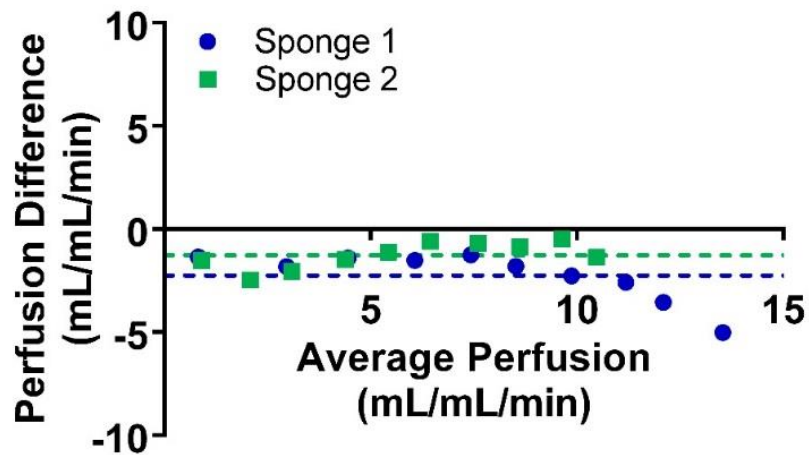


Figure 7.5: (A) Estimated perfusion compared with measured pCASL perfusion. (B) Bland-Altman analysis shows a negative bias in the ASL measurements. The perfusion signal in sponge 1 can be seen tapering off at, particularly at higher perfusion rates in both (A) and (B).

7.3 3D printed perfusion phantom

7.3.1 Design

The new phantom design (Figure 7.6) splits the circulating water in multiple branches, mimicking the branching of arterial vessels. The branches terminate at small evenly-spaced holes leading into a large chamber that holds a sponge. The small evenly-spaced holes ensure that the entire sponge is completely perfused. The water then exits the phantom through a mirror image of the input branches. The phantom was submerged in a water bath to minimize B_0 inhomogeneities. The pump outside the MR scanner room circulated water through the tubing. Perfusion was measured with 2D FAIR and 2D pCASL to assess the agreement between the ASL techniques. Images were acquired using a SSHTSE acquisition. Quantitative perfusion values were calculated using standard models for PASL and CASL [31]. pCASL labeling was applied axially over the inflowing tube for 500 msec, followed by a variable (0-5500 msec) PLD before imaging. The variable PLD allows the inflowing perfusion bolus to be sampled as it flows into the sponge. The inversion time for FAIR was varied to match the pCASL PLD. The pump flow rate was varied from 0 to 1000 mL/min to vary perfusion in the sponge. A proton density weighted image was also acquired through the sponge at each flow rate for perfusion quantification. The agreement between FAIR and pCASL quantitative measurements was assessed at varied flow rates. Finally, ASL measurements were repeated using the same pump flow rates on two different days to evaluate the repeatability of ASL measured quantitative perfusion.

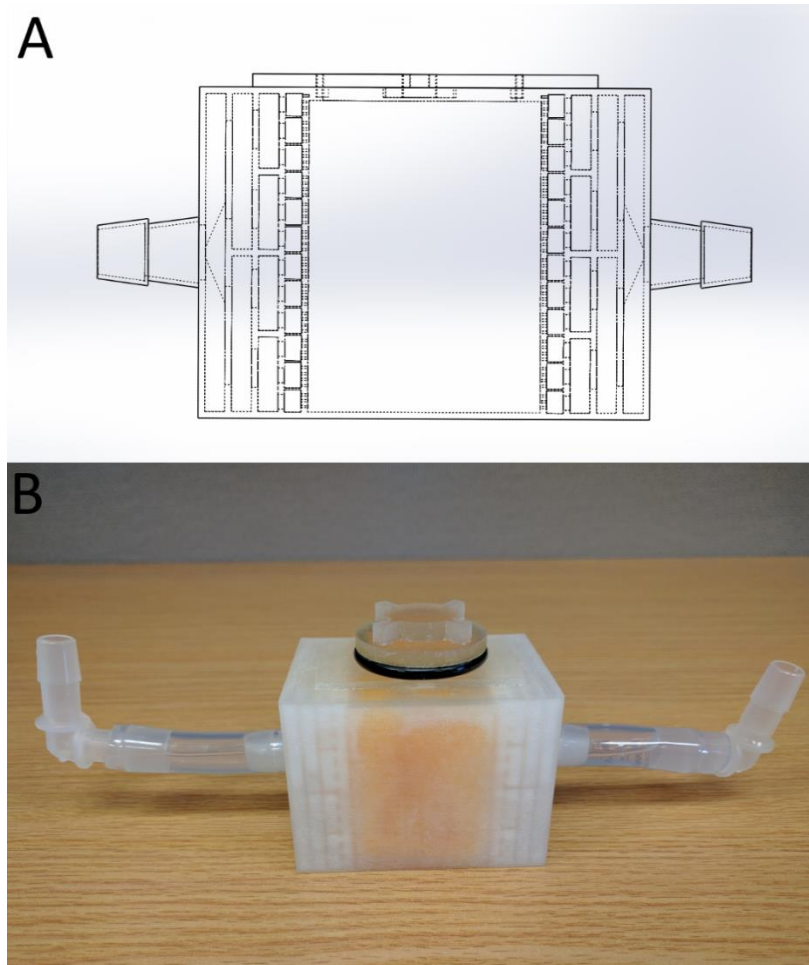


Figure 7.6: Phantom schematic (A) with branching inflow vessels that terminate in the larger sponge chamber, and (B) 3D printed phantom containing a sponge with sealed lid and input/output tubes to be connected to the pump.

7.3.2 Results

Figure 7.7 shows axial perfusion weighted images acquired with FAIR and pCASL throughout the inflow of the labeled perfusion bolus, showing similar flow patterns. Figure 7.8 shows average perfusion in the sponge acquired at varied post-label delays and at different pump flow rates. FAIR data was fitted to the PASL perfusion model, and pCASL was fitted to the CASL model. The expected increase in SNR of perfusion-weighted images was achieved with pCASL

compared to FAIR, indicated by the magnitude of the perfusion signal curves. Figure 7.9 (A) shows linearly-increasing measured perfusion as a function of the pump flow rate, showing a good correlation in both ASL techniques.

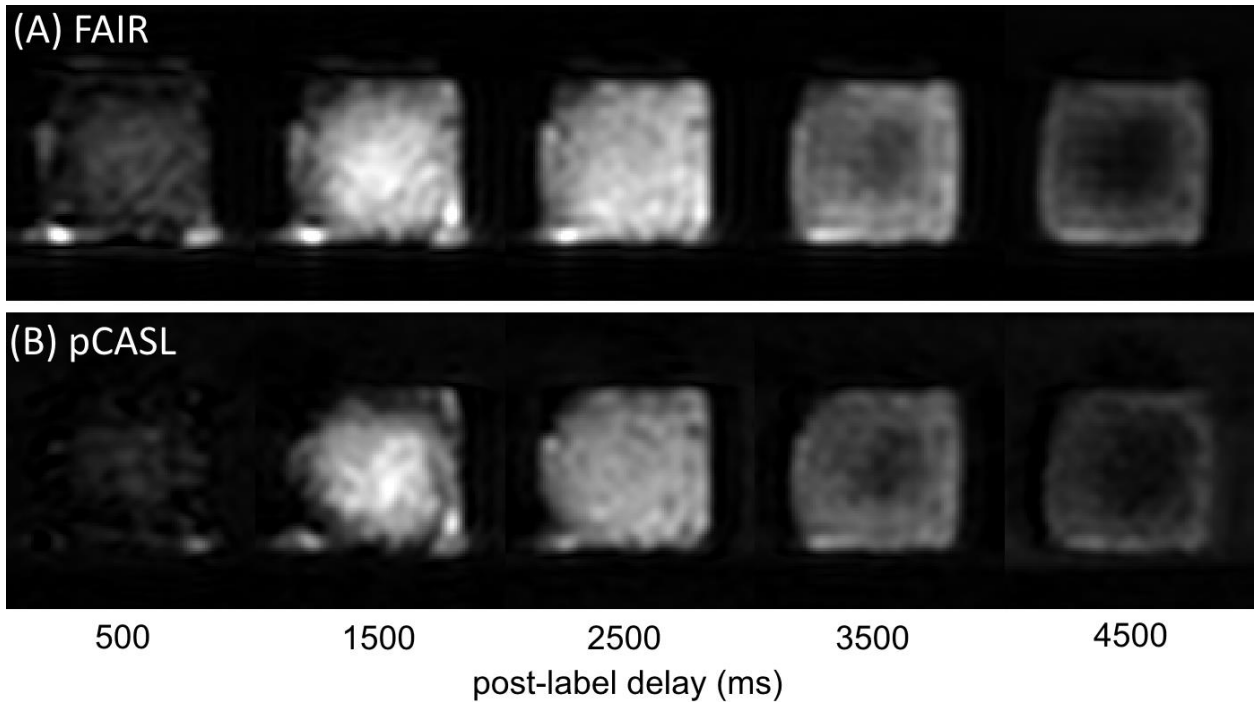


Figure 7.7: Perfusion-weighted images at varied post-label delays acquired with (A) FAIR and (B) pCASL.

Bland-Altman analysis of repeated FAIR and pCASL measurements (Figure 7.10) demonstrated consistency between scan dates. A longitudinal study of this phantom will further verify the reproducibility of ASL measurements.

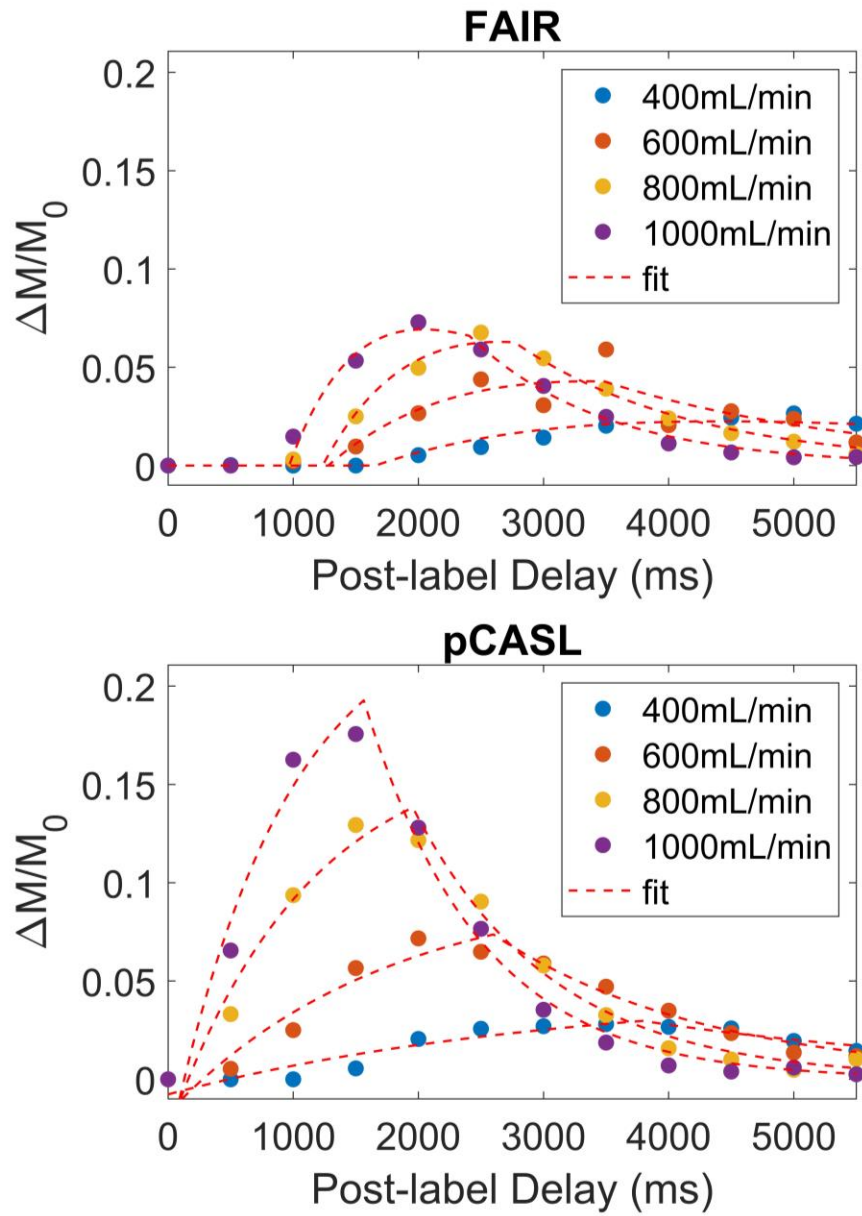


Figure 7.8: Average ASL signal in the sponge at varied PLDs and flow rates acquired with FAIR and pCASL.

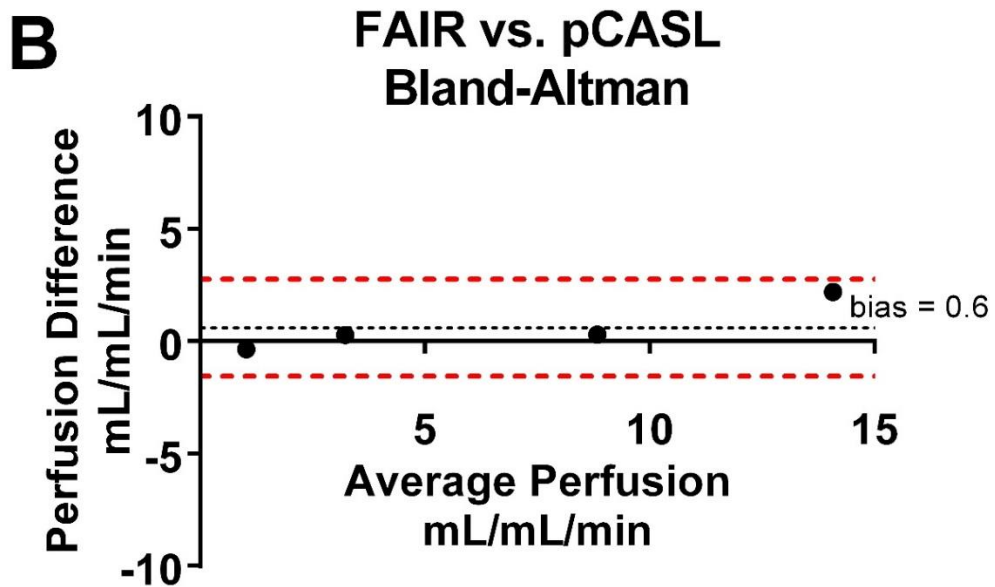
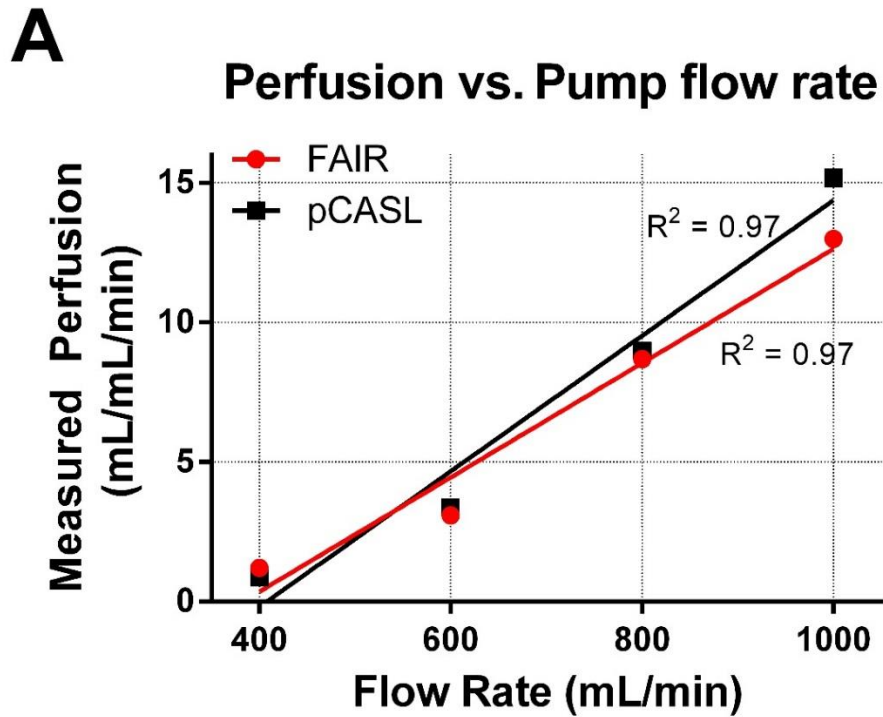


Figure 7.9: Analysis of the agreement between FAIR and pCASL measured perfusion. (A) shows linearly-increasing perfusion as the pump flow rate is increased. (B) shows Bland-Altman analysis of the agreement between FAIR and pCASL measurements.

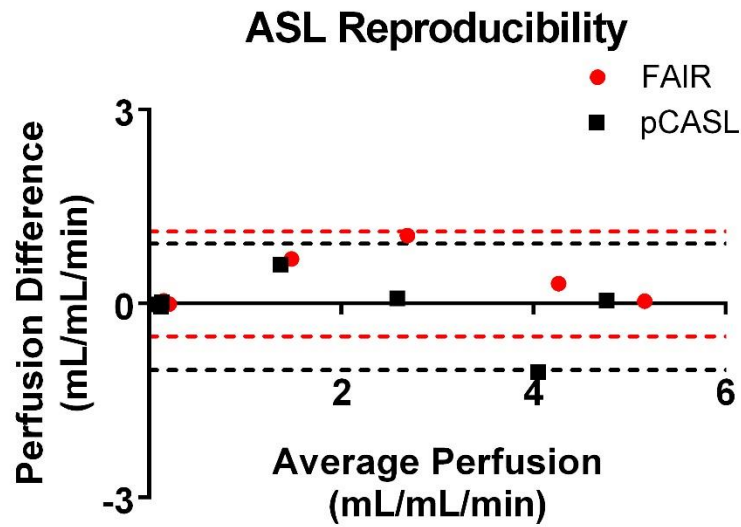


Figure 7.10: Bland-Altman analysis of the reproducibility of FAIR and pCASL quantitative perfusion measurements.

7.4 Discussion

Accurate and reliable measurements of quantitative perfusion is of utmost importance in establishing ASL as a quantitative biomarker for therapy response in clinical trials. We demonstrated a simple 3D printed perfusion phantom that can serve as a quality control to ensure reliable and precise ASL perfusion measurements. We also used the phantom to show that various ASL techniques can provide the same quantitative values. The initial phantom design could be used to establish the precision of ASL-measured perfusion, though the accuracy suffered at moderate flow rates. The 3D printed phantom mimics the perfusion effects shown by the general kinetic model used for in vivo perfusion quantification [31]. The reproducibility of perfusion measurements was demonstrated, and good agreement was observed between the FAIR and pCASL techniques.

Future experiments with the 3D printed phantom will include additional reproducibility testing by establishing a regular scanning schedule. By defining the expected perfusion values at various flow rates, the accuracy of ASL measurements can be confirmed. A range of flow rates in which this phantom design provides a linear increase in measured perfusion will also be identified. This 3D printed phantom could be potentially used as a tool to study technical developments to ASL sequences without the need for volunteer recruitment. Improvements in labeling efficiency can be validated in a phantom before introducing the additional complications introduced by in vivo imaging.

In conclusion, this 3D printed phantom can be easily replicated to serve as a quality control phantom at different sites to validate ASL-measured perfusion regardless of scanner manufacturer, imaging site, or field strength. This will help establish ASL as an accurate and precise perfusion measurement technique.

CHAPTER 8

DISCUSSION AND FUTURE DIRECTIONS

The work presented in this dissertation was performed to make arterial spin labeling more valuable for clinical non-contrast evaluation of pulmonary perfusion. First, the initial feasibility of FAIR at 3T was demonstrated, despite concerns about increased B_0 inhomogeneities at higher field strength. Quantification of pulmonary perfusion was shown to be highly reproducible, and masking of bright signal in the pulmonary vasculature enabled measurement of the underlying tissue perfusion.

The technical advancements made with the FAIR technique at 3T made the sequence more robust to respiratory motion, reduced signal in the major pulmonary vasculature, and allowed for multi-slice imaging across the entire lung. Our results showed that the C-FOCI pulse provided improved background suppression in fat tissues than the HS pulse, in agreement with Bloch simulations. Inflow saturation successfully reduced bright signal in the pulmonary vasculature, allowing visualization of underlying tissue perfusion. While the results of these techniques was very encouraging, further evaluation is needed in a larger number of subjects and patients to optimize inflow saturation timing and for reproducibility verification. Quantitative perfusion values need to be calculated and validated before multi-slice FAIR can become a viable clinical imaging technique.

Our application of the pCASL technique revealed the significance of proper cardiac triggering for lung perfusion imaging. While consistent diastolic acquisitions are known to be important for ASL [60], our results emphasized the influence of normal variations in heart rate and extended repetition times of the pCASL sequence. Our experience should prevent this

phenomenon from being overlooked in future lung ASL studies. pCASL RPA labeling with a cardiac triggered acquisition also provided consistent repetitions of pCASL perfusion images. In order to make this approach more robust, future efforts should include making pCASL less sensitive to pulsatile flow and B0 inhomogeneities near the lungs [86, 87].

Following our experiences and technical developments with FAIR and pCASL in the lungs, a novel pCASL IVC labeling approach was proposed to understand flow patterns in pediatric patients with Fontan circulation. pCASL measurements of differential IVC flow were validated, showing very good agreement with 4D-flow in 15 patients with Fontan circulation. This non-invasive approach to simultaneously assess quantitative pulmonary perfusion and differential IVC flow has the potential to provide longitudinal monitoring without the risks associated with existing imaging techniques.

To overcome the challenges associated with standard linear-ordered 3D TSE for body applications, a Cartesian Acquisition with Spiral PRofile Ordering (CASPR) was proposed and demonstrated in the brain and kidney. The proposed view ordering was particularly beneficial in the kidneys, where it enabled robust perfusion measurements, a result that the linear-ordered 3D TSE could not provide.

In the future, CASPR will be applied for volumetric perfusion mapping of the lungs with both FAIR and pCASL. Lung imaging with 3D CASPR was briefly explored using sagittal pCASL labeling of the RPA and a cardiac-triggered acquisition. Figure 8.1 shows sagittal pCASL perfusion weighted images acquired through the right lung. Figure 8.2 shows a sagittal slice in the same volunteer with axial (B) and coronal (C) reformats. As shown in these figures, the acquisition

still requires optimization to improve SNR and reduce blurring. However, CASPR was able to capture ASL signal in the lungs, while in our experience, the linear-ordered 3D TSE could not.

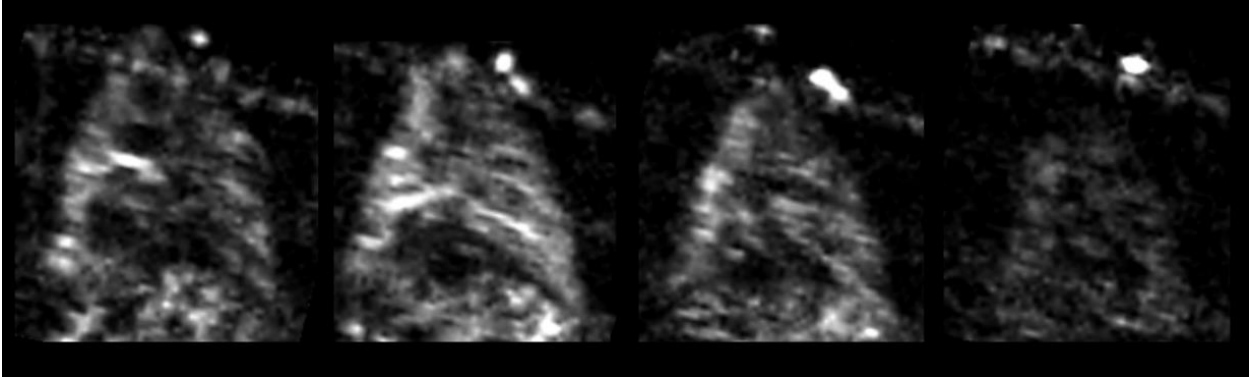


Figure 8.1: Sagittal perfusion-weighted images acquired through the lung using pCASL labeling of the RPA and a cardiac-triggered 3D CASPR acquisition.

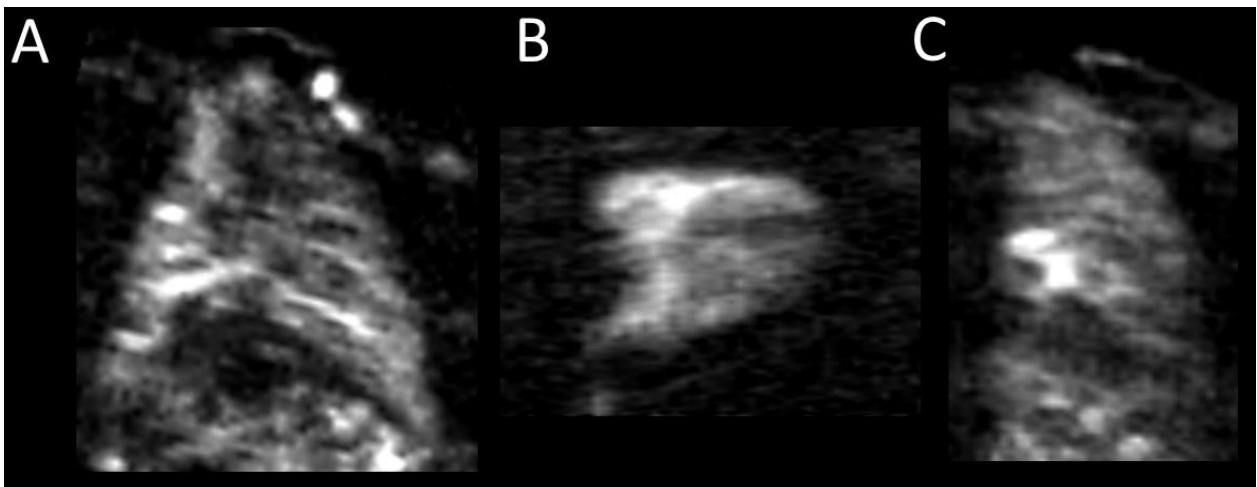


Figure 8.2: 3D perfusion-weighted image acquired with pCASL with CASPR view ordering in the sagittal plane (A), with axial (B) and coronal (C) reformats.

Finally, for ASL perfusion imaging to be adopted for clinical management of lung disease, quantitative measurements must be shown to be highly reproducible. Due to the complications introduced by normal physiological variations in vivo, a standardized perfusion phantom would

help establish the precision of ASL measurements. Though no phantom design has been widely accepted for ASL imaging, the 3D printed model approach makes reproduction of the phantom across different research sites straightforward and inexpensive. Our experiences with this design showed good agreement with the standard ASL model for PASL and CASL. A regular scanning schedule will be set up in the future to establish the achievable precision of this phantom design at varied perfusion rates.

In conclusion, the work contained in this dissertation addressed various technical challenges encountered while extending arterial spin labeling to the lungs for volumetric perfusion mapping. Substantial improvements were made in the reproducibility and SNR of pulmonary perfusion measurements. In the future, validation of quantitative measurements in the lungs should be performed using the imaging gold standard, ^{15}O PET. Demonstrating the accuracy and precision of ASL will help establish it as a quantitative imaging biomarker for the management of chronic pulmonary diseases.

REFERENCES

- [1] D. Schraufnagel, "Breathing in America: Disease, Progress, and Hope," *American Thoracic Society*, 2010.
- [2] B. Dunlap and G. Weyer, "Pulmonary Hypertension: Diagnosis and Treatment," *American family physician*, vol. 94, no. 6, 2016.
- [3] M. McGoon *et al.*, "Screening, early detection, and diagnosis of pulmonary arterial hypertension: ACCP evidence-based clinical practice guidelines," *Chest*, vol. 126, no. 1, pp. 14S-34S, 2004.
- [4] J. M. Renaud, R. Klein, and R. S. Beanlands, "Radionuclide tracers for myocardial perfusion imaging and blood flow quantification," *Cardiology clinics*, vol. 34, no. 1, pp. 37-46, 2016.
- [5] N. Tunariu, S. J. Gibbs, Z. Win, and W. Gin-Sing, "Ventilation-perfusion scintigraphy is more sensitive than multidetector CTPA in detecting chronic thromboembolic pulmonary disease as a treatable cause of pulmonary hypertension," *The Journal of Nuclear Medicine*, vol. 48, no. 5, p. 680, 2007.
- [6] N. Galiè *et al.*, "2015 ESC/ERS guidelines for the diagnosis and treatment of pulmonary hypertension: the Joint Task Force for the Diagnosis and Treatment of Pulmonary Hypertension of the European Society of Cardiology (ESC) and the European Respiratory Society (ERS): endorsed by: Association for European Paediatric and Congenital Cardiology (AEPC), International Society for Heart and Lung Transplantation (ISHLT)," *European heart journal*, vol. 37, no. 1, pp. 67-119, 2015.
- [7] G. G. King, B. Harris, and S. Mahadev, "V/Q SPECT: utility for investigation of pulmonary physiology," in *Seminars in nuclear medicine*, 2010, vol. 40, no. 6, pp. 467-473: Elsevier.
- [8] J. Meng *et al.*, "A comparison of ventilation/perfusion single photon emission CT and CT pulmonary angiography for diagnosis of pulmonary embolism," *Chinese journal of tuberculosis and respiratory diseases*, vol. 36, no. 3, pp. 177-181, 2013.
- [9] M. S. Pearce *et al.*, "Radiation exposure from CT scans in childhood and subsequent risk of leukaemia and brain tumours: a retrospective cohort study," *The Lancet*, vol. 380, no. 9840, pp. 499-505, 2012.
- [10] P. Rajiah, "The Evolving Role of MRI in Pulmonary Hypertension Evaluation: A Noninvasive Approach from Diagnosis to Follow-up," ed: Radiological Society of North America, 2018.

- [11] K. Nikolaou *et al.*, "Quantification of pulmonary blood flow and volume in healthy volunteers by dynamic contrast-enhanced magnetic resonance imaging using a parallel imaging technique," *Investigative radiology*, vol. 39, no. 9, pp. 537-545, 2004.
- [12] F. Calamante, "Arterial input function in perfusion MRI: a comprehensive review," *Progress in nuclear magnetic resonance spectroscopy*, vol. 74, pp. 1-32, 2013.
- [13] J. H. Maki, M. R. Prince, F. J. Londy, and T. L. Chenevert, "The effects of time varying intravascular signal intensity and k-space acquisition order on three-dimensional MR angiography image quality," *Journal of Magnetic Resonance Imaging*, vol. 6, no. 4, pp. 642-651, 1996.
- [14] Y. Zhang *et al.*, "Tumor Vascularity in Renal Masses: Correlation of Arterial Spin-Labeled and Dynamic Contrast-Enhanced Magnetic Resonance Imaging Assessments," *Clin Genitourin Cancer*, vol. 14, no. 1, pp. e25-36, Feb 2016.
- [15] L. Saleh, E. Juneman, and M. R. Movahed, "The use of gadolinium in patients with contrast allergy or renal failure requiring coronary angiography, coronary intervention, or vascular procedure," *Catheter Cardiovasc Interv*, vol. 78, no. 5, pp. 747-54, Nov 1 2011.
- [16] P. H. Kuo, E. Kanal, A. K. Abu-Alfa, and S. E. Cowper, "Gadolinium-based MR contrast agents and nephrogenic systemic fibrosis," *Radiology*, vol. 242, no. 3, pp. 647-649, 2007.
- [17] E. Kanal and M. F. Tweedle, "Residual or retained gadolinium: practical implications for radiologists and our patients," *Radiology*, vol. 275, no. 3, pp. 630-634, 2015.
- [18] D. R. Roberts *et al.*, "High levels of gadolinium deposition in the skin of a patient with normal renal function," *Investigative radiology*, vol. 51, no. 5, pp. 280-289, 2016.
- [19] T. Kanda *et al.*, "Gadolinium-based contrast agent accumulates in the brain even in subjects without severe renal dysfunction: evaluation of autopsy brain specimens with inductively coupled plasma mass spectroscopy," *Radiology*, vol. 276, no. 1, pp. 228-232, 2015.
- [20] S. Rajaram *et al.*, "3D contrast-enhanced lung perfusion MRI is an effective screening tool for chronic thromboembolic pulmonary hypertension: results from the ASPIRE Registry," *Thorax*, vol. 68, no. 7, pp. 677-678, 2013.
- [21] C. S. Johns *et al.*, "Lung perfusion: MRI vs. SPECT for screening in suspected chronic thromboembolic pulmonary hypertension," *Journal of Magnetic Resonance Imaging*, 2017.

- [22] K. Qing *et al.*, "Regional mapping of gas uptake by blood and tissue in the human lung using hyperpolarized xenon-129 MRI," *J Magn Reson Imaging*, vol. 39, no. 2, pp. 346-59, Feb 2014.
- [23] G. W. Miller *et al.*, "Advances in functional and structural imaging of the human lung using proton MRI," *NMR Biomed*, vol. 27, no. 12, pp. 1542-56, Dec 2014.
- [24] G. Bauman *et al.*, "Non-contrast-enhanced perfusion and ventilation assessment of the human lung by means of fourier decomposition in proton MRI," *Magn Reson Med*, vol. 62, no. 3, pp. 656-64, Sep 2009.
- [25] G. Bauman *et al.*, "Pulmonary functional imaging: qualitative comparison of Fourier decomposition MR imaging with SPECT/CT in porcine lung," *Radiology*, vol. 260, no. 2, pp. 551-9, Aug 2011.
- [26] G. Bauman *et al.*, "Lung ventilation-and perfusion-weighted Fourier decomposition magnetic resonance imaging: in vivo validation with hyperpolarized ^3He and dynamic contrast-enhanced MRI," *Magnetic resonance in medicine*, vol. 69, no. 1, pp. 229-237, 2013.
- [27] M. Lederlin *et al.*, "Functional MRI using Fourier decomposition of lung signal: reproducibility of ventilation-and perfusion-weighted imaging in healthy volunteers," *European journal of radiology*, vol. 82, no. 6, pp. 1015-1022, 2013.
- [28] Å. Kjørstad *et al.*, "Quantitative lung perfusion evaluation using Fourier decomposition perfusion MRI," *Magnetic resonance in medicine*, vol. 72, no. 2, pp. 558-562, 2014.
- [29] J. A. Detre, J. S. Leigh, D. S. Williams, and A. P. Koretsky, "Perfusion imaging," *Magnetic resonance in medicine*, vol. 23, no. 1, pp. 37-45, 1992.
- [30] D. S. Williams, J. A. Detre, J. S. Leigh, and A. P. Koretsky, "Magnetic resonance imaging of perfusion using spin inversion of arterial water," *Proceedings of the National Academy of Sciences*, vol. 89, no. 1, pp. 212-216, 1992.
- [31] R. B. Buxton *et al.*, "A general kinetic model for quantitative perfusion imaging with arterial spin labeling," *Magnetic resonance in medicine*, vol. 40, no. 3, pp. 383-396, 1998.
- [32] A. Pfefferbaum *et al.*, "Volumetric cerebral perfusion imaging in healthy adults: regional distribution, laterality, and repeatability of pulsed continuous arterial spin labeling (PCASL)," *Psychiatry Research: Neuroimaging*, vol. 182, no. 3, pp. 266-273, 2010.
- [33] N. A. Telischak, J. A. Detre, and G. Zaharchuk, "Arterial spin labeling MRI: clinical applications in the brain," *Journal of Magnetic Resonance Imaging*, vol. 41, no. 5, pp. 1165-1180, 2015.

- [34] P. M. Robson *et al.*, "Volumetric arterial spin-labeled perfusion imaging of the kidneys with a three-dimensional fast spin echo acquisition," *Academic radiology*, vol. 23, no. 2, pp. 144-154, 2016.
- [35] P. M. Robson *et al.*, "Strategies for reducing respiratory motion artifacts in renal perfusion imaging with arterial spin labeling," *Magn Reson Med*, vol. 61, no. 6, pp. 1374-87, Jun 2009.
- [36] W.-C. Wu, M.-Y. Su, C.-C. Chang, W.-Y. I. Tseng, and K.-L. Liu, "Renal perfusion 3-T MR imaging: a comparative study of arterial spin labeling and dynamic contrast-enhanced techniques," *Radiology*, vol. 261, no. 3, pp. 845-853, 2011.
- [37] D. W. Kim *et al.*, "Measurement of arterial transit time and renal blood flow using pseudocontinuous ASL MRI with multiple post-labeling delays: Feasibility, reproducibility, and variation," *Journal of Magnetic Resonance Imaging*, vol. 46, no. 3, pp. 813-819, 2017.
- [38] P. Martirosian, U. Klose, I. Mader, and F. Schick, "FAIR true-FISP perfusion imaging of the kidneys," *Magn Reson Med*, vol. 51, no. 2, pp. 353-61, Feb 2004.
- [39] C. de Bazelaire *et al.*, "Magnetic resonance imaging-measured blood flow change after antiangiogenic therapy with PTK787/ZK 222584 correlates with clinical outcome in metastatic renal cell carcinoma," *Clinical Cancer Research*, vol. 14, no. 17, pp. 5548-5554, 2008.
- [40] I. Pedrosa, D. C. Alsop, and N. M. Rofsky, "Magnetic resonance imaging as a biomarker in renal cell carcinoma," *Cancer*, vol. 115, no. S10, pp. 2334-2345, 2009.
- [41] V. M. Mai and S. S. Berr, "MR perfusion imaging of pulmonary parenchyma using pulsed arterial spin labeling techniques: FAIRER and FAIR," *Journal of Magnetic Resonance Imaging*, vol. 9, no. 3, pp. 483-487, 1999.
- [42] A. C. Henderson, G. K. Prisk, D. L. Levin, S. R. Hopkins, and R. B. Buxton, "Characterizing pulmonary blood flow distribution measured using arterial spin labeling," *NMR Biomed*, vol. 22, no. 10, pp. 1025-35, Dec 2009.
- [43] C. Schraml *et al.*, "Non-invasive pulmonary perfusion assessment in young patients with cystic fibrosis using an arterial spin labeling MR technique at 1.5 T," *MAGMA*, vol. 25, no. 2, pp. 155-62, Apr 2012.
- [44] X. Golay, J. Hendrikse, and T. C. Lim, "Perfusion imaging using arterial spin labeling," *Topics in Magnetic Resonance Imaging*, vol. 15, no. 1, pp. 10-27, 2004.

- [45] E. T. Petersen, I. Zimine, Y. C. Ho, and X. Golay, "Non-invasive measurement of perfusion: a critical review of arterial spin labelling techniques," *Br J Radiol*, vol. 79, no. 944, pp. 688-701, Aug 2006.
- [46] W. Dai, D. Garcia, C. de Bazelaire, and D. C. Alsop, "Continuous flow-driven inversion for arterial spin labeling using pulsed radio frequency and gradient fields," *Magn Reson Med*, vol. 60, no. 6, pp. 1488-97, Dec 2008.
- [47] A. Tannús and M. Garwood, "Adiabatic pulses," *NMR in Biomedicine: An International Journal Devoted to the Development and Application of Magnetic Resonance In Vivo*, vol. 10, no. 8, pp. 423-434, 1997.
- [48] D. C. Alsop and J. A. Detre, "Multisection cerebral blood flow MR imaging with continuous arterial spin labeling," *Radiology*, vol. 208, no. 2, pp. 410-416, 1998.
- [49] D. Roberts, J. A. Detre, L. Bolinger, E. K. Insko, and J. S. Leigh, "Quantitative magnetic resonance imaging of human brain perfusion at 1.5 T using steady-state inversion of arterial water," *Proceedings of the National Academy of Sciences*, vol. 91, no. 1, pp. 33-37, 1994.
- [50] D. A. Roberts *et al.*, "Pulmonary perfusion: respiratory-triggered three-dimensional MR imaging with arterial spin tagging—preliminary results in healthy volunteers," *Radiology*, vol. 212, no. 3, pp. 890-895, 1999.
- [51] J. A. Detre *et al.*, "Tissue specific perfusion imaging using arterial spin labeling," *NMR in Biomedicine*, vol. 7, no. 1-2, pp. 75-82, 1994.
- [52] E. C. Wong, R. B. Buxton, and L. R. Frank, "A theoretical and experimental comparison of continuous and pulsed arterial spin labeling techniques for quantitative perfusion imaging," *Magnetic Resonance in Medicine*, vol. 40, no. 3, pp. 348-355, 1998.
- [53] D. C. Alsop *et al.*, "Recommended implementation of arterial spin-labeled perfusion MRI for clinical applications: A consensus of the ISMRM perfusion study group and the European consortium for ASL in dementia," *Magnetic resonance in medicine*, vol. 73, no. 1, pp. 102-116, 2015.
- [54] D. M. Garcia, G. Duhamel, and D. C. Alsop, "Efficiency of inversion pulses for background suppressed arterial spin labeling," *Magn Reson Med*, vol. 54, no. 2, pp. 366-72, Aug 2005.
- [55] S. Aslan *et al.*, "Estimation of labeling efficiency in pseudocontinuous arterial spin labeling," *Magnetic resonance in medicine*, vol. 63, no. 3, pp. 765-771, 2010.

- [56] Z. Chen, X. Zhang, C. Yuan, X. Zhao, and M. J. van Osch, "Measuring the labeling efficiency of pseudocontinuous arterial spin labeling," *Magnetic resonance in medicine*, vol. 77, no. 5, pp. 1841-1852, 2017.
- [57] D. Heijtel *et al.*, "Accuracy and precision of pseudo-continuous arterial spin labeling perfusion during baseline and hypercapnia: a head-to-head comparison with ^{15}O H $_2\text{O}$ positron emission tomography," *Neuroimage*, vol. 92, pp. 182-192, 2014.
- [58] G. Xu *et al.*, "Reliability and precision of pseudo-continuous arterial spin labeling perfusion MRI on 3.0 T and comparison with ^{15}O -water PET in elderly subjects at risk for Alzheimer's disease," *NMR in Biomedicine*, vol. 23, no. 3, pp. 286-293, 2010.
- [59] Y. Chen, D. J. Wang, and J. A. Detre, "Test–retest reliability of arterial spin labeling with common labeling strategies," *Journal of Magnetic Resonance Imaging*, vol. 33, no. 4, pp. 940-949, 2011.
- [60] D. S. Bolar *et al.*, "Quantification of regional pulmonary blood flow using ASL-FAIRER," *Magn Reson Med*, vol. 55, no. 6, pp. 1308-17, Jun 2006.
- [61] S. R. Hopkins and G. K. Prisk, "Lung perfusion measured using magnetic resonance imaging: New tools for physiological insights into the pulmonary circulation," *J Magn Reson Imaging*, vol. 32, no. 6, pp. 1287-301, Dec 2010.
- [62] G. J. Stanisz *et al.*, "T1, T2 relaxation and magnetization transfer in tissue at 3T," *Magn Reson Med*, vol. 54, no. 3, pp. 507-12, Sep 2005.
- [63] M. N. Yongbi, F. Fera, Y. Yang, J. A. Frank, and J. H. Duyn, "Pulsed Arterial Spin Labeling: Comparison of Multisection Baseline and Functional MR Imaging Perfusion Signal at 1.5 and 3.0 T: Initial Results in Six Subjects 1," *Radiology*, vol. 222, no. 2, pp. 569-575, 2002.
- [64] E. Heiberg *et al.*, "FourFlow-open source code software for quantification and visualization of time-resolved three-directional phase contrast magnetic resonance velocity mapping," *Journal of Cardiovascular Magnetic Resonance*, vol. 14, no. S1, p. W14, 2012.
- [65] J. M. Gardin, C. S. Burn, W. J. Childs, and W. L. Henry, "Evaluation of blood flow velocity in the ascending aorta and main pulmonary artery of normal subjects by Doppler echocardiography," *American heart journal*, vol. 107, no. 2, pp. 310-319, 1984.
- [66] H. Lu, C. Clingman, X. Golay, and P. C. van Zijl, "Determining the longitudinal relaxation time (T1) of blood at 3.0 Tesla," *Magn Reson Med*, vol. 52, no. 3, pp. 679-82, Sep 2004.

- [67] W. Yang *et al.*, "Hepatic blood flow distribution and performance in conventional and novel Y-graft Fontan geometries: a case series computational fluid dynamics study," *The Journal of thoracic and cardiovascular surgery*, vol. 143, no. 5, pp. 1086-1097, 2012.
- [68] K. Suga, Y. Kawakami, H. Iwanaga, O. Tokuda, and N. Matsunaga, "Automated breath-hold perfusion SPECT/CT fusion images of the lungs," *American Journal of Roentgenology*, vol. 189, no. 2, pp. 455-463, 2007.
- [69] Joshua S. Greer *et al.*, "Non-contrast Pulmonary Perfusion at 3T using FAIR with inflow saturation and background suppression," in *International Society for Magnetic Resonance in Medicine*, Singapore, 2016, p. 1007.
- [70] Y.-R. Lin *et al.*, "Inflow-weighted pulmonary perfusion: comparison between dynamic contrast-enhanced MRI versus perfusion scintigraphy in complex pulmonary circulation," *Journal of Cardiovascular Magnetic Resonance*, vol. 15, no. 1, p. 21, 2013.
- [71] S. C. Walker, A. K. Asadi, S. R. Hopkins, R. B. Buxton, and G. K. Prisk, "A statistical clustering approach to discriminating perfusion from conduit vessel signal contributions in a pulmonary ASL MR image," *NMR Biomed*, vol. 28, no. 9, pp. 1117-24, Sep 2015.
- [72] R. J. Theilmann *et al.*, "Quantitative MRI measurement of lung density must account for the change in T_2^* with lung inflation," *Journal of Magnetic Resonance Imaging*, vol. 30, no. 3, pp. 527-534, 2009.
- [73] P. Martirosian *et al.*, "Quantitative lung perfusion mapping at 0.2 T using FAIR True-FISP MRI," *Magn Reson Med*, vol. 55, no. 5, pp. 1065-74, May 2006.
- [74] J. S. Greer *et al.*, "Non-contrast quantitative pulmonary perfusion using flow alternating inversion recovery at 3 T: A preliminary study," *Magnetic resonance imaging*, vol. 46, pp. 106-113, 2018.
- [75] S. Mani, J. Pauly, S. Conolly, C. Meyer, and D. Nishimura, "Background suppression with multiple inversion recovery nulling: applications to projective angiography," *Magnetic resonance in medicine*, vol. 37, no. 6, pp. 898-905, 1997.
- [76] F. Q. Ye, J. A. Frank, D. R. Weinberger, and A. C. McLaughlin, "Noise reduction in 3D perfusion imaging by attenuating the static signal in arterial spin tagging (ASSIST)," *Magnetic resonance in medicine*, vol. 44, no. 1, pp. 92-100, 2000.
- [77] K. S. Burrowes, R. B. Buxton, and G. K. Prisk, "Assessing potential errors of MRI-based measurements of pulmonary blood flow using a detailed network flow model," *Journal of Applied Physiology*, vol. 113, no. 1, pp. 130-141, 2012.

- [78] N. Maleki, W. Dai, and D. C. Alsop, "Optimization of background suppression for arterial spin labeling perfusion imaging," *MAGMA*, vol. 25, no. 2, pp. 127-33, Apr 2012.
- [79] X. Wang *et al.*, "Frequency Offset Corrected Inversion Pulse for B0 and B1 Insensitive Fat Suppression at 3T: An Exploratory Application to Brachial Plexus MR Neurography," *Journal of Magnetic Resonance Imaging (accepted)*.
- [80] E. C. Wong, R. B. Buxton, and L. R. Frank, "Quantitative imaging of perfusion using a single subtraction (QUIPSS and QUIPSS II)," *Magnetic resonance in medicine*, vol. 39, no. 5, pp. 702-708, 1998.
- [81] T. Bartalena *et al.*, "Lung perfusion in patients with pulmonary hypertension: comparison between MDCT pulmonary angiography with minIP reconstructions and 99mTc-MAA perfusion scan," *Investigative radiology*, vol. 43, no. 6, pp. 368-373, 2008.
- [82] Joshua S. Greer, Yue Zhang, Ivan Pedrosa, and A. J. Madhuranthakam, "Non-Contrast Pulmonary Perfusion using pseudo-Continuous Arterial Spin Labeling of the Inferior Vena Cava " in *International Society for Magnetic Resonance in Medicine*, Toronto, 2015, p. 534.
- [83] S. Kawanami *et al.*, "Flow-weighted MRI of the Lungs with the ECG-gated half-Fourier FSE technique: Evaluation of the Effect of the Cardiac Cycle," *Magnetic Resonance in Medical Sciences*, vol. 1, no. 3, pp. 137-147, 2002.
- [84] J. Knight-Scott, S. D. Keilholz-George, V. M. Mai, and J. M. Christopher, "Temporal dynamics of blood flow effects in half-Fourier fast spin echo 1H magnetic resonance imaging of the human lungs," *Journal of Magnetic Resonance Imaging: An Official Journal of the International Society for Magnetic Resonance in Medicine*, vol. 14, no. 4, pp. 411-418, 2001.
- [85] B. P. Poncelet *et al.*, "Measurement of human myocardial perfusion by double-gated flow alternating inversion recovery EPI," *Magnetic resonance in medicine*, vol. 41, no. 3, pp. 510-519, 1999.
- [86] L. Zhao, M. Vidorreta, S. Soman, J. A. Detre, and D. C. Alsop, "Improving the robustness of pseudo-continuous arterial spin labeling to off-resonance and pulsatile flow velocity," *Magn Reson Med*, vol. 78, no. 4, pp. 1342-1351, Oct 2017.
- [87] H. Jahanian, D. C. Noll, and L. Hernandez-Garcia, "B0 field inhomogeneity considerations in pseudo-continuous arterial spin labeling (pCASL): effects on tagging efficiency and correction strategy," *NMR Biomed*, vol. 24, no. 10, pp. 1202-9, Dec 2011.
- [88] P. Martirosian *et al.*, "Measurement of lung perfusion using optimized pseudo-continuous arterial spin labeling of pulmonary arteries and fast True-FISP imaging at 3 Tesla," in *25th*

Annual Meeting and Exhibition of the International Society for Magnetic Resonance in Medicine (ISMRM), 2017.

- [89] P. Martirosian *et al.*, "Measurement of Pulmonary Perfusion using PCASL True-FISP Imaging at 1.5 Tesla," in *26th Annual Meeting and Exhibition of the International Society for Magnetic Resonance in Medicine (ISMRM)*, 2018.
- [90] F. Seith *et al.*, "Temporal and spatial evaluation of pulmonary blood flow using multiple delay PCASL at 1.5 Tesla," in *26th Annual Meeting and Exhibition of the International Society for Magnetic Resonance in Medicine (ISMRM)*, 2018.
- [91] A. C. Lardo, S. A. Webber, I. Friehs, J. Pedro, and E. G. Cape, "Fluid dynamic comparison of intra-atrial and extracardiac total cavopulmonary connections," *The Journal of thoracic and cardiovascular surgery*, vol. 117, no. 4, pp. 697-704, 1999.
- [92] Y. Imoto, A. Sese, and K. Joh, "Redirection of the hepatic venous flow for the treatment of pulmonary arteriovenous malformations after Fontan operation," *Pediatric cardiology*, vol. 27, no. 4, pp. 490-492, 2006.
- [93] A. Cloutier *et al.*, "Abnormal distribution of pulmonary blood flow after the Glenn shunt or Fontan procedure: risk of development of arteriovenous fistulae," *Circulation*, vol. 72, no. 3, pp. 471-479, 1985.
- [94] D. Srivastava *et al.*, "Hepatic venous blood and the development of pulmonary arteriovenous malformations in congenital heart disease," *Circulation*, vol. 92, no. 5, pp. 1217-1222, 1995.
- [95] J.-w. Lee, J.-J. Park, H. W. Goo, and J. K. Ko, "Fontan Revision with Y-Graft in a Patient with Unilateral Pulmonary Arteriovenous Malformation," *The Korean journal of thoracic and cardiovascular surgery*, vol. 50, no. 3, p. 207, 2017.
- [96] S.-J. Kim *et al.*, "Inclusion of hepatic venous drainage in patients with pulmonary arteriovenous fistulas," *The Annals of thoracic surgery*, vol. 87, no. 2, pp. 548-553, 2009.
- [97] T. Matsushita *et al.*, "Assessment of the intrapulmonary ventilation-perfusion distribution after the Fontan procedure for complex cardiac anomalies: relation to pulmonary hemodynamics," *Journal of the American College of Cardiology*, vol. 15, no. 4, pp. 842-848, 1990.
- [98] T. B. Fredenburg, T. R. Johnson, and M. D. Cohen, "The Fontan procedure: anatomy, complications, and manifestations of failure," *Radiographics*, vol. 31, no. 2, pp. 453-463, 2011.

- [99] M. Markl *et al.*, "Time-resolved three-dimensional magnetic resonance velocity mapping of cardiovascular flow paths in volunteers and patients with Fontan circulation," *European Journal of Cardio-Thoracic Surgery*, vol. 39, no. 2, pp. 206-212, 2011.
- [100] P. Bächler *et al.*, "Caval blood flow distribution in patients with Fontan circulation: quantification by using particle traces from 4D flow MR imaging," *Radiology*, vol. 267, no. 1, pp. 67-75, 2013.
- [101] W. Commons. (July 18, 2018). *Diagram of the human heart*. Available: [https://commons.wikimedia.org/wiki/File:Diagram_of_the_human_heart_\(cropped\).svg](https://commons.wikimedia.org/wiki/File:Diagram_of_the_human_heart_(cropped).svg)
- [102] P. G. Walker, T. T. Howe, R. L. Davies, J. Fisher, and K. G. Watterson, "Distribution of hepatic venous blood in the total cavo-pulmonary connection: an in vitro study," *European journal of cardio-thoracic surgery*, vol. 17, no. 6, pp. 658-665, 2000.
- [103] M. Markl *et al.*, "Time-resolved three-dimensional magnetic resonance velocity mapping of cardiovascular flow paths in volunteers and patients with Fontan circulation☆," *European Journal of Cardio-Thoracic Surgery*, vol. 39, no. 2, pp. 206-212, 2011.
- [104] K. S. Roman *et al.*, "Comparative imaging of differential pulmonary blood flow in patients with congenital heart disease: magnetic resonance imaging versus lung perfusion scintigraphy," *Pediatric radiology*, vol. 35, no. 3, pp. 295-301, 2005.
- [105] A. Nilsson, K. M. Bloch, J. Töger, E. Heiberg, and F. Ståhlberg, "Accuracy of four-dimensional phase-contrast velocity mapping for blood flow visualizations: a phantom study," *Acta Radiologica*, vol. 54, no. 6, pp. 663-671, 2013.
- [106] M. A. Fogel *et al.*, "The nature of flow in the systemic venous pathway measured by magnetic resonance blood tagging in patients having the Fontan operation," *The Journal of thoracic and cardiovascular surgery*, vol. 114, no. 6, pp. 1032-1041, 1997.
- [107] M. A. Fogel *et al.*, "Caval contribution to flow in the branch pulmonary arteries of Fontan patients with a novel application of magnetic resonance presaturation pulse," *Circulation*, vol. 99, no. 9, pp. 1215-1221, 1999.
- [108] L. P. Dasi *et al.*, "Pulmonary hepatic flow distribution in total cavopulmonary connections: extracardiac versus intracardiac," *The Journal of thoracic and cardiovascular surgery*, vol. 141, no. 1, pp. 207-214, 2011.
- [109] C. Prieto *et al.*, "Highly efficient respiratory motion compensated free-breathing coronary MRA using golden-step Cartesian acquisition," *Journal of Magnetic Resonance Imaging*, vol. 41, no. 3, pp. 738-746, 2015.

- [110] M. Usman, B. Ruijsink, M. Nazir, G. Cruz, and C. Prieto, "Free breathing whole-heart 3D CINE MRI with self-gated Cartesian trajectory," *Magnetic resonance imaging*, vol. 38, pp. 129-137, 2017.
- [111] R. F. Busse, H. Hariharan, A. Vu, and J. H. Brittain, "Fast spin echo sequences with very long echo trains: design of variable refocusing flip angle schedules and generation of clinical T2 contrast," *Magn Reson Med*, vol. 55, no. 5, pp. 1030-7, May 2006.
- [112] D. C. Noll, D. G. Nishimura, and A. Macovski, "Homodyne detection in magnetic resonance imaging," *IEEE transactions on medical imaging*, vol. 10, no. 2, pp. 154-163, 1991.
- [113] R. J. Ordidge, M. Wylezinska, J. W. Hugg, E. Butterworth, and F. Franconi, "Frequency offset corrected inversion (FOCI) pulses for use in localized spectroscopy," *Magnetic resonance in medicine*, vol. 36, no. 4, pp. 562-566, 1996.
- [114] H. She *et al.*, "Accelerating Chemical Exchange Saturation Transfer MRI with Parallel Blind Compressed Sensing," *Magnetic Resonance in Medicine (accepted)*.
- [115] H. She, J. S. Greer, X. Wang, A. Madhuranthakam, and E. Vinogradov, "Accelerated 3D Arterial Spin Labeling using Cartesian Acquisition with Spiral Reordering and Compressed Sensing," in *International Society for Magnetic Resonance in Medicine*, Honolulu, 2017.
- [116] A. J. Madhuranthakam, Q. Yuan, and I. Pedrosa, "Quantitative Methods in Abdominal MRI: Perfusion Imaging," *Topics in Magnetic Resonance Imaging*, vol. 26, no. 6, pp. 251-258, 2017.
- [117] X. Qiao *et al.*, "Arterial spin-labeling perfusion MRI stratifies progression-free survival and correlates with epidermal growth factor receptor status in glioblastoma," *American Journal of Neuroradiology*, vol. 36, no. 4, pp. 672-677, 2015.
- [118] G. Y. Cho *et al.*, "A versatile flow phantom for intravoxel incoherent motion MRI," *Magnetic resonance in medicine*, vol. 67, no. 6, pp. 1710-1720, 2012.
- [119] K. Hulsey, M. Lewis, Y. Xi, Q. Yuan, and R. E. Lenkinski, "Comparison of Results Obtained by Fitting DWI Data to a Model Including IVIM and Kurtosis Using Nonlinear Least Squares and Maximum Likelihood Estimation," in *International Society for Magnetic Resonance in Medicine, 23rd Scientific Meeting*, Toronto, 2015, p. 2911.

BIOGRAPHICAL SKETCH

Joshua S. Greer was born in Dallas, TX in 1991. After graduating from Rowlett High School in 2009, he attended Texas A&M in College Station, TX. In May of 2013, he received his Bachelor of Science in Biomedical Engineering, and was accepted into the joint Bioengineering graduate program between UT Dallas and UT Southwestern Medical Center. He joined Dr. Ananth J. Madhuranthakam's laboratory to develop lung perfusion imaging using arterial spin labeled MRI. In the fall of 2018, he received his Doctor of Philosophy in Biomedical Engineering.

CURRICULUM VITAE

Joshua S. Greer

joshua.greer@utsouthwestern.edu

EDUCATION

University of Texas at Dallas 2013 – 2018
Ph.D. Bioengineering
Advisor: Dr. Ananth Madhuranthakam, *UT Southwestern Medical Center*

Texas A&M University 2009 – 2013
B.S. Biomedical Engineering
Focus: Bioinstrumentation
Minor: Electrical Engineering

TEACHING EXPERIENCE

University of Texas at Dallas Spring 2014
Teaching Assistant
Introduction to Bioengineering

University of Texas at Dallas Fall 2013
Teaching Assistant
Static Equilibrium and Rigid Body Dynamics

Texas A&M University 2011 – 2013
Tutor
Independently tutored students in Calculus, Chemistry, and Solid Mechanics

RESEARCH EXPERIENCE

UT Southwestern Medical Center 2013 – 2018
Doctoral Researcher – Dr. Ananth J. Madhuranthakam
MRI Translational Research lab
Development of 3D non-contrast pulmonary perfusion MRI using arterial spin labeling

Texas A&M University 2012 – 2013
Undergraduate Research Assistant – Dr. Vladislav Yakovlev
Application of Raman Spectroscopy using a broadband light source.

AWARDS

Society for Cardiovascular Magnetic Resonance Travel Award	2017
ISMRM Trainee Travel Award, 25 th annual meeting in Honolulu	2017
2nd place, Best ASL Poster, Perfusion Study Group, ISMRM 24 th annual meeting in Singapore <i>Pulmonary Perfusion using pseudo-Continuous Arterial Spin Labeling.</i>	2016
ISMRM Magna Cum Laude Merit Award, 24 th annual meeting in Singapore <i>B0 and B1 Insensitive Robust Fat Suppression using Frequency Offset Corrected Inversion (FOCI).</i>	2016
ISMRM Magna Cum Laude Merit Award, 24 th annual meeting in Singapore <i>Pulmonary Perfusion using pseudo-Continuous Arterial Spin Labeling.</i>	2016
ISMRM Magna Cum Laude Merit Award, 24 th annual meeting in Singapore <i>Non-Contrast Pulmonary at 3T using FAIR with inflow saturation and background suppression</i>	2016
ISMRM Trainee Travel Award, 24 th annual meeting in Singapore	2016
ISMRM Magna Cum Laude Merit Award, 23 rd annual meeting in Toronto <i>Non-Contrast Pulmonary Perfusion using pseudo-Continuous Arterial Spin Labeling of the Inferior Vena Cava</i>	2015
ISMRM Trainee Travel Award, 23 rd annual meeting in Toronto	2015
College of Engineering Student Scholar, Texas A&M University	2013

PUBLICATIONS

Huajun She, Bian Li, **Joshua S. Greer**, Jochen Keupp, Ananth J. Madhuranthakam, Ivan E. Dimitrov, Robert E. Lenkinski, and Elena Vinogradov. Accelerating Chemical Exchange Saturation Transfer MRI with Parallel Blind Compressed Sensing. *Magnetic Resonance in Medicine* (accepted)

Xinzeng Wang, **Joshua S. Greer**, Ivan E. Dimitrov, Avneesh Chhabra, Ananth J. Madhuranthakam (2018) Frequency Offset Corrected Inversion Pulse for B0 and B1 Insensitive Fat Suppression at 3T: An Exploratory Application to Brachial Plexus MR Neurography. *Journal of Magnetic Resonance Imaging* (accepted)

Joshua S. Greer, Christopher D. Maroules, Orhan K. Oz, Suhny Abbara, Ronald M. Peshock, Ivan Pedrosa, Ananth J. Madhuranthakam (2017) Non-contrast quantitative pulmonary perfusion using flow alternating inversion recovery at 3T: A preliminary study. *Magnetic Resonance Imaging*, 46, 106-113,

Greer, J. S., Petrov, G. I. and Yakovlev, V. V. (2013), Raman spectroscopy with LED excitation source. *J. Raman Spectroscopy*, 44: 1058–1059

CONFERENCE PROCEEDINGS

Joshua S. Greer, Jerry Michael, Barbara Burkhardt, Animesh Tandon, Gerald F. Greil, Tarique Hussain, and Ananth J. Madhuranthakam, Caval Blood Flow Distribution in Fontan Circulation: Comparison between ASL-Measured Pulmonary Perfusion and 4D Flow. *In: Proceedings 26th Scientific Meeting, International Society for Magnetic Resonance in Medicine, Paris, France (2018) (Power pitch)*

Joshua S. Greer, Xinzeng Wang, and Ananth J. Madhuranthakam, Robust non-contrast perfusion imaging of whole-lungs using multi-slice FAIR at 3T. *In: Proceedings 26th Scientific Meeting, International Society for Magnetic Resonance in Medicine, Paris, France (2018) (poster)*

Shu Zhang, Bian Li, **Joshua Greer**, Xinzeng Wang, Ananth Madhuranthakam, Jochen Keupp, Ivan Dimitrov, Robert Lenkinski, Ivan Pedrosa, Elena Vinogradov, Toward CEST MRI of renal masses: protocol optimization and first preliminary data. *In: Proceedings 26th Scientific Meeting, International Society for Magnetic Resonance in Medicine, Paris, France (2018) (ePoster)*

Joshua S. Greer, Jerry Michael, Barbara Burkhardt, Animesh Tandon, Gerald F. Greil, Tarique Hussain, and Ananth J. Madhuranthakam. Assessment of caval blood flow distribution in Fontan circulation using arterial spin labeled measurement of pulmonary perfusion. *Radiology Research Day, UT Southwestern Medical Center, Dallas, TX (2018) (oral)*

Joshua S. Greer, Jerry Michael, Barbara Burkhardt, Animesh Tandon, Gerald F. Greil, Tarique Hussain, and Ananth J. Madhuranthakam. Assessment of caval blood flow distribution in Fontan circulation using arterial spin labeled measurement of pulmonary perfusion. *Society for Cardiovascular Magnetic Resonance, Barcelona, Spain (2018) (oral)*

Marco C. Pinho, **Joshua S. Greer**, Xinzeng Wang, Joseph Maldjian, Ananth J. Madhuranthakam. Robust Volumetric Non Contrast Perfusion Imaging of the Whole Brain using a 3D TSE Acquisition (CASPR). *In: Proceedings 55th Scientific Meeting, American Society of Neuroradiology, Long Beach, California (2017) (oral)*

Joshua S. Greer, Xinzeng Wang, Marco C. Pinho, Elena Vinogradov, Ivan Pedrosa, and Ananth J. Madhuranthakam. Robust 3D pCASL perfusion imaging using a Cartesian Acquisition with Spiral Reordering (CASPR). *In: Proceedings 25th Scientific Meeting, International Society for Magnetic Resonance in Medicine, Honolulu, HI (2017) (ePoster)*

Joshua S. Greer, Xinzeng Wang, Keith Hulsey, Robert E. Lenkinski, Ananth J. Madhuranthakam. A 3D printed perfusion phantom for quality controlled measurement of arterial spin labeled perfusion. In: *Proceedings 25th Scientific Meeting, International Society for Magnetic Resonance in Medicine, Honolulu, HI (2017) (ePoster)*

Huajun She, Bian Li, **Joshua S. Greer**, Jochen Keupp, Ananth Madhuranthakam, Ivan E. Dimitrov, Robert Lenkinski, and Elena Vinogradov. Accelerating CEST Imaging with Parallel Blind Compressed Sensing. In: *Proceedings 25th Scientific Meeting, International Society for Magnetic Resonance in Medicine, Honolulu, HI (2017) (oral)*

Huajun She, **Joshua S. Greer**, Xinzeng Wang, Elena Vinogradov, and Ananth J Madhuranthakam. Accelerated 3D Arterial Spin Labeling using Cartesian Acquisition with Spiral Reordering and Compressed Sensing. In: *Proceedings 25th Scientific Meeting, International Society for Magnetic Resonance in Medicine, Honolulu, HI (2017) (poster)*

Huajun She, Bian Li, **Joshua S. Greer**, Jochen Keupp, Ananth Madhuranthakam, Ivan E. Dimitrov, Robert Lenkinski, and Elena Vinogradov. Accelerating CEST Imaging with Experimental Undersampling and Compressed Sensing. In: *Proceedings 25th Scientific Meeting, International Society for Magnetic Resonance in Medicine, Honolulu, HI (2017) (ePoster)*

Xinzeng Wang, **Joshua S. Greer**, Marco C. Pinho, Robert R. Lenkinski, and Ananth J. Madhuranthakam. Volumetric T2-weighted and FLAIR Imaging of Spine with Uniform Fat Suppression in a Single Acquisition. In: *Proceedings 25th Scientific Meeting, International Society for Magnetic Resonance in Medicine, Honolulu, HI (2017)*

Atzimba Casas, **Joshua Greer**, and Ananth J. Madhuranthakam. Correlation between Arterial Spin Labeled and Dynamics Contrast Enhanced Perfusion Measurements in Renal Parenchyma and Renal Tumors. *BUILDing Scholars poster session, UT Southwestern Medical Center, Dallas, TX (2016) (poster)*

Joshua S. Greer, Keith Hulsey, Robert E. Lenkinski, and Ananth J. Madhuranthakam. A simple and reliable perfusion phantom to measure precise and repeatable arterial spin labeled quantitative perfusion. In: *Proceedings 24th Scientific Meeting, International Society for Magnetic Resonance in Medicine, Singapore (2016) (poster)*

Joshua S. Greer, Xinzeng Wang, Ivan Pedrosa, and Ananth J. Madhuranthakam. Pulmonary Perfusion using pseudo-Continuous Arterial Spin Labeling. In: *Proceedings 24th Scientific Meeting, International Society for Magnetic Resonance in Medicine, Singapore (2016) (ePoster)*

Joshua S. Greer, Yue Zhang, Christopher Maroules, Orhan K. Oz, Ivan Pedrosa, and Ananth J. Madhuranthakam. Non-Contrast Pulmonary at 3T using FAIR with inflow saturation and background suppression. In: *Proceedings 24th Scientific Meeting, International Society for Magnetic Resonance in Medicine, Singapore (2016) (oral)*

Xinzeng Wang, **Joshua S. Greer**, Ivan Pedrosa, Neil M. Rofsky, and Ananth J. Madhuranthakam. Robust abdominal imaging with uniform fat suppression using Dixon based single shot turbo spin echo. *In: Proceedings 24th Scientific Meeting, International Society for Magnetic Resonance in Medicine, Singapore (2016) (oral)*

Xinzeng Wang, **Joshua S. Greer**, Ivan E. Dimitrov, Ananth J. Madhuranthakam. B0 and B1 Insensitive Robust Fat Suppression using Frequency Offset Corrected Inversion (FOCI). *In: Proceedings 24th Scientific Meeting, International Society for Magnetic Resonance in Medicine, Singapore (2016) (oral)*

Joshua S. Greer, Yue Zhang, Christopher Maroules, Orhan K. Oz, Ron Peshock, Ivan Pedrosa, and Ananth J. Madhuranthakam. Non-contrast Pulmonary Perfusion at 3T using FAIR with Inflow Saturation and Background Suppression. *Radiology Research Day, UT Southwestern Medical Center, Dallas, TX (2016) (poster)*

Joshua S. Greer, Yue Zhang, Christopher Maroules, Orhan K. Oz, Ivan Pedrosa, and Ananth J. Madhuranthakam. Pulmonary Perfusion using pseudo-Continuous Arterial Spin Labeling. *Radiology Research Day, UT Southwestern Medical Center, Dallas, TX (2016) (Poster)*

Joshua S. Greer, Xinzeng Wang, Ivan Pedrosa, and Ananth J. Madhuranthakam. Volumetric Non-Contrast Pulmonary Perfusion using pseudo-Continuous Arterial Spin Labeling. *In: Proceedings 23rd Scientific Meeting, International Society for Magnetic Resonance in Medicine, Toronto, Canada (2015) (poster)*

Joshua S. Greer, Yue Zhang, Ivan Pedrosa, and Ananth J. Madhuranthakam. Non-Contrast Pulmonary Perfusion using pseudo-Continuous Arterial Spin Labeling of the Inferior Vena Cava. *In: Proceedings 23rd Scientific Meeting, International Society for Magnetic Resonance in Medicine, Toronto, Canada (2015) (oral)*

Xinzeng Wang, **Joshua S. Greer**, Shu Zhang, and Ananth J. Madhuranthakam. Velocity Selective Prepared Non-Contrast Enhanced MR Angiography using Phase Sensitive Recontruction. *In: Proceedings 23rd Scientific Meeting, International Society for Magnetic Resonance in Medicine, Toronto, Canada (2015) (poster)*

Joshua S. Greer, Yue Zhang, Christopher Maroules, Ivan Pedrosa, and Ananth J. Madhuranthakam. Non-Contrast Pulmonary Perfusion MRI using Arterial Spin Labeling at 3T. *Radiology Research Day, UT Southwestern Medical Center, Dallas, TX (2015) (poster)*

INVITED TALKS

Quality Assurance in Clinical Trials Using Phantoms. International Society for Magnetic Resonance in Medicine, Member Initiated Symposium: How to Make Perfusion Imaging Become a Quantitative Imaging Biomarker, *Paris, France (2018)*

PATENTS

Madhuranthakam AJ, Wang X, Greer J, Pedrosa I. System and Method for Robust MR Imaging with Prepared Contrast using a Cartesian Acquisition with SPiral Reordering (CASPR) (US Provisional patent)

PROFESSIONAL ASSOCIATIONS

Society for Cardiovascular Magnetic Resonance (SCMR)	2017 – present
International Society for Magnetic Resonance in Medicine (ISMRM)	2014 – present
Radiological Society of North America (RSNA)	2013 – present